Experimental Characterization of Diffusive Phenomena in Multi-Ion-Species Plasma Shocks Formed During Railgun-Driven Plasma Jet Collision Events

Ameer I. Mohammed

Dissertation submitted to the Faculty of the

Virginia Polytechnic Institute and State University

in partial fulfillment of the requirements for the degree of

Doctor of Philosophy

in

Aerospace Engineering

Colin S. Adams, Chair

Bhuvana Srinivasan

Scott L. England

Wayne A. Scales

November 21st, 2023

Blacksburg, Virginia

Keywords: Multi-ion-species plasma, Plasma shocks, Diffusion, Transport processes

Experimental Characterization of Diffusive Phenomena in Multi-Ion-Species Plasma Shocks Formed During Railgun-Driven Plasma Jet Collision Events

Ameer I. Mohammed

(ABSTRACT)

Gradient-driven mass diffusion, or species separation, is a transport process which can occur in plasma shocks. Experimental observations of this phenomena are difficult to make, but are of interest to ongoing Inertial Confinement Fusion efforts. This body of work describes the results of two major experimental campaigns conducted at Virginia Tech's Experimental Plasma and Propulsion Laboratory to identify species separation in multi-component plasma shocks. A linear plasma-armature railgun forms and accelerates low temperature, high density, supersonic plasma jets, with the collision between two of these jets shown to induce a collisional plasma shock in the first campaign. The second campaign leverages this experimental setup while employing spatially resolved emission spectroscopy alongside collisional radiative modeling to identify species separation within multi-ion-species plasma shocks consisting of argon, aluminum, and nitrogen. These results are some of the first to be performed in a plasma shock with more than two ion species, and can be used for verification and validation of physics models of fusion plasmas.

This body of work was supported by the National Science Foundation under Grant No. PHY-1903442.

Experimental Characterization of Diffusive Phenomena in Multi-Ion-Species Plasma Shocks Formed During Railgun-Driven Plasma Jet Collision Events

Ameer I. Mohammed

(GENERAL AUDIENCE ABSTRACT)

Plasmas represent the fourth state of matter, where enough energy has been imparted onto a gas for ionization to occur, resulting in a quasi-neutral collection of charged and neutral particles that are subject to both hydrodynamic and electrodynamic effects. Shocks can occur in plasmas, which presents as a transition layer where plasma parameters drastically change over a small region of space. Plasmas hold the key to nuclear fusion, with the topic of gradient-driven mass diffusion, or species separation, in plasma shocks being of great interest to large-scale fusion experiments. This body of work performs experimental measurements using a railgun-based plasma source to create plasma shocks with multiple ion species in the laboratory, and ultimately observe this effect of species separation through the use of spatially resolved spectroscopy. To the author's best knowledge, these measurements represent some of the first to be done in a plasma shock with more than two ion species, and can be used to benchmark physics models of plasmas in fusion experiments.

Dedication

Dedicated to the memories of my aunt, Shamina Mohammed, and grandparents, Zobeida and Shamshudeen Mohammed.

Acknowledgments

This body of work is the culmination of five and half years of research. As I reflect on my experiences in graduate school throughout this time, I must acknowledge those whose support was essential to get me to this point.

First, I would like to thank Dr. Colin Adams for being my advisor. When I first stumbled into the Experimental Plasmas and Propulsion Laboratory (EPPL) in 2018, I had minimal experience with experimental plasma physics research. However, Dr. Adams trusted me with this project and gave me the resources and support to help me succeed as an experimentalist. There are many results within this dissertation that are a product of feedback from Dr. Adams on how to proceed in the lab. Beyond the laboratory, Dr. Adams' advice on preparing scientific manuscripts and presentations has been invaluable. I am the scientist I am today because of my time working with Dr. Adams, and I will remember all of the lessons I have learned as part of his research group as I move forward in my career.

My committee members have also provided a great deal of support and insight throughout my graduate school career. Thank you to Dr. Bhuvana Srinivasan for letting me sit in on your research group meetings during my first semester, and for making Computational Plasma Dynamics one of my favorite courses at Virginia Tech. Thank you to Dr. Wayne Scales for your helpful and insightful comments and questions during our committee meetings. Lastly, thank you to Dr. Scott England for always taking the time to chat with me whenever we would run into each other around campus, and for pointing me towards Dr. Adams' research group when I was applying to graduate school in 2018.

My experience at Virginia Tech was made all the better by the friends that I made during these last few years. Within our research group, Dan Weber and I have known each other the longest. During that time, Dan was always available to talk through problems as they came up in the lab and to help out with testing whenever I needed. I have fond memories of our meet-ups at PK's for Tijuana Toss, and of our often "thorough" testing of capacitor banks together. Trenton Brewer's assistance with testing was invaluable for the final campaign documented in this work. As lab and office-mates, I enjoyed our conversation topics that often ranged from abstract scientific discussions to raccoons(!). Minzhen Du is one of the most resourceful people I have ever met, and his engineering expertise helped to streamline many aspects of this project that would have otherwise been very difficult to execute. To my Space@VT colleagues : Aakash, Aishwarya, Deven, Jamil, Kolter, Matt, Sowmya and Vincent, thank you for your friendship all these years. Whether it was testing circuits, debugging code, or simply catching up over food, our interactions were always insightful and entertaining.

I am also very lucky to have a support system in the form of family and friends outside of the Blacksburg area. I have known Ben Ginty, Collin Morley and Julian LaRocca since high school, and over the entirety of my academic career, our mutual interests in music, concerts and food have provided welcome distractions from my studies when needed. To my extended family in Canada and Trinidad, the times that we get to see each other remain some of my favorite parts of each year. But I am most thankful to my parents, Charmian and Insaf, and sister, Sameerah for their love and support throughout this endeavor. Growing up, my parents both worked tirelessly to ensure that I could devote all my focus towards my studies. In undergraduate and graduate school, both my parents and sister have always been there to support me through good and bad times. I could not have finished this dissertation without them, and I feel very lucky to have them in my life.

Contents

List of Figures

List of Tables

Chapter 1

Introduction

Within the field of physics, the highest impact research occurs when results can be validated using theory, simulations and experiments. Within the sub-field of plasma physics, there are a variety of topics where such congruence has not yet been obtained, and therefore can serve as fertile ground for new experiments and scientific investigations.

One such topic is the physics of multi-ion-species plasma shocks, and the effect of gradient-driven diffusive mass flux on the shock structure [4, 23, 30, 31, 32]. This topic has experienced a period of renewed interest, due to its potential relevance to inertial confinement fusion experiments being conducted at US National Laboratories [7]. However, until recently, this attention has largely been contained to theoretical and computational-driven research efforts [3, 4, 7, 30, 31]. The lack of progress on this topic from an experimental standpoint can in part be explained due to the difficulty in obtaining the necessary measurements; ICF relevant shocks exist over spatial and temporal scales that are extremely difficult to survey [7]. Here at Virginia Tech's Experimental Plasma and Propulsion Laboratory (EPPL), we have designed a pulsed power experiment that is capable of generating centimeter scale plasma shocks that can be spatially and temporally diagnosed [8, 15, 17]. The work detailed in this dissertation discusses the role of species separation in multi-ion-species plasma shocks, a topic that until recently has only been investigated through a computational and theoretical framework [3, 4, 7, 30, 31]. This chapter will summarize the results of these previous investigations, while laying the foundation for our experimental efforts at the EPPL.

1.1 Hydrodynamic shocks in neutral gases

A shock is a transition layer in a fluid, across which fluid properties change dramatically [1, 2, 13]. Shocks occur in supersonic flows, and are the mechanism by which such flows adjust to abruptly changing conditions along their flow path [1, 2, 13]. A classic example of a hydrodynamic shock is supersonic flow past a two-dimensional wedge [1, 2, 13]. When one-dimensional supersonic flow encounters a two-dimensional wedge, a shock forms near the leading edge of the wedge as shown in Figure 1.1 [1, 2, 13]. The shock structure is dependent on the wedge angle, with small and large wedge angles inducing oblique and normal shocks respectively [1, 2, 13].

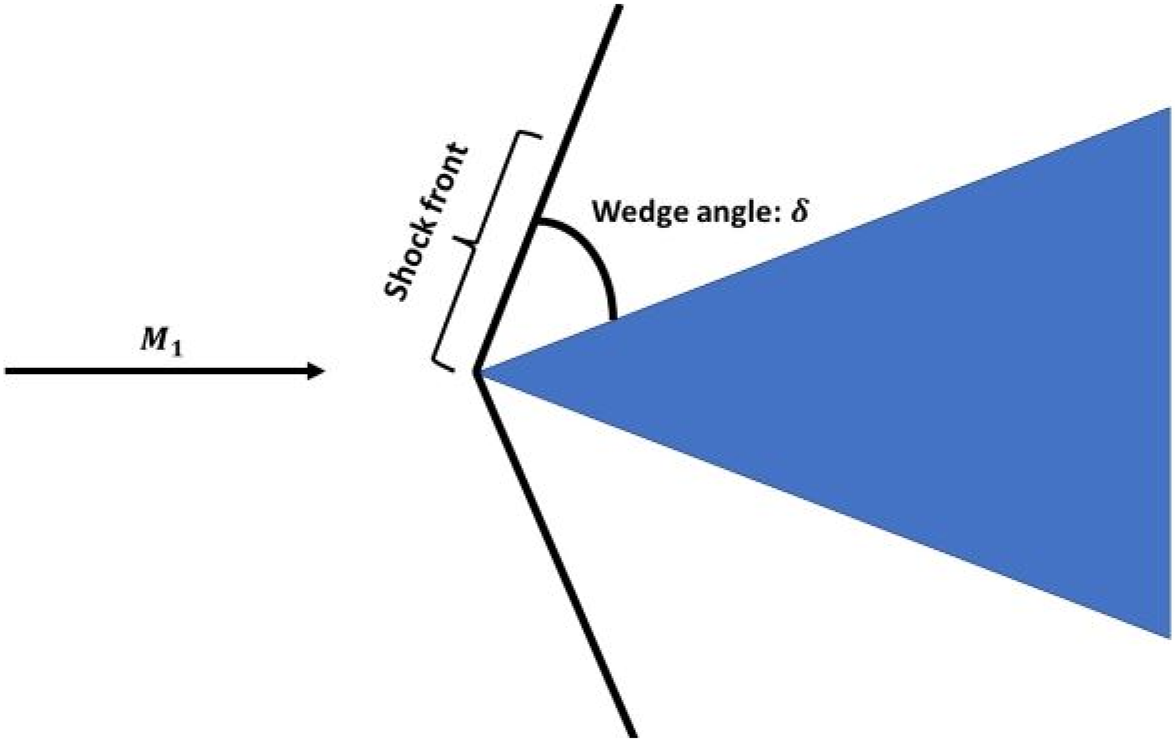

Figure 1.1: Shock formation due to supersonic flow past a two dimensional wedge. Image based on model from Ref. [1]. At larger wedge angles, δ, the shock morphology transitions from attached and oblique (as shown above) to detached and normal [1, 2].

Across a shock, the fluid density increases while the velocity component normal to the shock decreases [1, 2, 13]. The flow's kinetic energy may also be converted into thermal energy, heating the fluid and increasing its temperature [1, 2, 13, 24]. These changes can be characterized relative to the flow conditions upstream of the shock by the Rankine-Hugoniot jump conditions [2].

1.2 Collisional shocks in plasmas

Shock waves can also occur in plasmas. A plasma is an ionized gas that maintains quasi-neutrality and exhibits collective behavior [33]. The presence of ions and free electrons within a plasma necessitate the coupling of hydrodynamic and electrodynamic theory to understand plasma behavior [33]. This interplay presents the opportunity for complex physics processes to occur in plasmas and in plasma shocks.

A majority of physical phenomena is understood by modeling the plasma ion and electron species as a set of interpenetrating fluids [3, 4, 33]. This two-fluid model resolves macroscopic plasma quantities by evolving a self consistent set of hydrodynamic equations that have been modified with electrodynamic effects [3, 4, 33]. This approach is valid when the plasma is highly collisional with a near-Maxwellian particle distribution function [3, 4, 33]. When the distribution function is non-Maxwellian, a kinetic approach becomes necessary to resolve important physics [3, 4, 33]. Kinetic theory considers the distribution function of each species, and resolves microscopic plasma parameters using the Vlasov equation, which describes the time evolution of the particle distribution function [33]. While kinetic models provide a more complete physics picture, fluid codes are computationally cheaper and often easier to implement [33].

From a microscopic perspective, elastic collisions between charged particles in a plasma are mediated through their respective electric fields and are referred to as Coulomb collisions [33].

Due to the various types of Coulomb collisions that can occur (electron-electron, electron-ion, and ion-ion), numerous collisional mean free paths are defined for these processes [1, 3, 13, 19]. When these characteristic collision lengths are less than the scale length of the system, the plasma is considered collisional [1, 3, 13, 19]. Shocks mediated through binary collisions in neutral gases and plasmas are termed collisional shocks [24]. While the structure of a collisional plasma shock is still an area of active research, pioneering work by Jaffrin and Probstein [3] established the structure of hydro plasma shock utilizing a fluid model, as illustrated in Figure 1.2 [3, 4]. Scale lengths of the various regions across the shock are inferred using collisional mean free paths, with the electron-ion and ion-ion mean free paths establishing the length of the electron-preheating and ion compression layers present in the shock structure [1, 3, 13, 19].

Plasma shocks can also be collisionless, occurring by way of collective effects over spatial scales significantly less than the system mean free path [24, 34, 35]. While this dissertation focuses on collisional shocks, the broader plasma physics community is actively engaged in the study of collisionless shocks due to their relevance to particle acceleration and cosmic rays [24, 34, 35].

1.3 Inertial Cofinement Fusion and species separation in fusion fuel

While collisional plasma shocks may be considered less exotic than collisionless shocks, there has been a renaissance of plasma shock experiments [4, 13, 23, 24], due to their relevance in inertial confinement fusion (ICF) research. Nuclear fusion is the process where two light atoms bond together to form a heavier atom [6, 36]. When the mass of the heavier atom is less

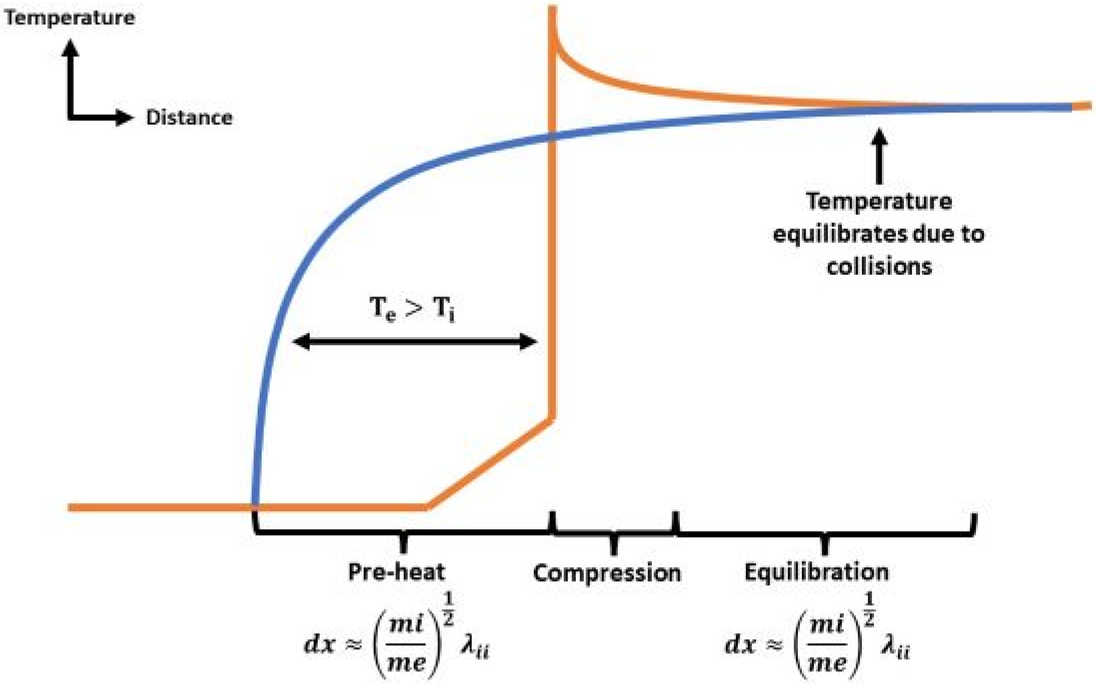

Figure 1.2: Structure of a collisional hydrodynamic plasma shock, as predicted by Jaffrin and Probstein's work in Ref. [3]. Drawing based on model from Ref. [4]. This two-fluid approach models a plasma consisting of interpenetrating ion and electron fluids. For an intermediate or strong plasma shock, the electron temperature initially rises ahead of the ion temperature in the "pre-heat region" [3, 4, 5]. This electron-ion temperature disparity is due to low electron inertia, which allows them to travel ahead of the compression layer [3, 4, 5]. Behind the pre-heating layer lies the ion compression layer, where ion temperature rises and exceeds the electron temperature, and equilibration layer, where electron-ion collisions relaxes the ion temperature to the electron temperature [3, 4, 5].

than the sum of its constituents, that difference in mass is given off as energy, determined by $E = mc^2$ [6]. The sun generates its energy through fusion reactions and serves as a reminder of the potential for nuclear fusion on Earth [6, 36]. A commercially viable approach to controlled nuclear fusion will provide a clean renewable energy source that can also be used to achieve long duration human spaceflight [37]. In experiment, the most commonly used fusion fuel consists of deuterium and tritium [36]. Inertial confinement fusion is one of many experimental setups designed to obtain net energy gain through nuclear fusion [6].

ICF aims to achieve nuclear fusion on extremely short timescales through the use of high intensity laser pulses, which imparts energy onto the surface of a capsule of deuterium-tritium fuel as shown in Figure 1.3 [6]. This imparted energy rapidly ablates the capsule surface, resulting in rocket-like blowoff of the ablator material which launches shock waves through the now deuterium-tritium plasma [6]. These shocks drive thermonuclear burn, resulting in fusion yield. [6, 7]

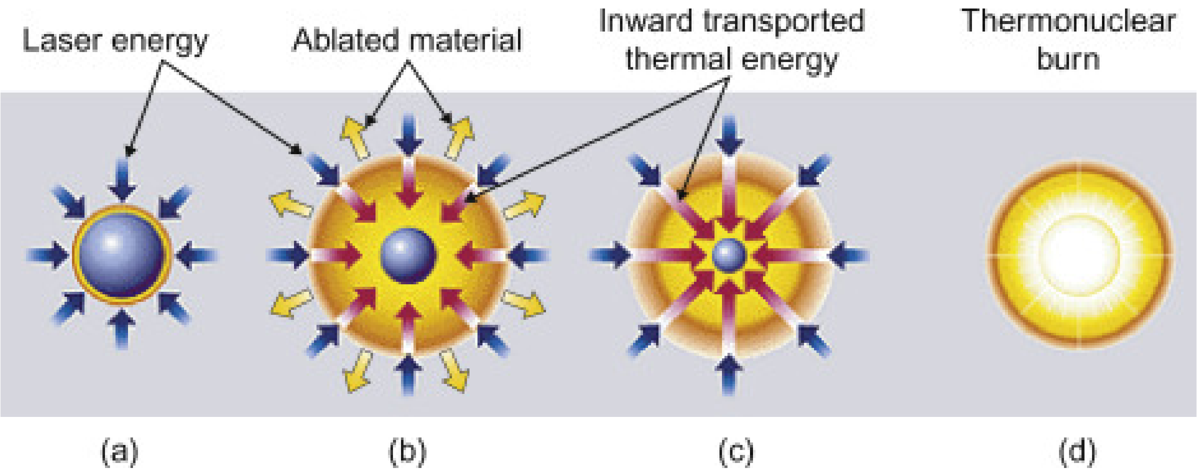

Figure 1.3: Stages of an inertial confinement fusion experiment. First, energy is imparted onto the surface of a pellet of fusion fuel (a) [6]. This heating of the fuel surface forms a plasma envelope (orange layer) [6]. The rocket-like blowoff of ablated material drives spherical shock waves that propagate inwards towards the center of the fusion fuel (b) [6]. These spherically converging shock waves increase the density and temperature of the fuel (c) [6], eventually igniting thermonuclear burn (d) [6]. Image used with permission of Elsevier Science and Technology Journals, from Ref. [6]: Garry McCracken and Peter Stott. Fusion: the energy of the universe. Academic Press, 2013.; permission conveyed through Copyright Clearance Center, Inc.

While results from ICF experiments in recent years have been encouraging, the experimental fusion yield has consistently fallen short of theoretical and computational predictions [7, 31, 38, 39, 40, 41]. . Recent theoretical work has suggested that this may due to shock-induced species separation of the deuterium and tritium plasma, which perturbs the initial mass concentration of the DT fusion fuel [7, 31, 38, 39, 40, 41].

1.4 Transport processes in plasma shocks

When considering a binary fluid mixture, it has long been theorized that gradients within the fluid parameters will drive separation between the fluid components [23, 30, 31, 32, 39, 42]. This theory, formulated for a neutral fluid by Landau and Lifshitz [42] has been adapted for adapted for a plasma, where electric fields and varying temperatures between ions and electrons may be present [30, 31, 39]. The result is a theoretical formulation for gradient-driven species separation that can be expressed in terms of the lighter ion species' diffusive mass flux, assumed in the center of mass frame of a binary-ion plasma as shown in Equation 1.1 [30, 31, 39].

Adopting the center of mass frame, this formalism suggests that light and heavy species diffuse in opposite directions, which presents as the light species concentrating at the shock front in the lab frame, as shown in Figure 1.4 [7, 23]. This transport process may be driven through baro-diffusion, thermo-diffusion and electro-diffusion, which is governed by gradients in total ion pressure ($\nabla log(P_i)$), mass averaged ion temperature ($\nabla log(T_i)$), and electrostatic potential ($\nabla\phi$), respectively [30, 31, 39]. The strength of each diffusion mechanism is represented by the corresponding diffusion ratio (k term) [23, 30, 31, 32]. Tractable analytic solutions are available in literature for k_p and k_e, which are thermodynamic quantities that do not depend on plasma collisionality [23, 30, 31]. Thermo-diffusion ratios however, are kinetic quantities whose calculation relies on the use of a collisional-model [23, 30, 31].

$$\mathbf{i} = -\rho D\Big(\nabla c + k_p \nabla \log p_i + \frac{ek_E}{T_i}\nabla\Phi + k_T^{(i)}\nabla \log T_i + k_T^{(e)}\nabla \log T_e\Big) \tag{1.1}$$

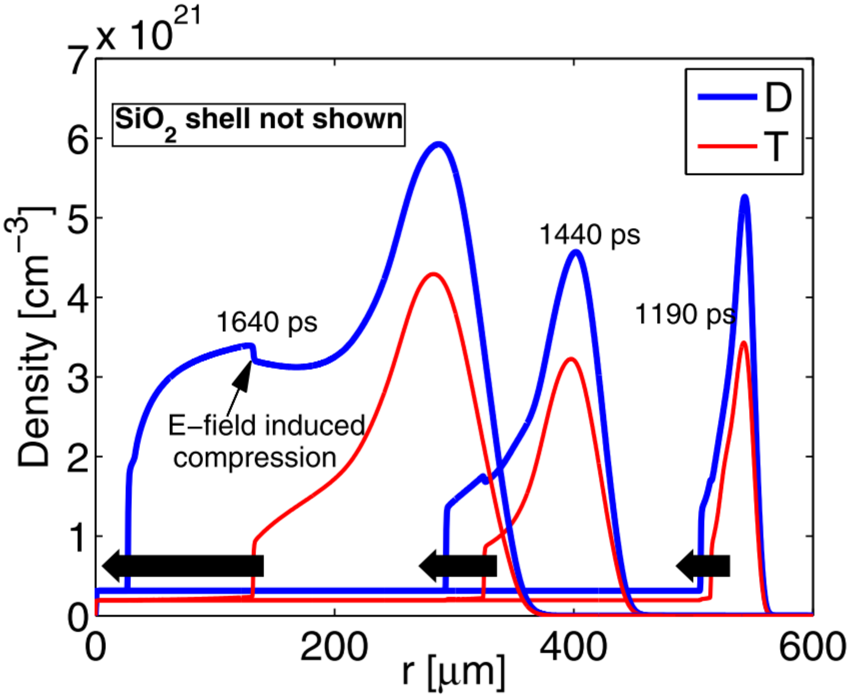

Figure 1.4: Multi-fluid simulations of a deuterium-tritium plasma shock present in ICF implosions predict that gradient-driven species separation results in spatial dephasing of the light (deuterium) and heavy (tritium) ion components [7]. Image reprinted from Ref. [7]: C Bellei, PA Amendt, SC Wilks, MG Haines, DT Casey, CK Li, R Petrasso, and DR Welch. Species separation in inertial confinement fusion fuels. Physics of Plasmas, 20(1):012701, 2013, with the permission of AIP Publishing.

1.5 Shocks in Type-II supernovae explosions

An enhanced understanding of shock physics is also critical to the study of type-II supernova explosions. Supernova explosions occur at the end of a star's life, where it has exhausted its nuclear fuel [43]. Without the energy and pressure provided by fusion reactions, the plasma core of the star collapses under the force of its own gravity [43]. This core collapse occurs so quickly that it launches outward propagating shock waves that drives nucelosynthesis in the star's outer layers, producing elements such as iron [44].

In some cases, the outward propagating shock will stagnate, and as the star continues to collapse, a black hole will form [44]. In other cases, the shock wave will result in shedding of the star's outer layers, resulting in the formation of a neutron star [43, 44]. Understanding the role of the outward propagating shock wave on the evolution of fusion burn and the outcome of these supernovae events is an area of active research [43, 44]. Laboratory plasma physics experiments provide a unique opportunity to study plasma shocks on more accessible spatial and temporal scales that are scalable to their astrophysical counterparts. So while understanding plasma shocks is crucial to the progress of fusion experiments, their presence in complex physical and astrophysical scenarios further justify their study in an experimental setting.

1.6 Experimental studies on plasma shocks

While plasma shocks have been extensively studied analytically and computationally [3, 4, 30, 31, 38, 39, 45], there is a limited amount of experimental studies that can be used to benchmark predictions related to multi-ion-species effects and species separation in plasma shocks [23, 24, 32]. This is due to the temporal and spatial scales over which shocks exist, which makes a detailed study of the structure of a collisional shock very difficult [23, 24, 32]. Nevertheless, there have been a few experiments in recent years that have started to make progress on this front [23, 24, 32]. Work by Langendorf et al. has observed ion heating in collisional plasma shocks through Doppler broadening [24]. More recent work done by Chu et al. has taken this a step further by observing temperature separation between different ion species in a multi-ion-species shock [32]. These observed heating effects certainly play a role in the diffusive mass flux of the various ion species in a plasma shock, and are crucial to correctly estimating the strength of the various diffusion mechanism within a plasma shock. [30, 31].

With regards to species separation, Byvank et al. performed high-speed imaging of obliquely merging supersonic Ar-He jets to infer species separation on the order of ≈ 7 mm between the two ion species at the shock front [23]. Chu et al. have also used emission spectroscopy to infer differing diffusion velocities of lighter (N) and heavier (Ar) species within plasma shocks resulting from the head-on-collision of supersonic plasma jets [32]. While this work did not directly observe species separation, the differing diffusion velocities between the light and heavy ion species near the shock front implies the presence of species separation at the shock front [32].

These two studies in particular have been some of the first to experimentally characterize species separation in plasma shocks [23, 32]. However, each of these studies have limitations that the experiments in this dissertation aim to address. In particular:

- These experiments involve collisions of plasmas with low electron densities ($\approx 10^{14} cm^{-3}$) [23, 32]. No experiments have investigated species separation in denser plasmas.
- Despite dealing with radially unconstrained, three dimensional setups, these experiments relied on chord integrated measurements [23, 32]. Investigations of the shock structure in additional spatial dimensions [26] can help to extend upon traditional one-dimensional plasma shock theory to help us understand and model more realistic plasmas.
- These experiments focused solely on binary ion plasmas [23, 32]. Laboratory plasmas can often involve additional ion species due to the presence of impurity elements that become ionized during the experiment [15, 19]. Attempts to characterize the diffusive mass fluxes in plasmas with three or more ion species can help to expand traditional binary ion fluid diffusion theory [30, 31, 42].

These topics have interest have helped to formulate a series of experimental campaigns that has utilized spatially resolved spectroscopy to characterize the atomic number density distributions of three prominent ion species in a multi-ion-species plasma shock. These results build upon the work done on the topic by Byvank and Chu [23, 32], while providing scale-able results that can be used to benchmark, validate and expand upon theoretical and computational models relevant to plasma shocks in astrophysical, fusion, and laboratory settings.

1.7 Organization of the remainder of this dissertation

Chapter 2 of this dissertation describes in detail the experimental apparatus, plasma diagnostics and analysis techniques used in the experimental campaigns reported on in Chapters 3 and 4. These analysis techniques involve the use of emission spectroscopy, and heterodyne interferometry [14], and serve as the foundation for the work described in the subsequent chapters. Chapter 3 reports the identification of ion shock layers formed from the collision between a supersonic plasma jet and a quasi-stagnant background plasma. These shocks are shown to exist in a semi- to fully-collisional regime, and are diagnosable over spatial scales of a few hundred mean-free-paths. Due to the large gradients in ion density across the shock front, barodiffusion is the dominant driver of diffusive mass flux in these experiments. The results from this campaign have been formally published in Ref. [15], and have informed the campaign reported on in Chapter 4, where shocks are induced in multi-ion-species plasma jets to diagnose the physics of multi-ion-species plasma shock structures on spatial scales that have not been reported in the literature up to this point. Chapter 5 reflects on the results of these campaigns, while presenting potential research directions that can leverage the resources and results from this work to further our understanding of fundamental plasma physics phenomena.

Chapter 2

Experimental apparatus and diagnostic overview

2.1 Experimental Plasmas and Propulsion Laboratory

The following experiments were performed at Virginia Tech's Experimental Plasmas and Propulsion Laboratory, which is presently located on Virginia Tech's Blacksburg campus. A pulsed plasma-armature railgun (Figure 2.1) was used as a platform for forming and studying the physics of colliding plasma jets [8, 15, 17]. Neutral gas puffed between the rails of the railgun is broken down and accelerated down the z-axis of a cylindrical vacuum chamber due to the $\vec{J} \times \vec{B}$ force resulting from the discharge of an underdamped current pulse across the railgun via a pulse forming network (PFN) [8, 15, 17, 46].

A typical current pulse supplied to the railgun has a peak current of 100 kA and a ringing frequency of 30 kHz, which results in the formation and acceleration of multiple jets within a single discharge cycle [8, 15, 17]. Previous experiments performed with this apparatus [8, 17] have extensively studied the first jet emitted from the railgun, demonstrating repeatable formation of a low temperature, highly supersonic plasma, which is favorable for the study of collisional plasma shocks. We induce collisions within a single experimental "shot" by installing a polycarbonate obstruction downstream the muzzle of the railgun; the first jet collides with the obstruction, forming a diffuse background that subsequent jets can collide

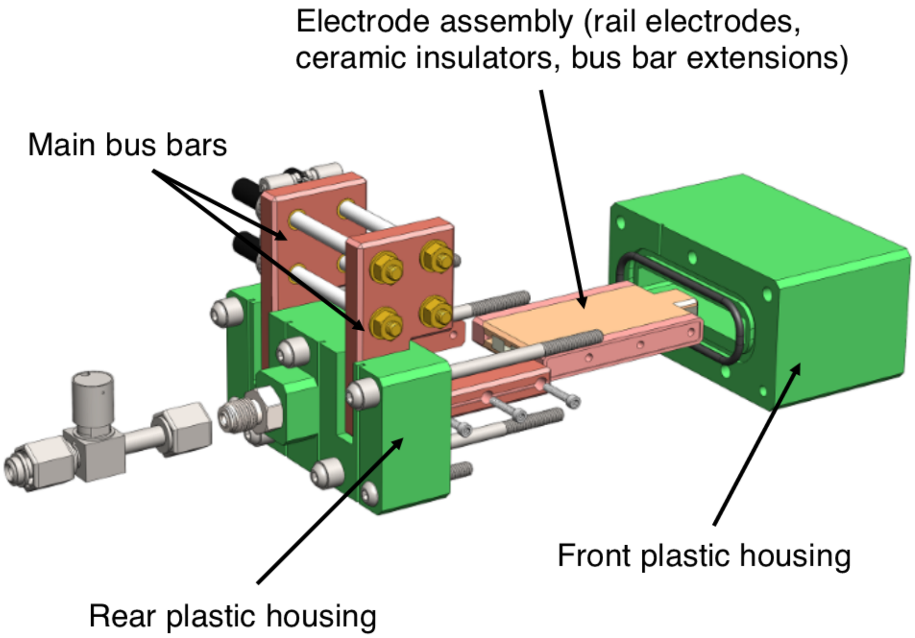

Figure 2.1: Exploded view of linear plasma-armature railgun utilized to form and accelerate plasma jets. Image from Ref. [8]. The electrode assembly consists of two tungsten-copper electrodes sandwiched in between two ceramic insulators, forming a bore that is approximately 5 mm wide and 3.5 mm tall. Gas is puffed into the electrode assembly through the use of a Parker-Hannifin high speed dispense valve, which is overdriven to achieve opening and closing times on the order of milliseconds. Coaxial transmission lines deliver current from the PFN to copper bus bars which connect to the electrode assembly. These components are encased in a PEEK housing.

with [8, 15]. The following experiments characterize the interaction between the supersonic second jet and stagnated first jet, which has been shown to consistently occur during each shot [8, 15].

2.2 Diagnostic overview

A suite of diagnostics non-intrusively characterizes the collision event from outside the vacuum chamber. Diagnostic access is provided through the use of eight 30 cm quartz viewports, whose line of sight intersects the z-axis of the chamber. The primary diagnostics include a Rogowski coil, a heterodyne Mach-Zehnder interferometer [1], and a high spatial resolution survey spectrometer coupled with an image-intensified CCD camera that serves as the spectrometer detector while also being used for fast photography. The Rogowski coil and interfermeter signals are digitized with an 8-channel National Instruments PXIe oscilloscope at a sampling frequency of 60 Mhz, allowing for temporally resolved measurements during a single shot. The iCCD and spectrometer are only capable of time-gated measurements, thus measurements from multiple shots must be taken with these diagnostics to infer the temporal evolution of plasma parameters.

2.2.1 Rogowski coils infer PFN discharge current

Rogowski coils are magnetic field diagnostics that can infer the temporal profile of transient current pulses [9, 10] . A Rogowski coil, pictured in Figure 2.2 consists of solenoidal windings wrapped as a torus [9]. In the railgun experiment, a single Rogowski coil is placed around the transmission lines which delivers current from the PFN to the railgun [8, 15, 17]. Rogwoski coil measurements have shown consistent PFN performance from shot to shot, with repeatably observed current profiles [8, 15, 17]. In practice, Rogowski coil measurements are primarily used to identify temporal jitter from shot to shot, allowing us to define our reference time, t = 0 as the time which the discharge event begins [8, 15, 17]. An example is shown in Figure 2.3.

2.2.2 Fast photography images the experiment

A Princeton Instruments PiMAX4 1024 × 1024 pixel intensified charged-coupled device (iCCD) is employed to visualize the experiment in the visible-ultraviolet (VUV) emission

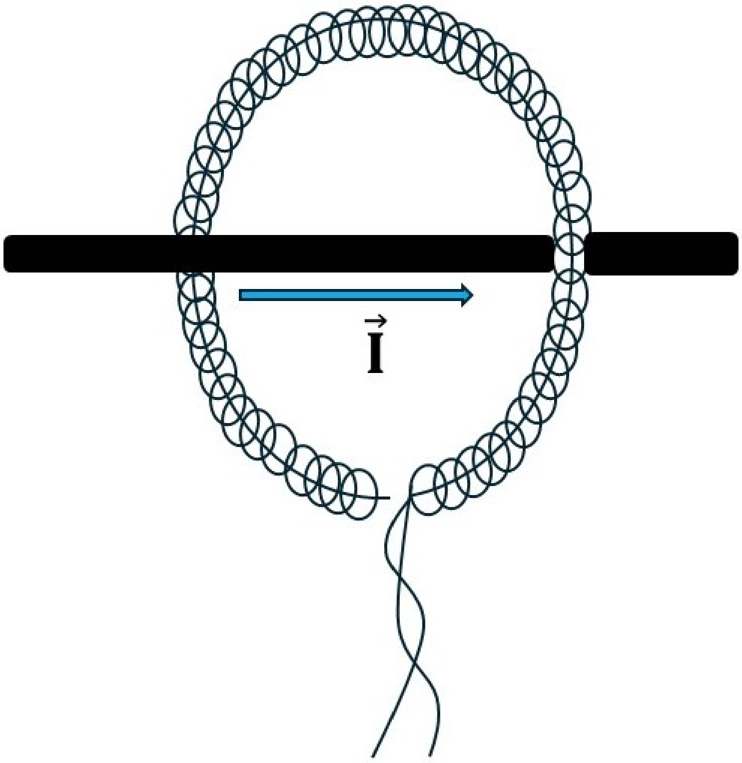

Figure 2.2: Sample Rogowski coil. Drawing based on model from Image from Ref. [9]. The working principle of Rogowski coils rely on the use of Ampere's and Faraday's law [9, 10]. When a current carrying wire is traveling through the torus, Ampere's law dictates that the associated magnetic field travels around the toroidal axis [9, 10]. Farady's law then governs the resulting voltage induced across the coil as a result of the changing magnetic flux through the windings [9, 10]. This measured voltage is proportional to the time-derivative of current flowing thorugh the coil, with the constant of proportionality determined by the geometry and construction of the coil itself [9, 10]. Our Rogowski coil voltage measurements are digitally integrated through a trapezoidal numerical method to infer current traveling to the railgun during the discharge event.

band using time gated exposures [8, 11, 15, 17]. Image intensification is achieved through an assembly consisting of a photocathode, microchannel plate and phosphor screen (see Figure 2.4) and can be used to improve each image's signal-to-noise ratio [11]. Time gated

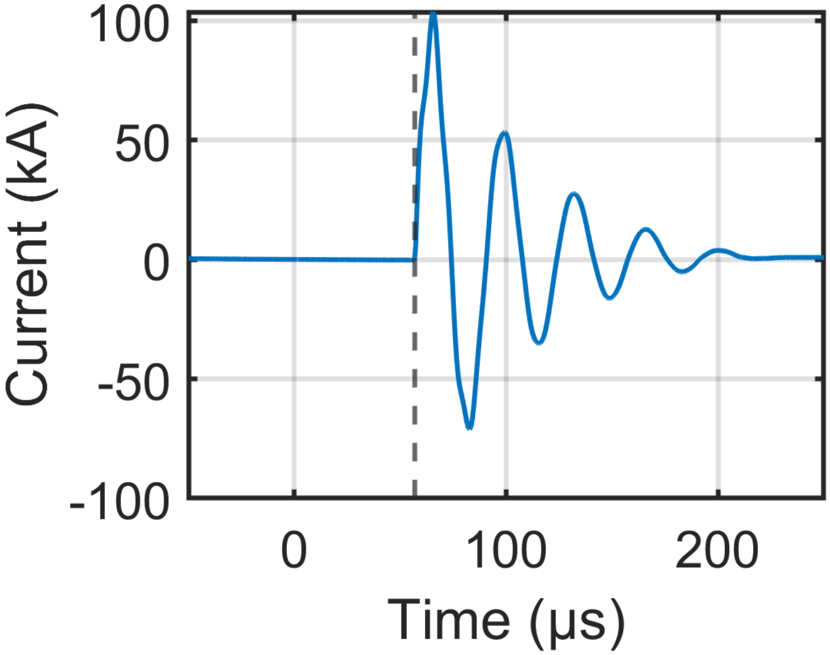

Figure 2.3: Rogowski-inferred current associated with discharge 2026. This observed current profile is representative of all shots reported on in this dissertation, exhibiting an underdamped profile with a ringing frequency of 30 kHz and peak current of ≈ 100 kA. This shot in particular exhibits a noticeable delay in time from when the experiment is set to fire at Time $= 0$ μs. As mentioned above, this temporal jitter is associated with the performance of the PFN. Rogowski coil measurements allow us to assign our reference time to the moment right before a large increase in current occur, as indicated by the dashed vertical line.

operation means that photons are accumulated on each pixel during the image exposure time [11, 21]. However, the use of an electronic shutter results in the use of exposure times as low as 3 ns [11], eliminating the effect of motion blur as plasma jets travel through the vacuum chamber. Pairing the iCCD with a 25 mm f8 lens allows for ”freeze-frame” imaging of the experiment, spanning the length and diameter of the vacuum chamber [8, 11, 15, 17].

The images presented in this dissertation were captured with the iCCD placed atop the vacuum chamber as shown in Figure 2.5, with its optical axis normal to the jet propagation axis.

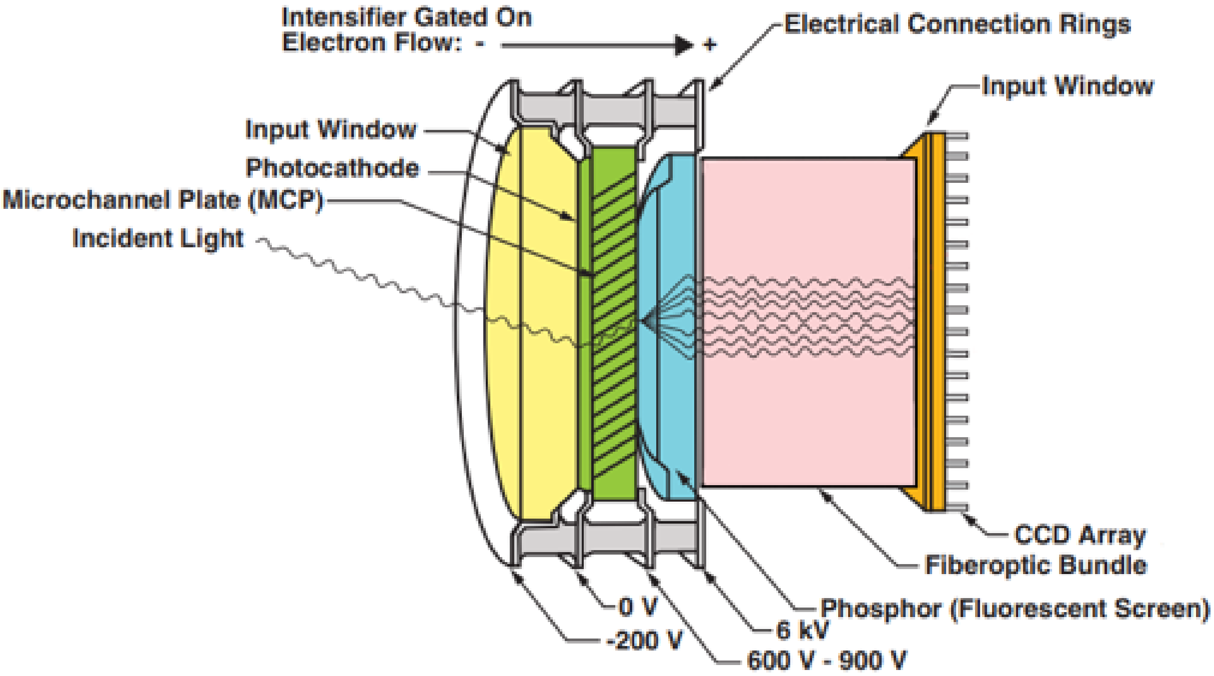

Figure 2.4: The internal workings of a CCD. Image from Ref. [11]. Photons incident on the photocathode are converted into photoelectrons [11]. Upon hitting the microchannel plate, the photoelectrons are multiplied into an electron cloud which are then converted back into photons once passing through the phosphor screen [11]. This multiplied cloud of photons then hit the detector, which generates an intensified signal [8, 11].

2.2.3 Multi-Chord interferometery and Abel inversions

A multi-chord heterodyne Mach-Zehnder interferomter [1, 13, 14, 16] provides estimates of chord-integrated electron density. A laser beam is split into a probe bean and reference beam that has been up-shifted by a frequency of 80 MHz [8, 15, 17]. After passing through the plasma, the probe beam recombines with the reference beam, forming a 80 MHz beatwave [1, 13, 14, 16]. Processing [1, 8, 12, 13, 14, 15, 16, 17] of this signal yields as shown in Figure 2.6 yields un-ambiguous measurements of phase shift relative to the reference beam. These measurements are related to electron density integrated across the path length of the probe beam, as defined by [1, 8, 10, 12, 13, 14, 15, 16, 17]:

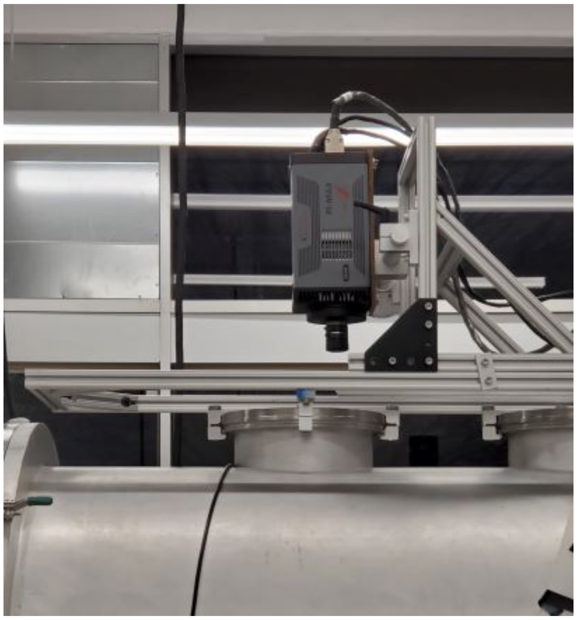

Figure 2.5: Typical iCCD arrangement for the results presented in this dissertation. A mount designed of 80/20 strut material is used to secure the camera to the chamber.

$$\Delta\phi = C\int n_e dl, \tag{2.1}$$

The analytic expression for C is given by $\frac{e^2\lambda}{4\pi\epsilon_0 m_e c^2}$ [1, 8, 10, 12, 13, 14, 15, 16, 17] . Typical interferometer chord arrangement involves two probe beams traveling across the diameter of the vacuum chamber, normal to the jet propagation axis. Each chord provides line-integrated density measurements at two axial stations along the chamber. These measurements are used to quantitatively characterize the various features observed within a single shot.

Because studies involving plasma shocks often deal with non-uniformities, we must deconvolve localized values of electron densities from our chord-integrated phase shift measurements [10]. This can be achieved by taking chordal measurements along the radial profile of the plasma [1, 26, 27]. Given an interferometer setup where a total number, i_{tot} of these sightlines are inferring chord integrated electron density along the radial profile of an

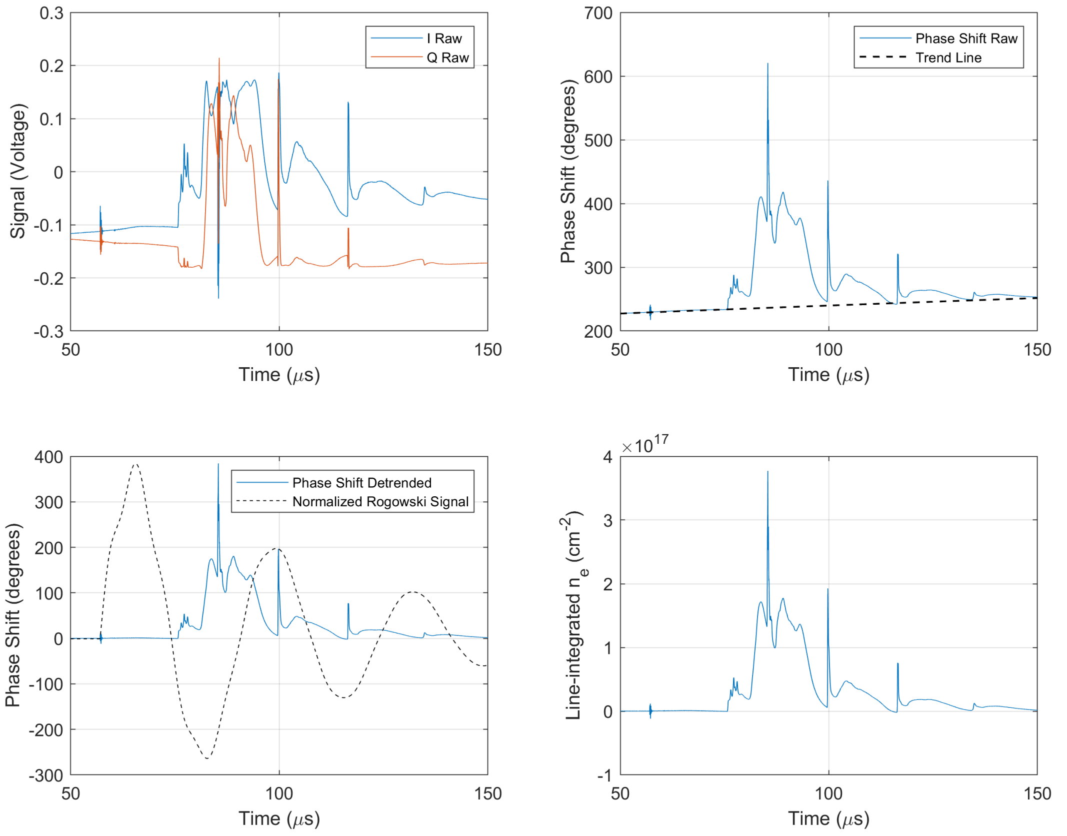

Figure 2.6: Interferometer analysis procedure [1, 8, 12, 13, 14, 15, 16, 17] applied to measurements phase shift measurements for discharge 2026. Measurements returned by the interferometer system are I, Q demodulated components of the phase shift, which respectively correspond to the cosine and sine components of the phase shift [1]. The four-quadrant inverse tangent of Q/I [1] is used to determine phase shift, which is presented in degrees in the top-right figure. The phase shift due to the plasma is then isolated from contributing sources of phase shift by subtracting a polynomial fitted baseline from the total phase shift [1], as shown in the bottom left figure. This detrended phase shift is then converted to line-integrated density in cm^{-2} through Equation 2.1 [1]

axisymmetric plasma column, the chords are assumed tangential to regions of constant density [1, 26, 27], such that the number of radial zones, j_{tot} is equivalent to the total number of sightlines, $i_{tot} = j_{tot}$. This model, used in the analysis carried out by Gornushkin et al. [27], is employed to study infer volumetric electron density in our plasma jets. Crucial to this analysis is the determination of the length matrix, $L_{i,j}$, which determines the chord length of sightline 'i' through radial zone 'j' in one quadrant of the plasma [1, 26, 27]. The analytic form of $L_{i,j}$ can be determined from geometric principles [1, 26, 27], as shown in Appendix A.2. The length matrix is used to enforce a system of linear equations that relate the measured phase shifts associated with each sightline, $\Delta\phi_i$ to the desired electron densities in each radial zone, n_j through the relation [1, 26, 27]:

$$\Delta\phi_i = C \sum_j 2L_{i,j} n_{e_j}, \tag{2.2}$$

An Abel-like matrix inversion can be be easily applied to Equation 2.2 to solve for n_{e_j} as [1, 26, 27]:

$$n_{e_j} = \frac{1}{2C} \sum_i L^{-1}_{j,i} \Delta\phi_i. \tag{2.3}$$

This analysis provides localized measurements of electron density which can be paired with measurements from emission spectroscopy to infer additional plasma parameters relevant to the study of plasma shocks.

2.2.4 Spatially resolved spectroscopy and PrismSPECT

When not used to image the experiment, the iCCD serves as the detector for a 750 mm high spectral resolution survey spectrometer to measure plasma line radiation. The use of interchangeable diffraction gratings (300, 2400 and 3600 g/mm) allow for spectral dispersion between 5 and 50 pm per pixel. Spatially resolved collection optics were designed that projects plasma radiation onto a linear array of seven fibers with a core diamter of 200 μm [8, 15]. The use of spatially resolved collection optics alongside low exposure times afforded by the iCCD result in the collection of emission spectra with millimeter spatial resolution and nanosecond temporal resolution, allowing for detailed analysis of the evolution of line radiation [15].

Within a typical experimental spectrogram, such as the one shown in Figure 2.7, there are numerous lines of interest. The most abundant lines belong to the working gas supplied to the railgun, which is either argon (See Ch. 3) or a mix of argon and nitrogen (See Ch. 4). Additional lines represent impurity species ablated from plasma facing railgun material during each discharge cycle [8, 15, 17]. Of the various impurity species, aluminum originating from the railgun insulator material [47] is the most prominent.

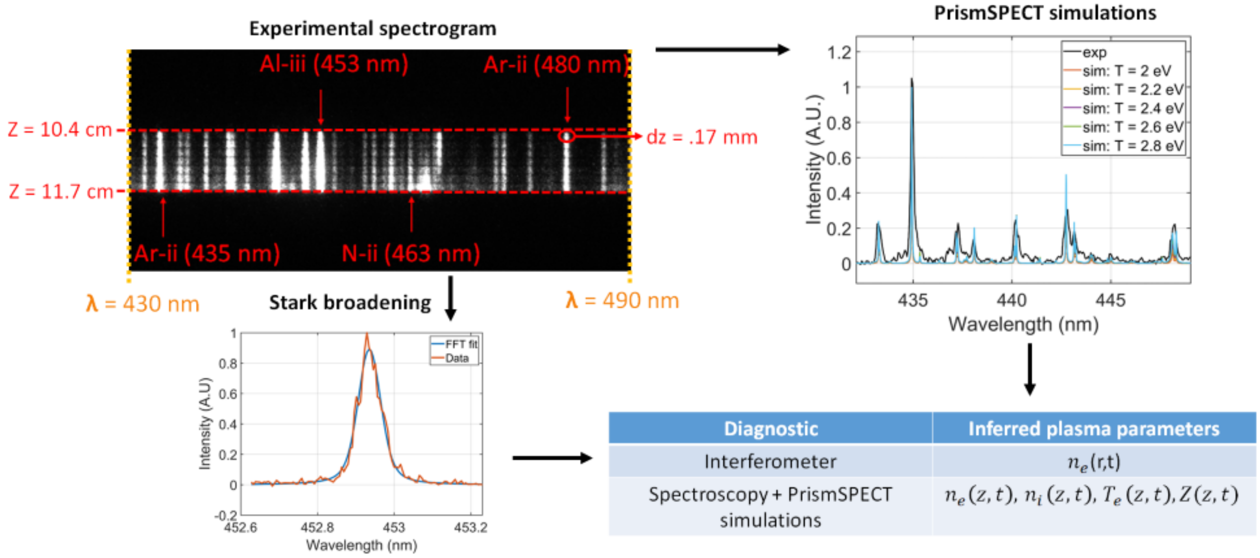

Diagnostic	Inferred plasma parameters
Interferometer	n_e(r,t)
Spectroscopy + PrismSPECT simulations	$n_e(z,t)$, $n_i(z,t)$, $T_e(z,t)$, $Z(z,t)$

Figure 2.7: Raw measurements (top left) and parameter inferences (remaining three) from the spectrometer diagnostic. A typical iCCD image of an energized railgun shot displays lines attributable to the working gas supplied to the railgun, as well as impurities (notably aluminum) that are ablated from the plasma facing railgun components. These raw measurements as well as PrismSPECT simulations [1, 12, 13, 15, 16, 18, 19] and stark broadening [1, 10, 15, 20, 21] line fitting techniques are employed to infer a suite of spatial and temporal plasma parameters that can be compared with interferometer measurements to assess jet collisionality and collisional shock physics. This data analysis framework is extensively used to produce the results discussed in the remaining chapters of this dissertation.

In addition to identifying plasma composition, experimental spectrograms aid in the inference of a variety of plasma parameters. Of particular interest are estimates of ion density, electron temperature, and mean charge state which are obtained using experimental spectrograms and corresponding phase shift measurements in concert with non-LTE collisional radiative modeling performed with PrismSPECT spectral modeling software [1, 12, 13, 15, 16, 18, 19]. By taking ion density as input, these simulations model line radiation of an optically thin low temperature plasma with a Maxwellian electron energy distribution function for a given range of electron temperatures [18].

Because phase shift measurements provide inferences of electron density, an iterative procedure is employed for PrismSPECT analysis (see Figure 2.8) [1, 12, 13, 15, 16, 18, 19]. At the start of the analysis, ion density is assumed equivalent to the electron density inferred through interferometer measurements [1, 12, 13, 15, 16, 18, 19]. This initial guess of ion density is used as input to the PrismSPECT simulations to model plasma line radiation for a range of possible electron temperatures [1, 12, 13, 15, 16, 18, 19]. These simulations are then used obtain enveloped estimates of T_e and $\bar{Z}$ based on the presence or absence of simulated lines when compared to the experimental spectrogram [1, 12, 13, 15, 16, 18, 19]. The estimate of $\bar{Z}$ is used alongside the quasi-neutrality condition [29] to update the estimate of ion density [1, 12]. Convergence is declared if the updated estimate of n_i is within ten percent of the guess at the beginning of an iteration [15]. In practice, roughly two to three iterations must be performed before convergence is achieved [15]. This method is used extensively in Ch. 3 [15].

Additionally, line profile measurements taken using higher order diffraction gratings are used to infer localized inferences of electron density through measurements of Stark broadening [10, 20, 21]. Line-radiation as measured by a spectrogram is not infinitely narrow [10, 21]. Rather, the line profile has a finite width as a result of instrumental and physical broadening mechanisms [10, 20, 21]. Of the various physical broadening mechanisms that take

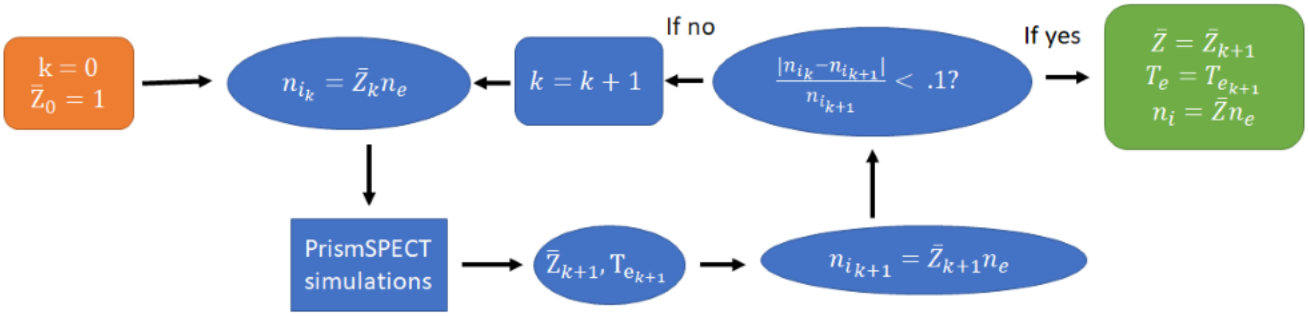

Figure 2.8: Block diagram detailing the iterative analysis procedure [1, 12, 13, 15, 16, 18, 19] that is used to infer n_i using the spectrometer and interferometer measurements in concert with on another. This analysis is extensively used in Section 3.6 [15].

place, Doppler and Stark broadening tend to dominate [10, 20, 21]. In the case of Doppler broadening, a Maxwellian ion distribution results in ions moving towards and away from the collection optics' line-of-sight, blue- and red- shifting the radiated line emission, which presents as line broadening [10, 20, 21]. A Doppler-broadened line follows a Gaussian profile, whose analytic form is provided as [20]:

$$G(\lambda) = A_G \exp \frac{-4\ln(2) \times (\lambda - \lambda_0)^2}{W_G^2}. \tag{2.4}$$

Where W_G is the Doppler FWHM, which can be used to infer ion temperature as [20]:

$$W_G = \frac{\lambda_0}{c}\sqrt{\frac{k_B T_i \times 8\ln(2)}{m_i}} \tag{2.5}$$

Given the high plasma jet densities inferred in previous campaigns [8, 15, 17], Stark broadening is often the dominant broadening mechanism. Stark broadening is the result of perturbative effects on a radiating atom due to neighboring particles [10, 20, 21]. In the quasi-static approximation, the dominant perturbation is due to the plasma microfield of neighboring ions, which often results in an asymmetric line profile [10, 20, 21]. In the electron impact regime, Coulomb collisions with neighboring electrons interrupt the wave train of the emitting ion, resulting in a symmetric Lorentzian line profile of the form [10, 20, 21]:

$$L(\lambda) = A_L \frac{W_L^2}{4(\lambda - \lambda_0)^2 + W_L^2} \tag{2.6}$$

Where W_L is the corresponding Stark width [20]. In practice, a line profile will often have the analytic form of a Voigt profile, which is the convolution of Doppler-broadened Gaussian profiles with Stark-broadened Lorentzian profiles [10, 20, 21]. If only one of these broadening mechanism are present, then the line profile resembles the form associated with the dominant source of broadening [10, 20, 21]. Because broadening due to instrument effects can also take the form of a Voigt profile, experimentally observed spectra have an analytic line profile of [10, 20, 21]:

$$V(\lambda) = \int G(\lambda - \lambda')L(\lambda')d\lambda'. \tag{2.7}$$

Where the total Gaussian FWHM is given as [10, 20, 21]:

$$W_{G_{Tot}} = \sqrt{W_{G_{Doppler}}^2 + W_{G_{Inst}}^2} \tag{2.8}$$

And the Lorentzian FWHM is given as [10, 20, 21]:

$$W_{L_{Tot}} = W_{L_{Stark}} + W_{L_{Inst}} \tag{2.9}$$

By fitting the functional form of a Voigt profile to experimental data, optimized values of W_G and W_L can be inferred and isolated from instrumental effects, allowing for inference of ion temperature and electron density [10, 20, 21]. In practice, Doppler broadening is often un-resolvable in low temperature plasmas [10, 20, 21]. For ionized atoms, collisional Stark broadening due to electron impact effects dominate, and the inferred Stark width relates to electron density as [10, 20, 21, 22]:

$$W_{L_{Stark}} = \omega \frac{n_e}{n_e^{ref}}, \tag{2.10}$$

Where ω is an independent measurement of a Stark width taken at a reference electron density n_{ref} [48, 49]. Through this linear relation between Stark width and electron density, spatially resolved highly localized measurements of electron density can be obtained through the spectrometer diagnostic [15].

In addition to this traditional Voigt fit in wavelength space, fits to line profiles can also be done in Fourier space [20]. In Fourier space, the Fast Fourier Transform (FFT) of a Voigt profile is simply the product of the FFTs of a Gaussian and Lorentzian, as shown in Equation 2.11 [20]. Voigt fitting in wavenumber space offers some benefits to traditional wavelength fitting of experimental line profiles. The fitting function is simpler in wavenumber space, and wavenumber space allows for the possibility of spectral filtering to fit noisy signals [20]. However, the quality of the fit in FFT space has a slight dependence on sample size, as this affects wavenumber resolution [50]. Conversely, traditional wavelength fits are more sensitive to signal noise, but are relatively independent of sample size [20]. Thus, fits to experimental spectra are often run in both FFT and λ space to provide independent inferences of localized n_e [15]. The agreement or disagreement between these two fitting procedures are then used to aid in the interpretation of these results [15].

$$V(k) = A_v \exp\left(\frac{-W_G^2 k^2}{16 \ln 2} - \frac{W_L |k|}{2}\right) \tag{2.11}$$

By using these analysis techniques in coordination with interferometry measurements, the temporal and spatial evolution of plasma parameters such as ion/electron density, electron temperature, and mean charge state can be inferred. These parameters provide insight into the physics of colliding plasma jets and can be used to quantitatively study the structure of collisional plasma shocks

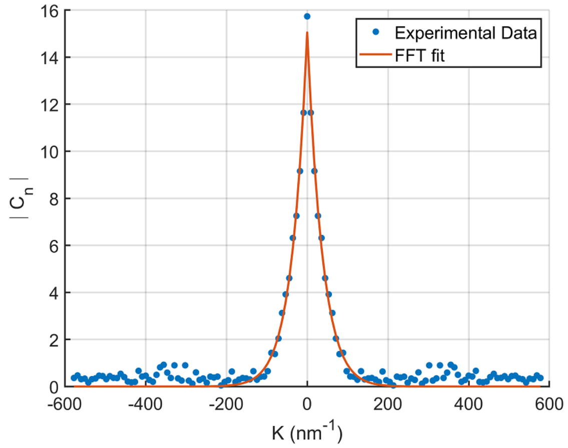

(a) Voigt fit in Fourier space to Ar-II line emission observed in shot 1800.

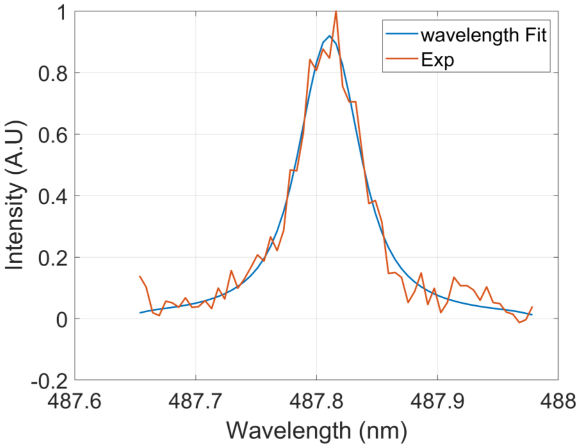

(b) Voigt fit in wavelength space to the same line in Figure 2.9a

Figure 2.9: Fits to measured line-emission in both wavelength and Fourier [10, 20, 21, 22] space provide an opportunity to infer localized measurements of electron density through independent fitting techniques. This analysis is a crucial part of the work performed in Chapter 4. Figure (a) reproduced from Ref. [15] AI Mohammed and CS Adams. Ion shock layer formation during multi-ion-species plasma jet stagnation events. Physics of Plasmas, 29(7):072307, 2022., with the permission of AIP Publishing

Chapter 3

Evidence of ion shock layer in collisions of argon plasma jets

This chapter[1] describes the results of an experimental campaign that has identified ion shock layers that result from the collisions of argon plasma jets, using the linear railgun plasma source and associated diagnostics. These results have been used to evaluate the ability of the present experimental setup to observe and characterize gradient- driven ion species diffusion, while also serving as the foundation for the work presented in Chapter 4.

3.1 Experimental setup

As discussed in Chapter 2, this experiment focused on characterizing the collision event between the second jet in railgun discharge cycle, and the first jet, which has been stagnated using a polycarbonate obstruction. We place the obstruction at two locations, $z_{pc} = 12$ cm and $z_{pc} = 17$ cm, which are measured relative to the muzzle of the railgun. A working gas of argon was supplied to the railgun, which upon breakdown, produces plasma jets that are primarily argon, along with impurity elements ablated from the railgun during discharge. Adopting methodology from Moser et al. [19], jet composition was estimated

---

[1] The results presented in this chapter have been published in Ref. [15]: AI Mohammed and CS Adams. Ion shock layer formation during multi-ion-species plasma jet stagnation events. Physics of Plasmas, 29(7):072307, 2022., Reprinted and reproduced with the permission of AIP Publishing.

by measuring the difference in vacuum chamber pressure rise between neutral-gas-injections and shots where the railgun was energized. From this analysis we estimate the individual jet composition as 86 % argon by molar percentage, with the impurity material consisting of carbon, hydrogen, and oxygen (which originate from the PEEK plastic railgun housing), and boron, aluminum, and nitrogen (which originate from the insulator assembly [47]) [8, 17].

Figure 3.1 [8, 15] below depicts the diagnostic setup used for this campaign. Of particular importance is the $z_{pc} - z = 1$ cm axial station, which was probed at various radial stations through interferometry. Spectrometer viewing chords were arranged to provide a top-down measurement of line-radiation, with one viewing chord co-incident with the $z_{pc} - z$ $= 1$ cm station. Each viewing chord was approximately 2 mm in length, with chord locations provided in Table 3.1 for each experimental configuration. Three sets of experiments were conducted; two characterized the collision event at $z_{pc} - z = 1$ cm for the two different z_{pc} locations, while the third measured the properties of the unobstructed plasma jets as they traveled through axial stations farther away from the obstruction.

3.2 Fast-photography images of the collision event

False-color, logarithmically scaled VUV images of the experiment presented in Figures 3.2 and 3.3 are used to visualize the evolution of a single discharge cycle for the $z_{pc} = 12$ cm and $z_{pc} = 17$ cm cases, respectively. To reduce the effect of shot-to-shot jitter, image time, $t - t_0$, is presented relative to the post-collision plasma transit time as measured in the $z_{pc} - z = 1$ cm, y = 0 cm interferometer chord (see Figure 3.4). Three distinct phases of the experiment are observed in the images from both obstruction locations. Initially, the first jet travels unobstructed towards down the image, towards the obstruction. Upon impact, the first jet stagnates, forming a background plasma that expands radially and

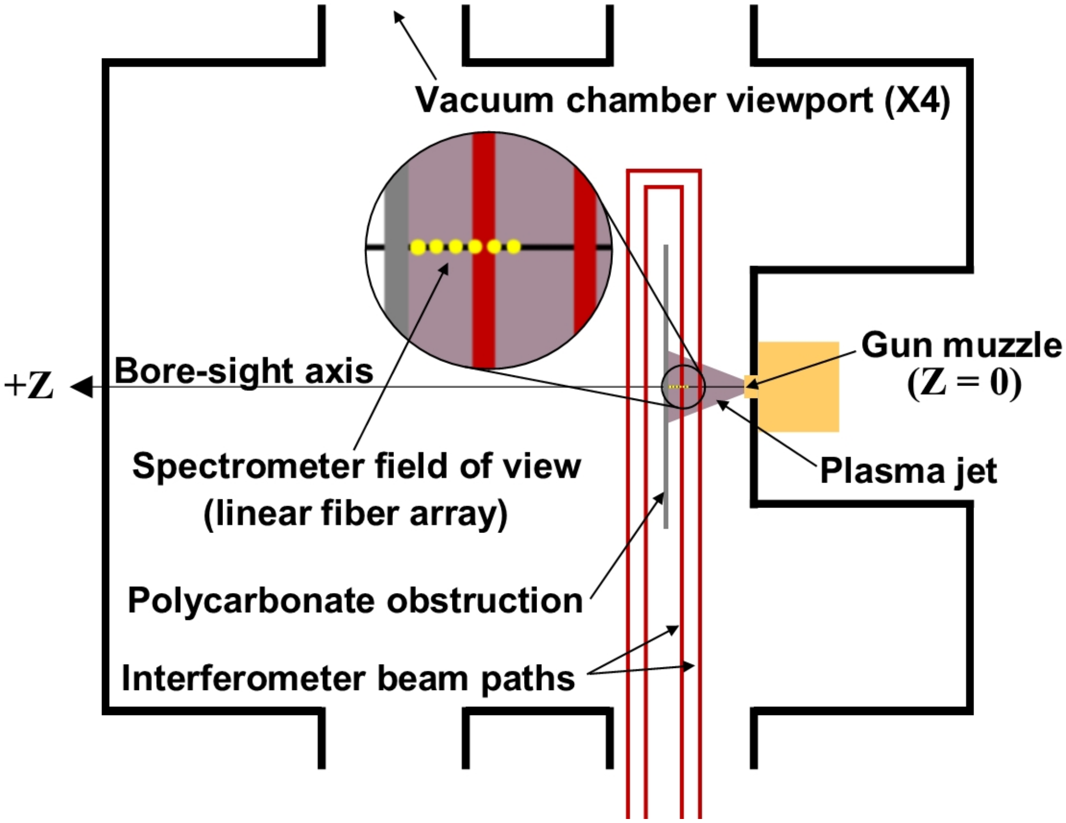

Figure 3.1: Vacuum chamber cross section and associated coordinate system from a top-down perspective. Image from Ref. [8, 15]. Origin is chosen to be the muzzle of the railgun, from which the polycarbonate and interferometers chord are located at downstream axial stations (to the left of the image). Interferometer chords are launched into the chamber from the viewports on the side, while spectrometer viewing chords are mounted over top the chamber so that these two diagnostics can be used simultaneously with one another to characterize the plasma jets as they travel down the z-axis/bore-sight axis.

back towards the muzzle of the gun. As this occurs, the second jet is ejected from the railgun and travels towards the background plasma. The collision between the second jet and background plasma forms a structure with strong emission in the VUV band. The appearance of this post-collision plasma is concurrent with a gradient in chord-integrated electron density, inferred from interferometer phase shift measurements.

These images provide additional insights into the geometry of the plasma jet emitted from

Table 3.1: Viewing chord information relevant to the spectrometer diagnostic for the experiments performed in this chapter. Throughout this experimental campaign, a spatial resolution of ≈ 2 mm is maintained.

Experimental config. (cm)	Fiber number	Chord view range (cm)
$z_{\mathrm{pc}} = 12$ (imaging collision event)	A1	11.49–11.71
	A2	11.15–11.37
	A3	10.81–11.03
	A4	10.47–10.69
	A5	10.13–10.35
	A6	9.80–10.01
	A7	9.46–9.68
$z_{\mathrm{pc}} = 17$ (imaging collision event)	B1	16.28–16.52
	B2	15.93–16.16
	B3	15.57–15.80
	B4	15.22–15.45
	B5	14.86–15.09
	B6	14.51–14.74
	B7	14.15–14.38
$z_{\mathrm{pc}} = 17$ (imaging unobstructed jets)	C1	11.79 – 11.99
	C2	11.50 –11.70
	C3	11.21 – 11.41
	C4	10.93 – 11.13
	C5	10.64 – 10.84
	C6	10.35 – 10.55
	C7	10.07 – 10.27

the railgun. As seen in both sets of images, the unobstructed jets are wider than they are thick, with a distinct leading edge. The post-collision material has a notably curved leading edge, resembling a bow-shock.

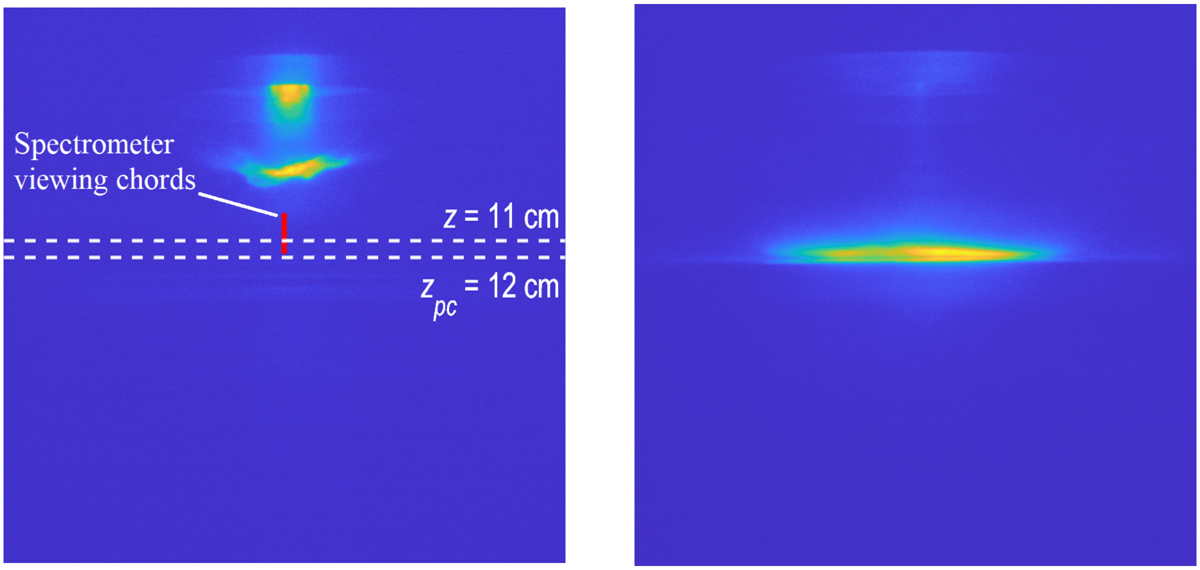

(a) $t - t_0$ = -12.77 μs

(b) $t - t_0$ = -5.32 μs

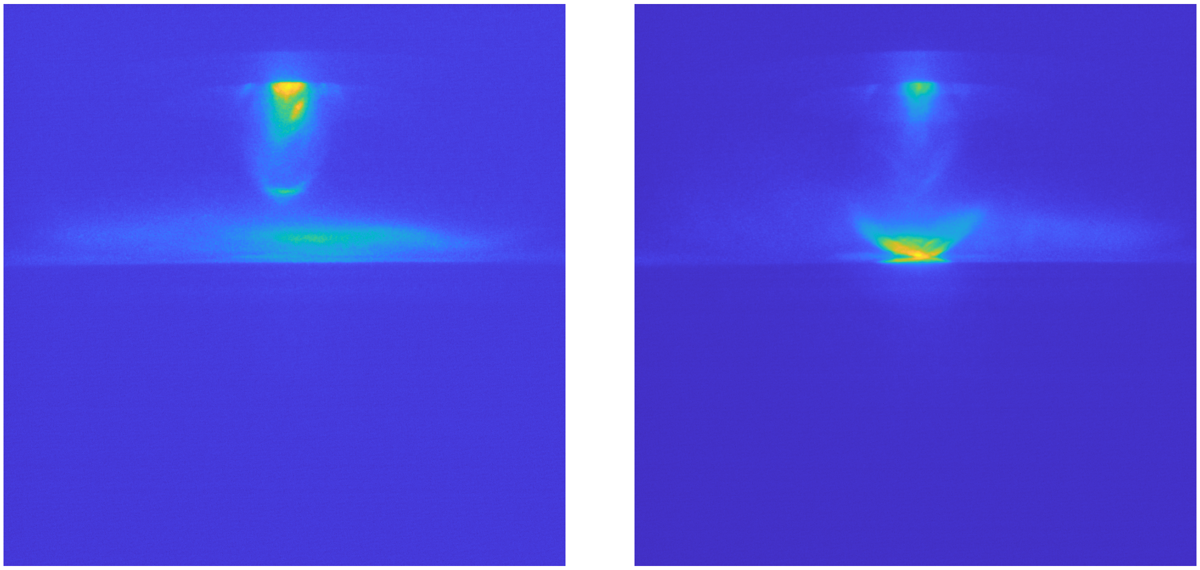

(c) $t - t_0$ = -1.30 μs

(d) $t - t_0$ = 0.02 μs

Figure 3.2: Evolution of the experiment when the obstruction is located at $z_{\text{oc}} = 12$ cm. All images are logarithmically scaled with a colormap applied to qualitatively infer plasma jet emissivity. Time is measured relative to the transit time of the post-collision plasma in the interferometer chord located at $z_{\text{pc}} - z = 1$, $y = 0$ cm. All images were collected with an exposure time of ≈ 3 ns, such that these photos are essentially freeze-frame images of the experiment.

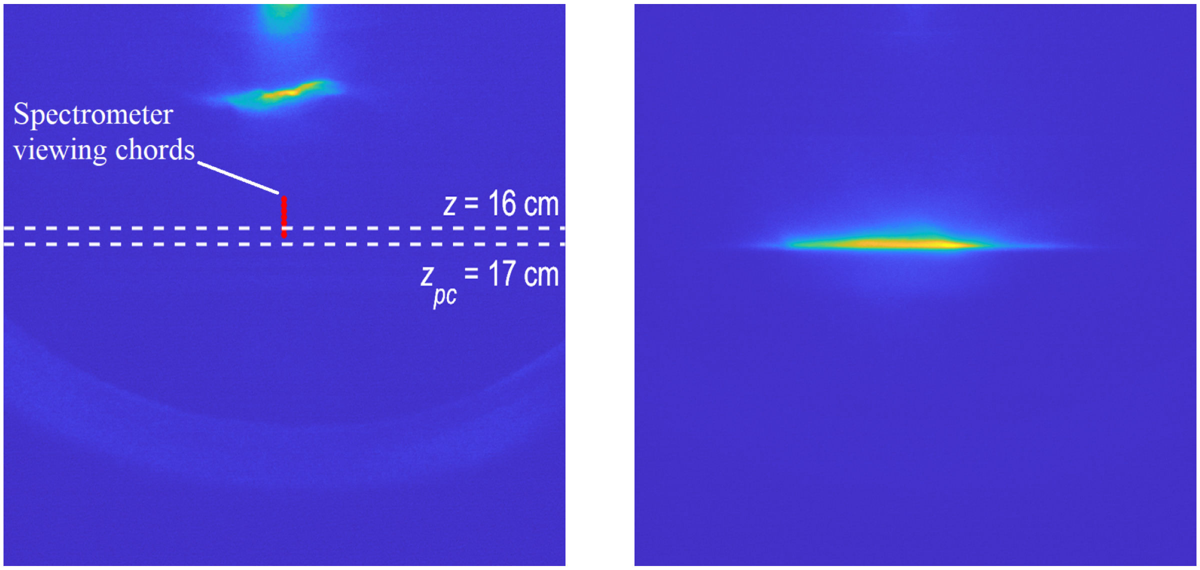

(a) $t - t_0$ = -13.22 µs (b) $t - t_0$ = -5.78 µs

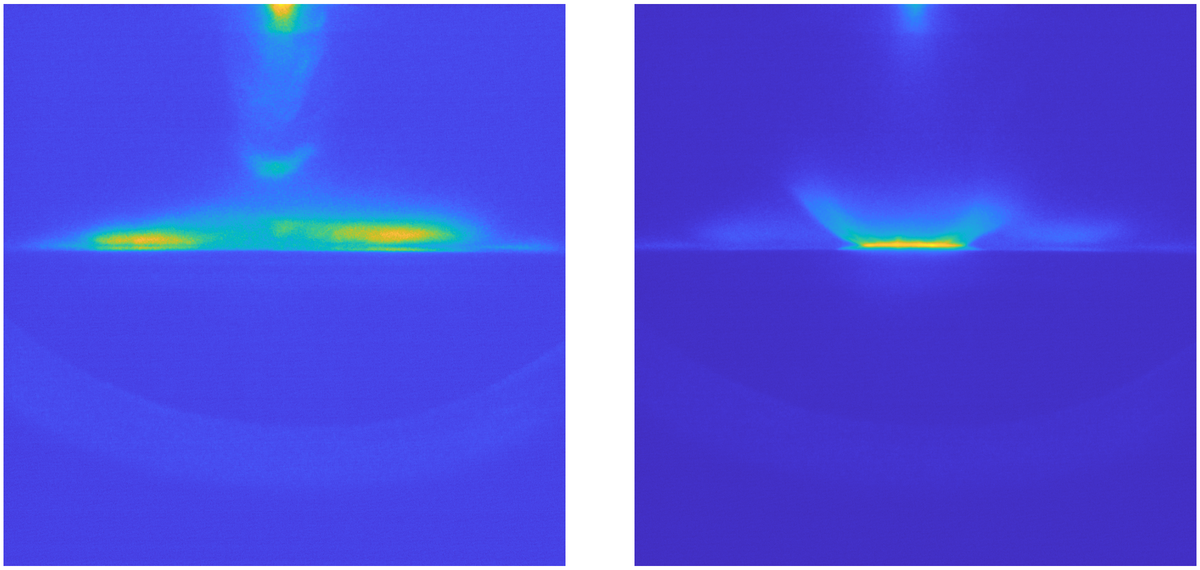

(c) $t - t_0$ = -1.63 µs (d) $t - t_0$ = 0.68 µs

Figure 3.3: Evolution of the experiment when the polycarbonate obstruction is located at $z_{\text{oc}} = 17$ cm. These images were taken and processed in the same manner as those reported in Figure 3.2.

3.3 Axial density profiles of collision events

Chord-integrated electron density is inferred at axial stations of $z_{pc} - z = 1$ cm and $z_{pc} - z = 2.5$ cm taken at the height of the jet propagation axis/bore-sight axis (y = 0) for both obstruction cases in Figures 3.4 and 3.5. The three stages of the experiment identified in the VUV images are also evident from these density profiles. As the first jet is en-route to the obstruction, each chord detects a local maximum in phase shift due to the jet passing through each interferometer beam. As the jet stagnates, there is a slow rise in n_{el} observed in the $z_{pc} - z = 1$ cm chord due to the background plasma expanding radially and back towards the muzzle of the gun. As this occurs, the second jet is detected at the $z_{pc} - z = 2.5$ cm station, as it travels unobstructed towards the background plasma. The second jets were shown in the camera images to be dimmer than the first jet, while the interferometer traces also suggest that the second jet is less dense as well, with a lower inferred n_{el}. This is likely because a sizeable portion of the neutral-gas-injection is accelerated as the first jet, leaving less material to make up the second jet. Averaged time-of-flight measurements taken in the lab frame for the second jet at the z = 9.5 cm and z = 14.5 cm interferometer chords suggest a bulk velocity of 32.9 km/s. After passing through the $z_{pc} - z = 2.5$ cm chord, there is a sharp increase at $z_{pc} - z = 1$ cm during time t_0, which corresponds to the bright, post-collision material observed in the camera images. This increase in chord-integrated electron density is suggestive of shock compression.

3.4 Transverse density distributions of collision events

To confirm that these collision events do form a shock, it is necessary to characterize the ion density enhancement that occurs as a result of the collision event [1, 13]. This means inferring

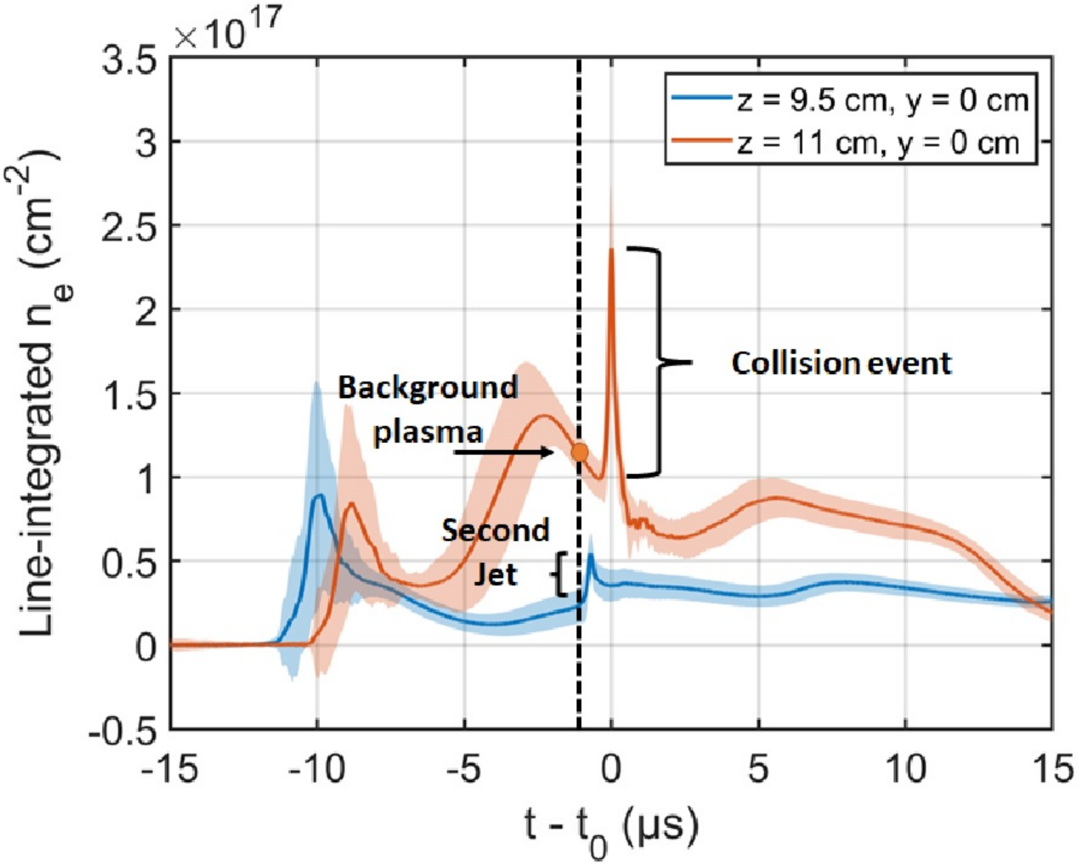

Figure 3.4: Temporal evolution of averaged line-integrated electron densities (solid lines) and 1σ standard deviations (gel-shaded), measured at two axial stations for the $z_{\mathrm{pc}} = 12$ cm case. Similar to the camera images, time is referenced to the transit time of the post-collision plasma which is concurrent with the local maxima in $n_e l$ at $z = 11$ cm, $y = 0$ cm. Line-integrated densities for the post-collision plasma and unobstructed jets are estimated as the peak value of $n_e l$ relative to the inferred density immediately preceding the transit time of the corresponding shot feature. The stagnated plasma density at $z_{\mathrm{pc}} - z = 1$ cm is inferred as the value of $n_e l$ measured at the time immediately preceding the arrival of the second unobstructed jet at $z_{\mathrm{pc}} - z = 2.5$ cm. This is done to ensure that the background plasma is inferred prior to any initial jet interaction further upstream of the location of the interferometer chords.

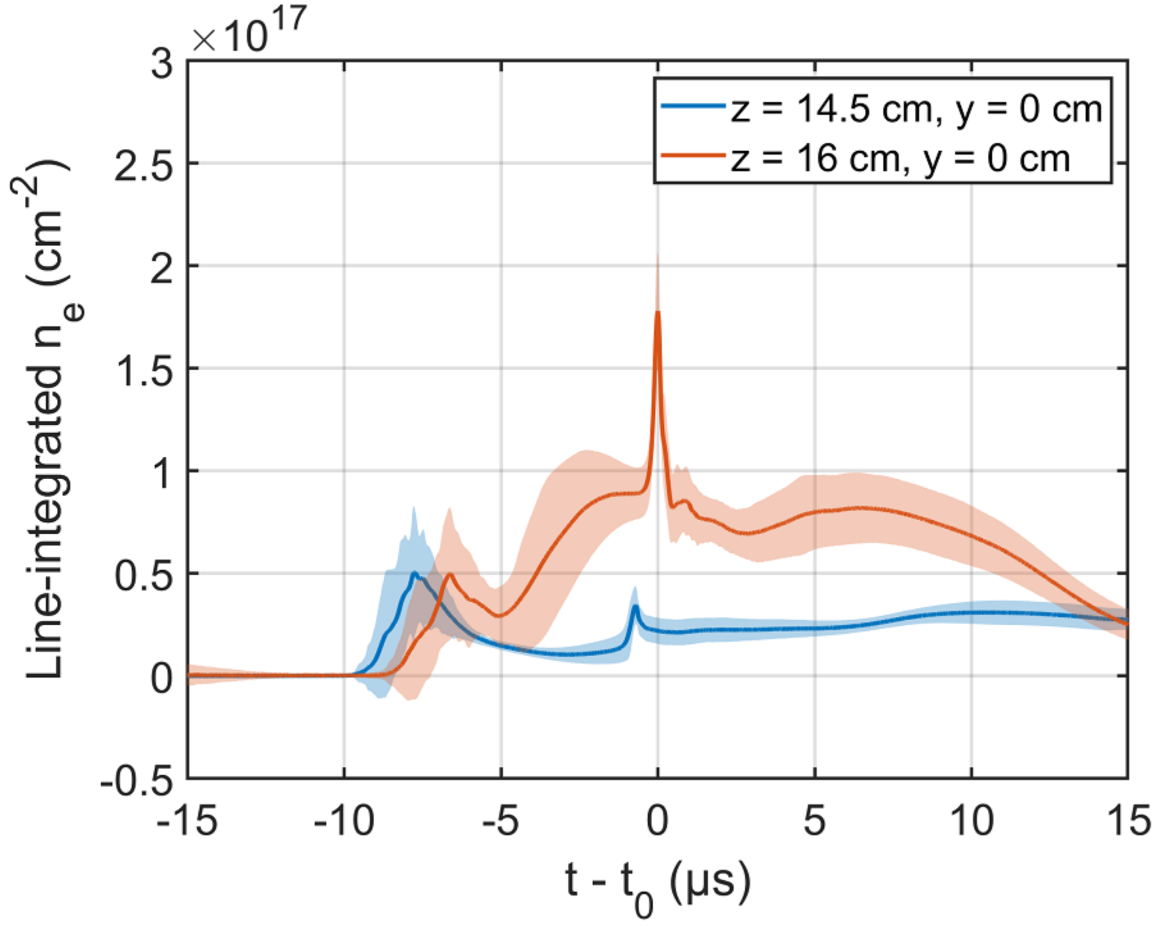

Figure 3.5: Temporal evolution of line-integrated densities at two different axial stations for the $z_{\text{pc}} = 17$ cm case.

volumetric electron density for the pre- and post- collision components, which can be used in coordination with PrismSPECT to obtain estimates of ion density [1, 13, 16]. To that end, chordal measurements across the radial profile of the plasma jets at the $z_{pc} - z = 1$ cm axial station are presented in Figures 3.6 and 3.7 for both obstruction cases. These chordal measurements are spaced 2 cm apart, probing the experiment at the height of jet propagation axis (y = 0 cm) up to 6 cm off-axis. Under the assumption of an axially symmetric plasma column [1, 10, 26, 27], these measurements show that densities are non-uniform, with n_{el} decreasing with increasing chordal height, y. The camera images, despite being taken along one line-of-sight, appear to validate these measurements, with the plasma emission strongest towards the center, and decreasing radially outward. The time-of-flight of the post-collision plasma increases with y-position. This is explained by the camera images which show that the post-collision plasma has a curved leading edge, therefore reaching off-axis locations later in time.

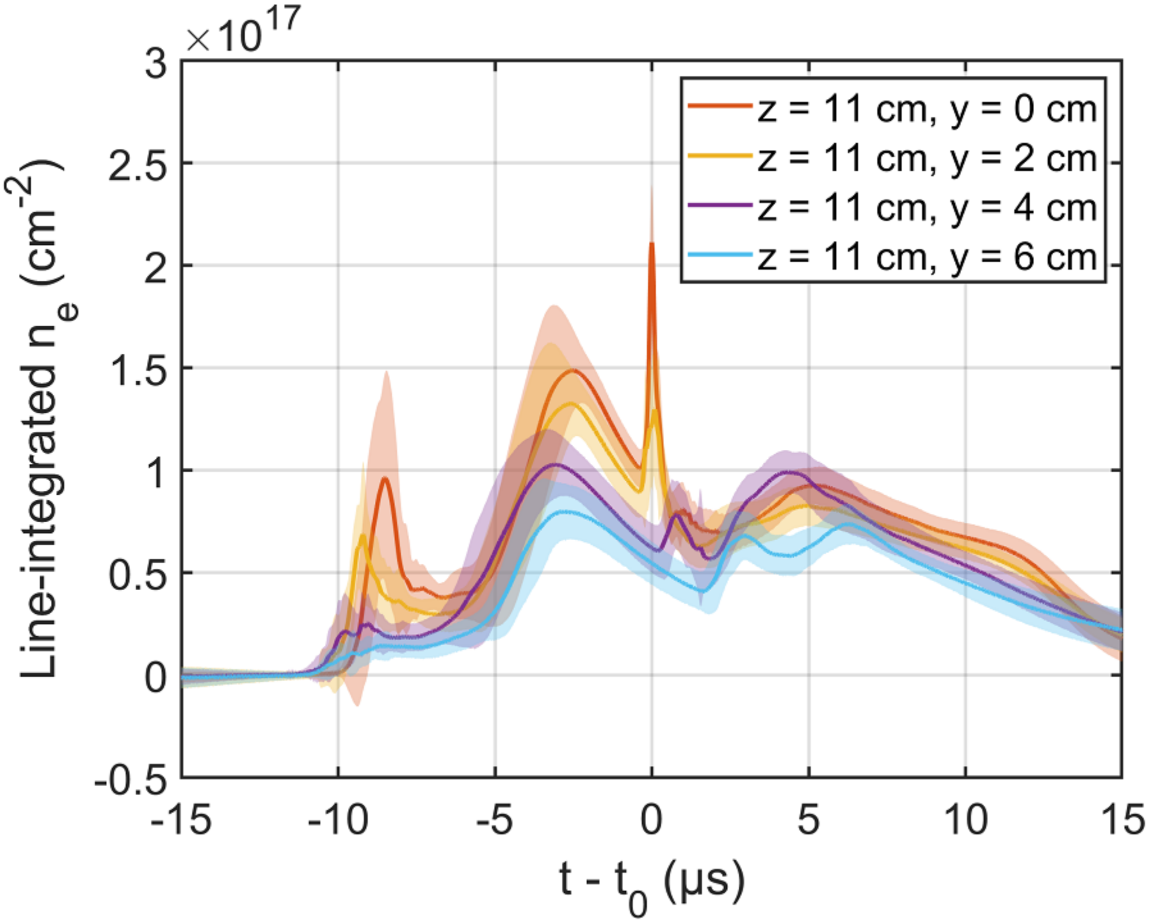

Figure 3.6: Temporal evolution of line-integrated densities at four different radial stations for the $z_{\mathrm{pc}} = 12$ cm case. A positive Y location indicates that the off-axis chord is located above the bore-sight axis.

To characterize the density of the unobstructed second jet, transverse density distributions for shots where no obstruction was placed in the chamber are present in Figures 3.8 and 3.9. While these measurements also show that n_{el} decreases with increasing y, the second jet is

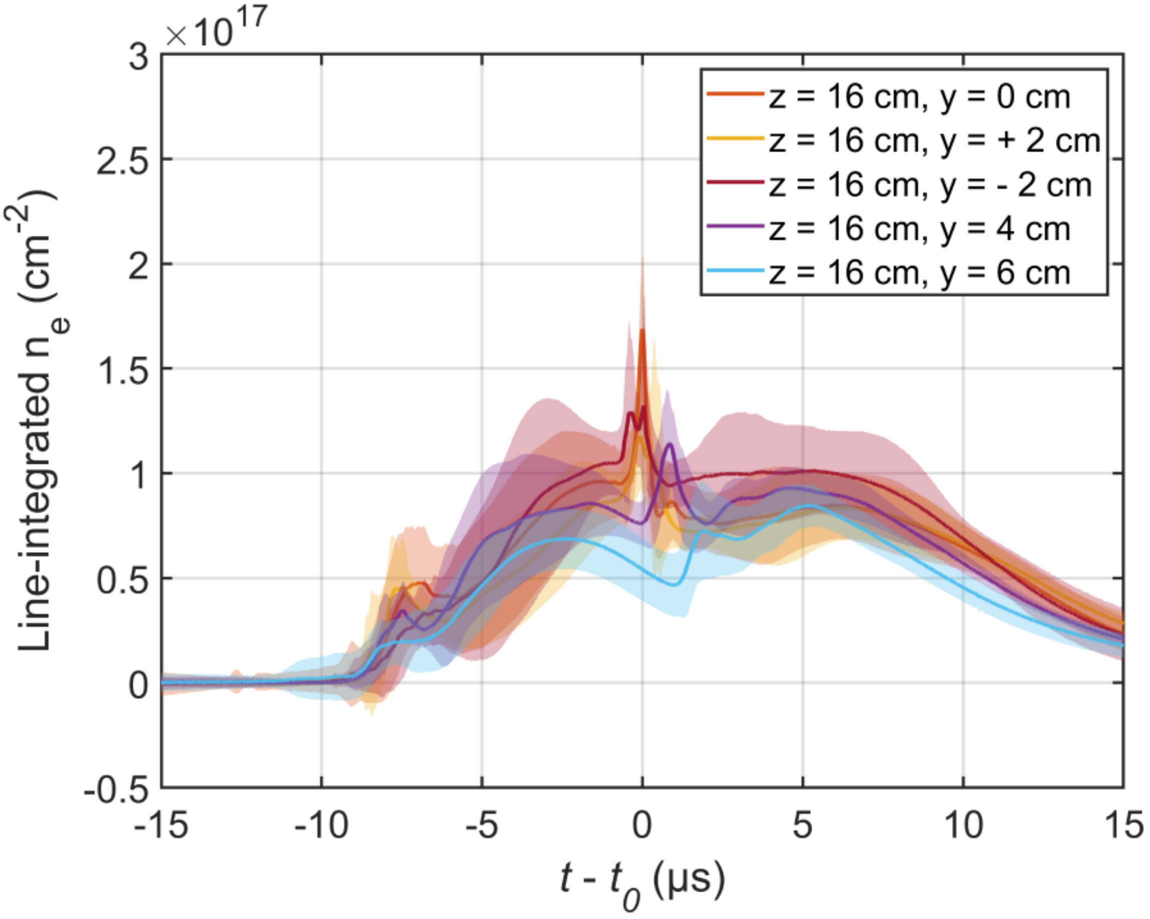

Figure 3.7: Temporal evolution of line-integrated densities at five different radial stations for the $z_{\mathrm{pc}} = 17$ cm case.

observed at the y = 0 and y = 2 cm radial locations at approximately the same time, which suggests that the jet leading edge is nearly planar.

3.5 Abel-inverted estimates of volumetric electron density

Of these temporally resolved measurements, there are three distinct shot features in each obstruction case that are of interest to us. These include the local maxima associated with

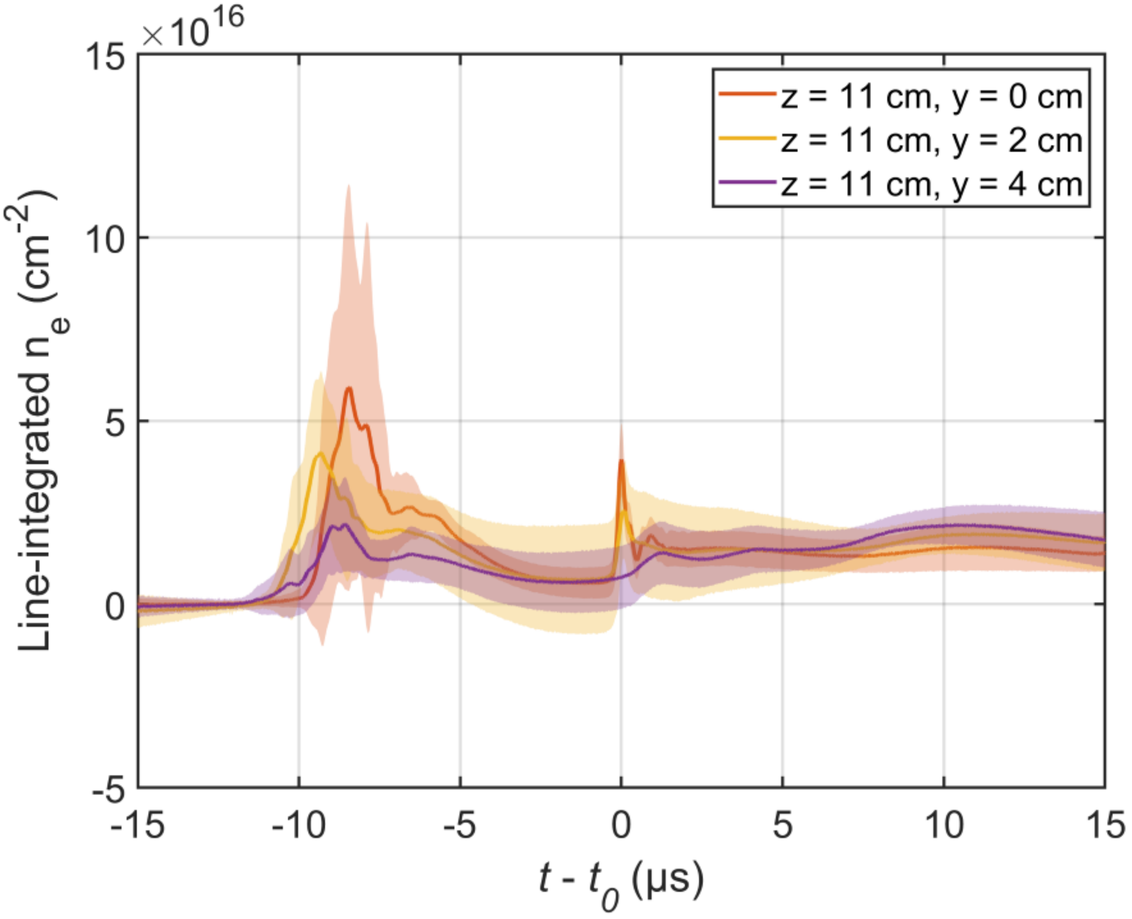

Figure 3.8: Temporal evolution of line-integrated densities at three different radial stations, characterizing the unobstructed jets as they pass freely through the z = 11 cm axial station.

the post-collision plasma in the $z_{pc} - z = 1$ cm chord, the local maxima of the unobstructed second jet, as measured in the chord closest to the obstruction for each case (z = 11 cm for z_{pc} = 12 cm and z = 14.5 cm for z_{pc} = 17 cm), and the background plasma measured in the $z_{pc} - z = 1$ cm chord immediately preceding any interaction with the second jet. On and off-axis phase shift measurements for each of these features are used as input to the matrix Abel inversion process detailed in Chapter 2 [26, 27] to obtain radial electron density profiles for each of these plasma structures, as shown in Figures 3.10 and 3.11. Because the spatial resolution from these measurements depends on the chord-to-chord spacing along the

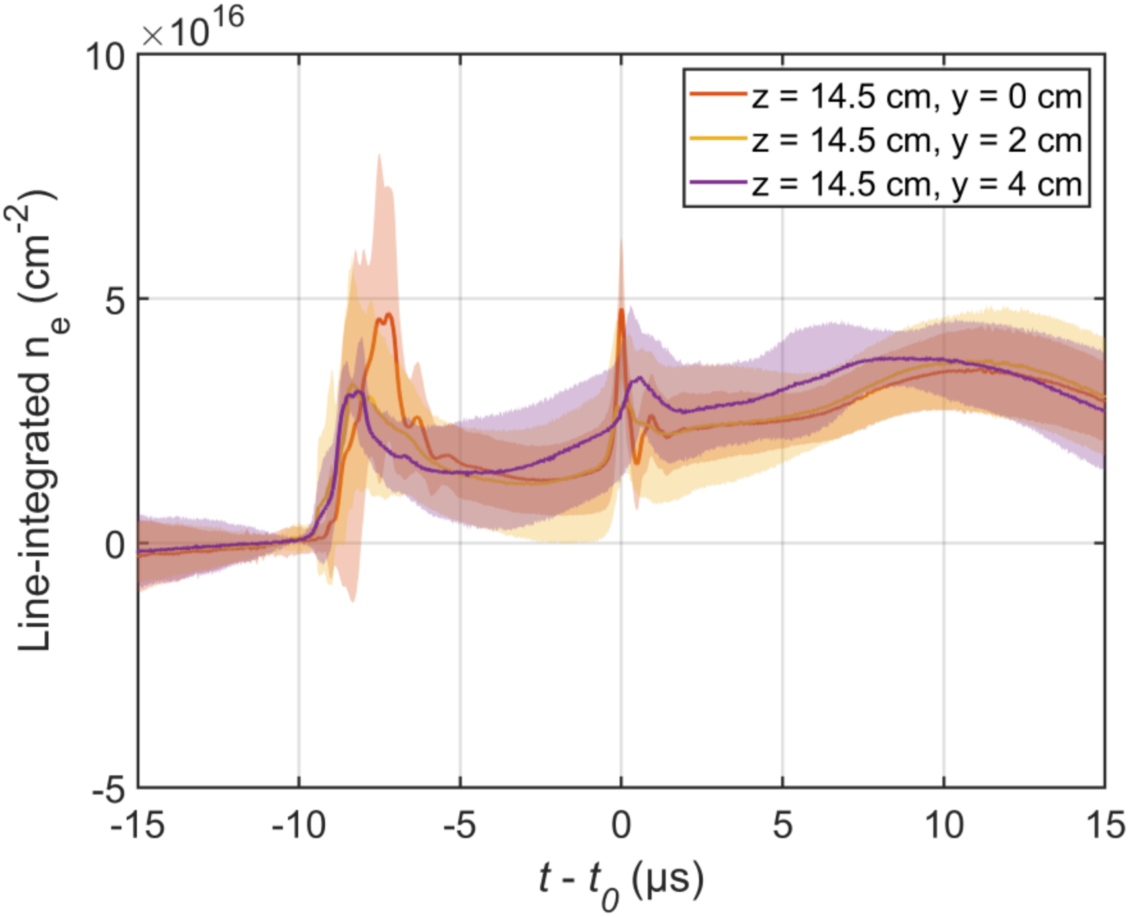

Figure 3.9: Temporal evolution of line-integrated densities at three different radial stations, characterizing the unobstructed jets as they pass freely through the z = 14.5 cm axial station.

y-axis [1, 10, 26, 27], we assume that the inverted density profiles are constant over shells roughly 2 cm in radius. To recover the background plasma radial density distribution, we assume that n_e –> 0 cm as y –> 18 cm. This boundary condition is physically enforced by the use of an optical breadboard which supports the obstruction in the chamber, and is located roughly 18 cm below the bore-sight axis.

For all plasma structures, density decreases with increasing radial position. Across both obstruction cases, the density of the post-collision plasma and unobstructed second jet is approximately zero at the r = 4 cm station, suggesting that these features have a total width on the order of 8 cm, despite being radially unconstrained in experiment. On-axis densities for all components are presented in Tables 3.2 and 3.3 for the two obstruction cases, alongside one-sigma standard deviations, which were propagated from variances [51] in phase shift measurements throughout the inversion process. Both tables show that the on-axis density of the post-collision plasma is roughly an order of magnitude greater than the on-axis density of the pre-collision components.

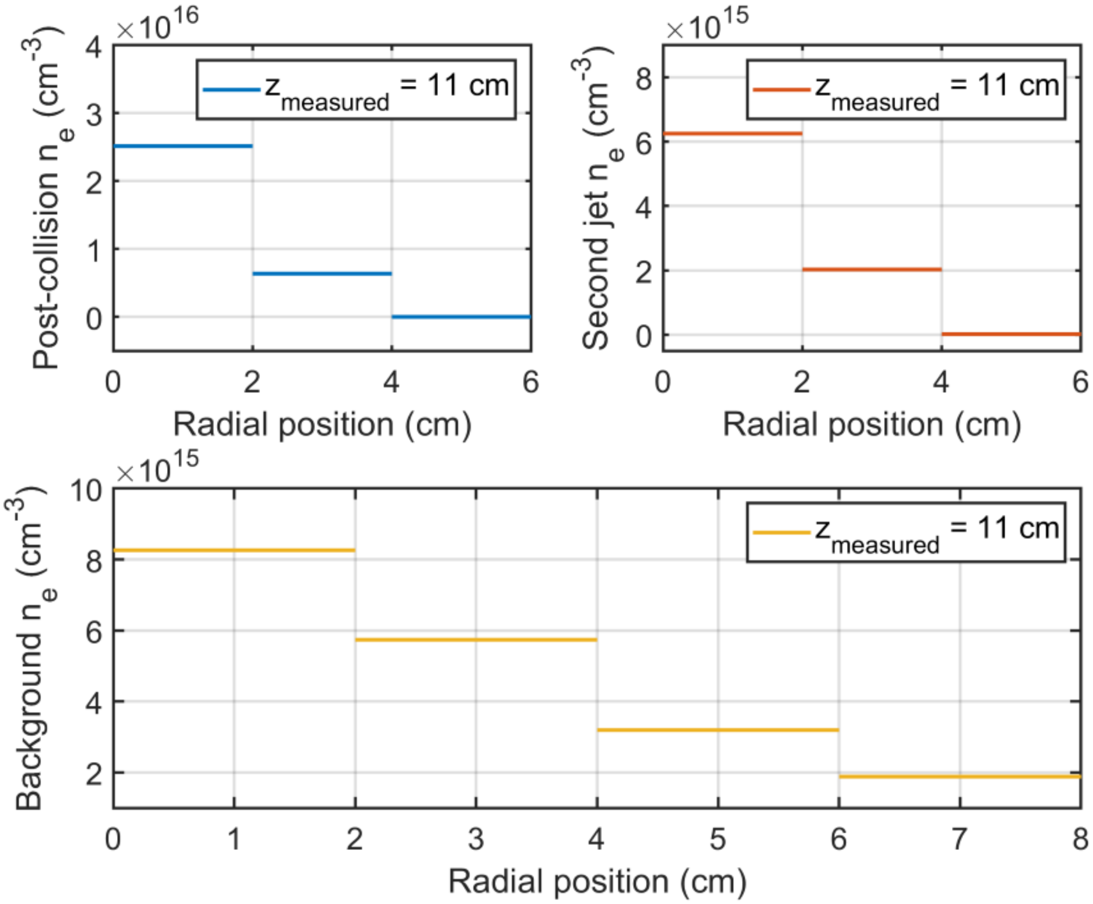

Figure 3.10: Electron densities inferred from Abel-inverted interferometer measurements made for the $z_{\mathrm{pc}} = 12$ cm case.

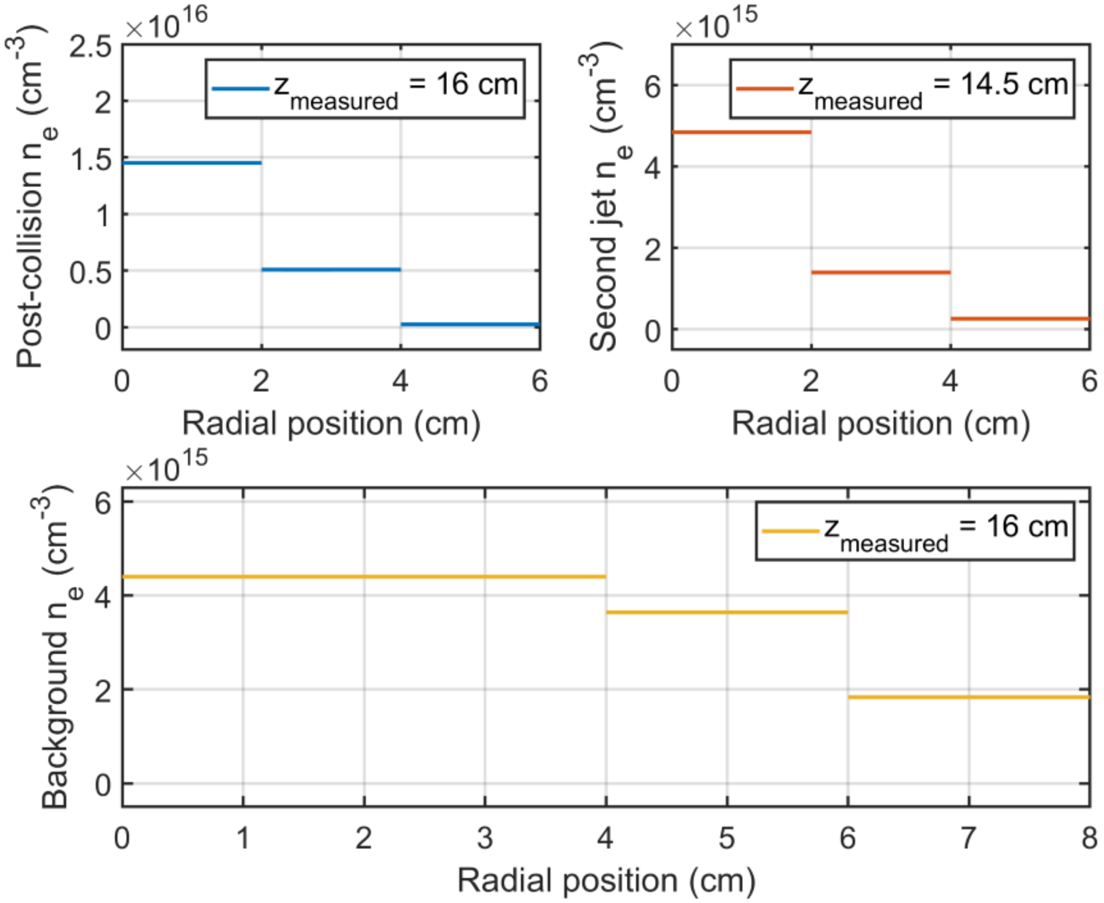

Figure 3.11: Electron densities inferred from Abel-inverted interferometer measurements made for the $z_{\text{pc}} = 17$ cm case.

Table 3.2: Averaged on-axis electron densities and one-sigma standard deviations for the $z_{\text{pc}} = 12$ cm case.

	z (cm)	n_e (cm^{-3})
background	11	$8.3 \pm 2.1 \times 10^{15}$
second jet	11	$6.3 \pm 2.0 \times 10^{15}$
post-collision	11	$2.5 \pm 1.0 \times 10^{16}$

Table 3.3: Averaged on-axis electron densities and one-sigma standard deviations for the $z_{\mathrm{pc}} = 17$ cm case.

	z (cm)	n_e (cm^{-3})
background	16	$4.4 \pm 1.2 \times 10^{15}$
second jet	14.5	$4.8 \pm 1.9 \times 10^{15}$
post-collision	16	$1.5 \pm 0.6 \times 10^{16}$

3.6 Inference of temperature and charge state using PrismSPECT

As a final step towards estimating the ion density enhancement as a result of each collision event, the Abel-inverted interferometer measurements are used in coordination with spectrometer measurements at the same axial location to infer plasma temperature, charge state and ion density using PrismSPECT and the iterative analysis technique described in Chapter 2 [1, 12, 13, 15, 16, 18, 19]. The converged plasma parameters, as displayed in Tables 3.4 and 3.5 show that for both obstruction cases, there is not a significant rise in electron temperature as a result of the collision event. All pre- and post-collision components have an electron temperature within the 2 to 3 eV range. Consequently, the mean charge state across all components are within 1 to 2. This suggests that during the collision event, ionization is not the dominant mechanism that accounts for the density gradient observed from phase shift measurements. Rather than ionizing atoms in the plasma, the results suggest that the second jet instead acts like a piston, compressing material back towards the obstruction, resulting in an increase in ion density, and consequently electron density. This hypothesis is reinforced by estimates of ion density enhancement provided for both obstruction cases in Table 3.6. We estimate density enhancement as the ion density of the post-collision plasma divided by the sum of the second jet and background plasma ion densities, which is a variation of the metric employed by Merrit et al. in their studies of obliquely merging supersonic plasma jets [1, 13, 16]. If this value is less than 1, then the density enhancement during the collision event is primarily due to jet interpenetration of the second jet through the background plasma [1, 13, 16]. However, a density enhancement greater than 1 suggests that jet interpenetration alone cannot account for the density increase, and that the density increase must be due to compression of material upon impact [1, 13, 16]. For both obstruction cases, the density enhancement is greater than 1, suggesting that this is indeed the case. Furthermore, a density increase greater than 1 is strongly indicative of collisional shock formation when one considers that the plasma jets are radially unconstrained. As in other laboratory studies of plasma shocks [1, 13, 16], three-dimensional effects such as pressure-relief out of the page is also occurring upon impact, the fact that any density enhancement greater than 1 is observed is a strong indicator of collisional shock formation, suggesting that for both obstruction cases, the post-collision plasma is in fact post-shocked material.

Table 3.4: Plasma parameters inferred from the iterative PrismSPECT analysis [1, 12, 13, 15, 16, 18, 19] of the $z_{\mathrm{pc}} = 12$ cm spectrometer data, assuming a plasma jet composition of 86% argon.

	z	T (eV)	$\bar{Z}$	n_i (cm^{-3})
background	11	$T > 2.4$	$\bar{Z} > 1.7$	$n_i > 5.0 \times 10^{15}$
second jet (pre-collision)	11	2.0 - 2.8	1.1 - 1.9	3.3×10^{15} - 5.6×10^{15}
post-collision	11	2.4 - 2.6	1.7 - 1.8	1.4×10^{16} - 1.5×10^{16}

Table 3.5: Plasma parameters inferred from the iterative PrismSPECT analysis [1, 12, 13, 15, 16, 18, 19] of the $z_{\mathrm{pc}} = 17$ cm spectrometer data, assuming a plasma jet composition of 86% argon.

	z	$T\,(\mathrm{eV})$	$\bar{Z}$	$n_i\,(\mathrm{cm}^{-3})$
background	16	2.4 - 2.8	1.6 - 1.9	2.3×10^{15} - 2.8×10^{15}
second jet (pre-collision)	16	2.0 - 2.8	1.1 - 1.9	2.2×10^{15} - 3.8×10^{15}
post-collision	16	2.4 - 2.6	1.7 - 1.8	7.9×10^{15} - 8.8×10^{15}

Table 3.6: Ion density enhancement induced from plasma-jet collision; inferred from plasma parameters presented in Table 3.4 and 3.5

$z_{\mathrm{pc}}\,(\mathrm{cm})$	12	17
$z_{\mathrm{measured}}\,(\mathrm{cm})$	11	16
$n_{\mathrm{collision}}/(n_{\mathrm{background}} + n_{\mathrm{jet2}})$	1.3 - 1.8	1.2 - 2.0

3.7 Inference of axial density gradients from stark broadening

We now turn to our spatially resolved spectrometer diagnostic to study the structure of the post-shocked material in these experiments. Measurements of the Stark width (see Chapter 2) of the Ar-II line at 488 nm during shots where the post-shock material is present in the fiber viewing chords allow for inferences of axial density profiles across the post-shock material. These inferences in density are obtained across pairs of fibers, thus electron density is assumed in viewing chords of ≈ 6 mm in length. Axial density profiles are presented for both obstruction cases in Figures 3.12a and 3.12b. Both the FFT [20] and λ-space fitting routines were employed, with gel-shaded standard deviations provided, which is inferred from confidence intervals from the fitting routines propagated [51] alongside experimental uncertainties to yield uncertainties in electron density. For viewing chords locations that were coincident with interferometer chord measurements, we provide Abel-inverted electron density estimates at r = 0 to aid in interpretation of the fitting routine. While our spectrometer measurements by nature are integrated along the optical line-of-sight [26], we interpret the broadening associated with our recorded line profile to correspond to the greatest density occurring along the optical line of sight, which is typically at the r = 0 cm location.

In the $z_{pc} = 17$ cm case, we note that the Abel-inverted density estimate is less than, but on the order of the Stark-inferred n_e at the same location. This is because spectrometer measurements are more localized, and density is estimated over viewing chords that are millimeters in length, rather than being averaged over centimeter sized shells, as is the case with interferometer measurements. For this obstruction case, the FFT and λ fitting routines return nearly equivalent estimates of density. This agreement is also observed to a degree in the $z_{pc} = 12$ cm density profiles in Figure 3.12a, where the FFT and λ fits are nearly equivalent in the viewing chord closest to the obstruction. However, this agreement breaks down in adjacent viewing chord, positioned farther away from the obstruction, where the λ fit infers a density significantly less than that of the FFT fit. This discrepancy is likely attributed to the low signal-to-noise-ratio associated with the spectrogram recorded during this shot, resulting in a high fitting residual for both routines. That being said, the corresponding FFT fit is on the order of the interferometer measurement obtained at the same z-axis location. These inferences suggest a significant increase in electron density, with line broadening along the viewing chord closest to the obstruction suggesting electron densities an order of magnitude greater than those inferred at $z = 11$ cm. This axial density gradient is consistent with collisional shock formation and suggests additional density enhancement beyond the $z_{pc} - z = 1$ cm station.

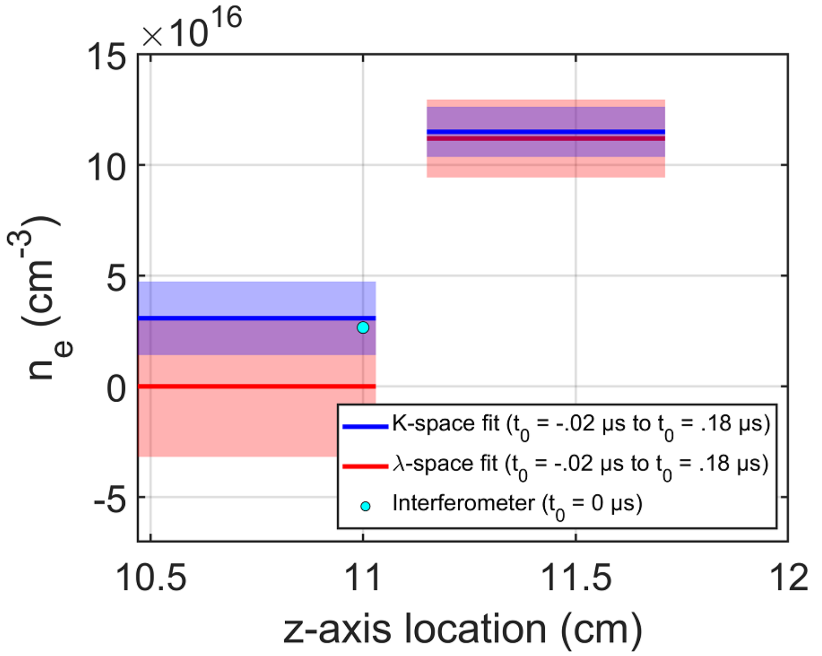

(a) Inferred axial electron density distribution for shot 1800, representing the $z_{pc} = 12$ cm case.

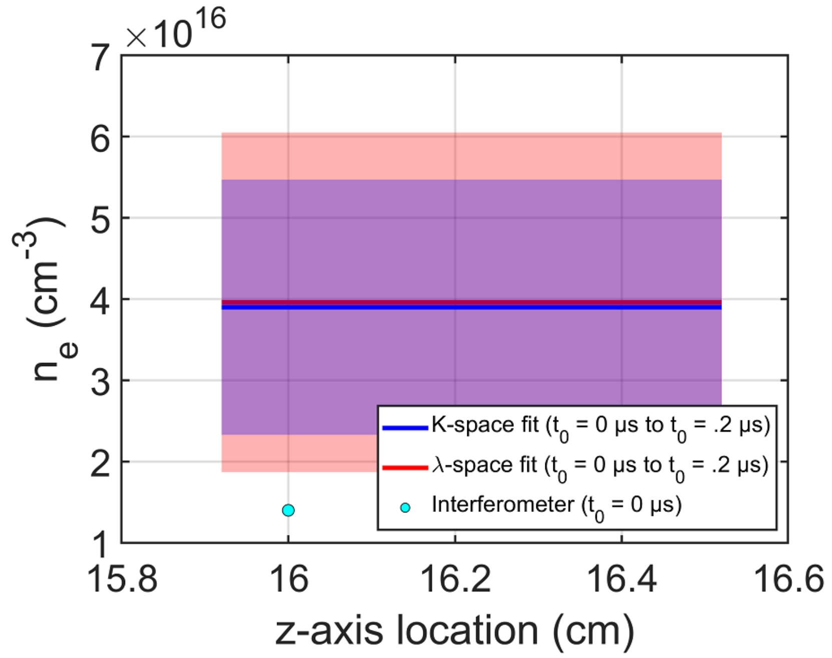

(b) Inferred axial electron density distribution for shot 1612, representing the $z_{pc} = 17$ cm case.

Figure 3.12: Stark inferred electron densities and 1-sigma standard deviations (gel-shaded) alongside Abel-inverted interferometer measurements. Electron densities inferred from both the traditional λ fit and k-space fit are both presented to compare fitting routines.

3.8 Collision and diffusion parameters relevant to the study of plasma shocks

Experimental results from this campaign are now compared to analytical models to better understand the collision event, and address the suitability of this experimental setup towards resolving shock front separation in multi-ion-species plasmas [7]. We first turn to kinetic models associated with jet interpenetration and intra-jet mean free paths [1, 13, 17, 19, 23, 24, 25]. Considering a test ion with plasma parameters associated with the unobstructed second jet, the ion-ion interpenetration length estimates the distance that this test ion will stream through a Maxwellian field particle distribution of the stagnant background plasma before becoming collisional [1, 13, 17, 19, 23, 24, 25]. This interpenetration length is calculated according to Equation 3.1 below [1, 13, 17, 19, 23, 24, 25], where λ_{ii} is the Coulomb logarithm for counter-streaming ions [1, 13, 17, 19, 23, 24, 25]. Additionally, the intra-jet mean free path is calculated considering a test ion from the post-shock material as it collides with a Maxwellian distribution of field particles from the post-shock material at the ion thermal speed [23, 25]. For both cases, we consider test particles of argon and impurity carbon atoms within our plasma. The field particles is taken as a molar-fraction weighted average over all species present in the plasma. All estimated collision lengths, presented in Tables 3.7 and 3.8 are less than or on the order of the centimeter scale shock structure, suggesting that across both obstruction cases, the second jet-stagnant plasma interaction exists in a semi- to fully collisional regime. When considering the interpenetration lengths, these results reinforce the picture that the second jet acts as a piston upon impact.

$$\lambda_i^s \approx \frac{u_{rel}}{4\nu_s^{i|i'}}. \tag{3.1}$$

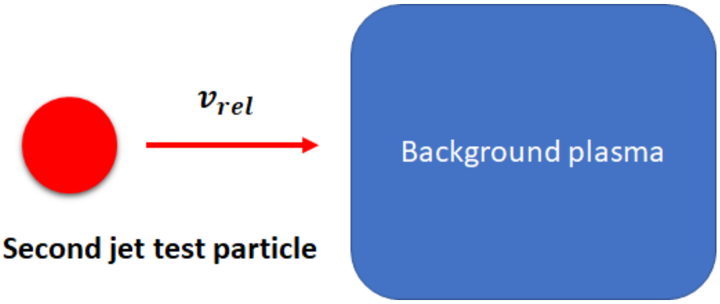

Figure 3.13: Interpenetration lengths model how far the second jet ions streams through the background plasma before becoming collisional [1, 13, 17, 19, 23, 24, 25].

Table 3.7: Ion-ion interpenetration lengths, calculated using plasma parameters inferred from iterative PrismSPECT analysis [1, 12, 13, 15, 16, 18, 19].

z_{pc} (cm)	12	17
$\lambda^s_{i,\mathrm{Ar}}$ (mm)	2.1 – 5.9	3.3 – 11
$\lambda^s_{i,\mathrm{C}}$ (mm)	.3 – .9	.6 – 1.7

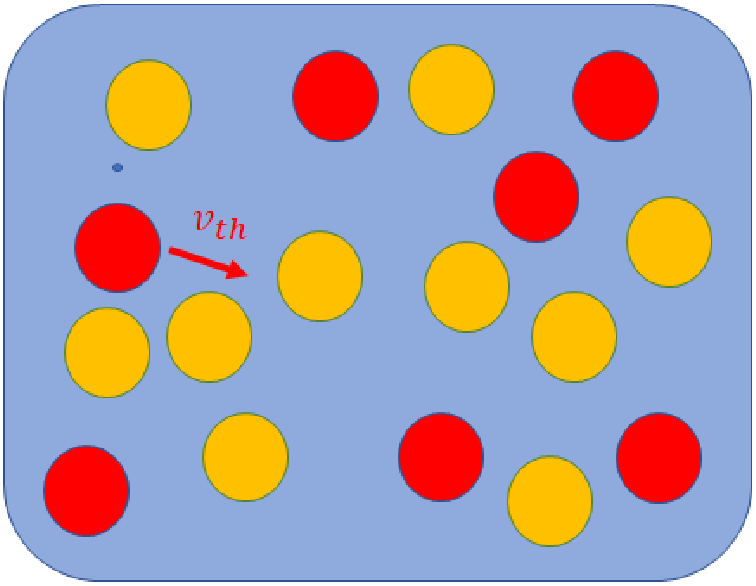

Figure 3.14: Mean free path model considers a test particle colliding with ion species in the post-shock region [23, 25].

We now use fluid theory [7, 23, 30, 32, 42] to characterize the post-shock material in the context of species separation. As mentioned in Chapter 1, the theoretical basis for species separation in fluids and plasmas is well-established [7, 23, 30, 32, 42], with the diffusive

Table 3.8: Post-shock intra ion-ion mean free paths, calculated using plasma parameters inferred from iterative PrismSPECT analysis [1, 12, 13, 15, 16, 18, 19].

z_{pc} (cm)	12	17
$\lambda_{i,\mathrm{Ar}}$ μm	7 – 8	11 - 13
$\lambda_{i,\mathrm{C}}$ μm	6 – 7	10 – 11

mass flux of the light ion species in the center-of-mass frame of a binary ion fluid element given by equation 1.1. Gradients in the log of total ion pressure, electron temperature and ion temperatures, constitute baro- and thermodiffusion, with the ambipolar electric field driving electrodiffusion [7, 23, 30, 32, 42]. Analytic forms for the electro and baro diffusion coefficients are available with literature, wihle the thermodiffusion coefficients require a collisional model to estimate [23, 30, 31, 32]. In Table 3.9, we estimate the strength of the various diffusion mechanisms present in the post-shock material, where the various gradients are computed using experimentally derived parameters associated with the pre-collision second jet and post-shocked material. The ambipolar electric field assumed proportional to the gradient in electron temperature [23, 32, 45, 52]. The ratio of baro- and electro-diffusion coefficients show that for both obstruction cases, electro-diffusion reinforces baro-diffusion. The ratio of the total baro- and electrodiffusion terms (diffusion coefficients times the corresponding gradients) suggests that barodiffusion dominates over electrodiffusion. In the absence of a kinetic model, the ratios of the relevant barodiffusion and thermodiffusion gradients suggests that barodiffusion also dominates over thermodiffusion. These results suggest that for the shocks identified within these experiments, barodiffusion will be the dominant driver of diffusive mass flux at the shock front, which is consistent with other experimental studies performed on shocks within a similar parameter space [23, 32].

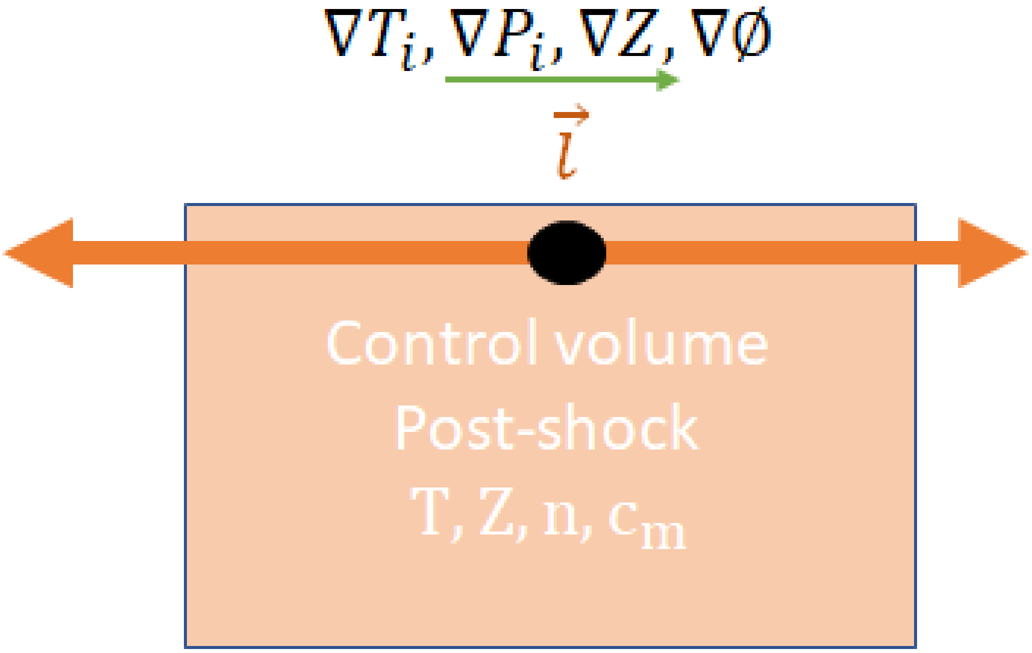

Figure 3.15: Control volume model used for diffusion analysis.

Table 3.9: Relative strengths of diffusion mechanisms, calculated using the formulism presented in Equation 1.1 [23, 30, 31, 32].

z_{pc} (cm)	12	17
k_{Pi}/k_E	0.62 – 0.64	0.62 - 0.64
$\bar{f}_{1_{\text{Baro}}}/\bar{f}_{1_{\text{Electro}}}$	3.1 – 4.6	2.7 – 4.0
$\nabla log(P_i)/\nabla log(T_i)$	4.4 – 6.5	3.8 – 5.6

3.9 Conclusion

The experimental campaign described in this chapter has characterized the interaction between supersonic jets with stagnated plasma, utilizing experimental configurations where obstructions were placed at $z_{pc} = 12$ cm and $z_{pc} = 17$ cm. For both obstruction cases, the collision event is concurrent with a sharp increase in ion and electron density, which is suggestive of collisional shock formation. Kinetic models [1, 13, 17, 19, 23, 24, 25] and spatially resolved measurements suggest that the interaction event is semi- to fully-collisional, producing post-shock material with highly collisional ions and axial density distributions consistent with collisional shock formation. Fluid theory [7, 23, 30, 32, 42] suggests that within the plasma regime present in this campaign, barodiffusion will serve as the dominant driver of diffusive mass flux at the shock front. This campaign provides the foundation for the work presented in Chapter 4, and has also shown that the experimental and diagnostic setup detailed in Chapter 2 is viable for studying plasma shocks on spatial scales not previously attempted in the published literature.

Chapter 4

Species separation in a plasma shock with more than two ion species

4.1 Experimental setup

With the collision between predominantly argon jets studied in the previous chapter, we now introduce additional ion species into our experiment by doping the gas supplied to the railgun with nitrogen. Prior to ionization, the gas supplied to the railgun is roughly 90 % Ar, 10 % N_2 by molar fraction, resulting in the formation and acceleration of multi-ion-species plasma jets. As we will cover in the successive sections, the impurity lines in the post-shocked material are noticeably brighter, with very strong aluminum lines consistently being observed within the experiment. Thus, the measurements presented in this study correspond to collisional plasma shocks with at least three ion species present. We utilize this adjustment to the experiment to assess the proscpect of gradient-driven species separation in multi-ion-species collisional plasma shocks. We use the experimental setup from the previous experimental campaign [15] as the foundation for this most recent study. Because the $z_{pc} =$ 12 cm study yielded denser and brighter plasma jets [15], this study focuses exclusively on this obstruction position. The obstruction placement and chamber orientation remain the same as before. The biggest difference comes from the diagnostics, which are re-positioned to probe the shock at distances closer to the obstruction. This is in the form of fixed interferometer chords at z = 11 cm (z - z_{pc} = 1 cm) and z = 11.65 cm (z - z_{pc} = .35 cm). The telescope for the spectrometer was slightly altered to obtain a finer fiber-to-fiber spatial resolution of ≈1.7 cm, that subtends the interferometer chord arrangement, with the closest fiber probing a distance ≈ 2 mm away from the obstruction. The viewing locations for each chord are provided in Table 4.2. This telescope location is close enough to the obstruction to observe any separation that occurs, but also far away from the obstruction to ensure that viewing chords are not being obstructed or blocked in any way. Additional calculations in the proceeding sections will also show that the plasma probed at these regions are free from any sheath effects, allowing us to assume quasi-neutrality in our analysis [10, 33]. Additionally, the telescope was affixed atop a translation stage (See Figure 4.1) that allowed us to probe the plasma at two stations: One where the fibers are aligned axially alongside the bore-sight-axis, and a second station translated ≈1.6 cm in the direction transverse to the propagation of the jets (in the downwards direction of Figure 4.1). Because the telescope must be translated to each radial station, it is impossible to simultaneously obtain axial and radial information in a single shot. However, proceeding sections will analyze averaged shot statistics at each station to make inferences about the radial intensity profiles of each species, which are crucial to the interpretation of our results.

Table 4.1: Viewing chord information relevant to the spectrometer diagnostic for the experiments performed in this chapter. Throughout this experimental campaign, a spatial resolution of ≈ 1.73 mm is maintained with the viewing chord arranged closer to the obstruction than in the last chapter.

Experimental config. (cm)	Fiber number	Central viewing chord (cm)	Nearest interferometer chord (cm)
	F1	11.72	z = 11.65
	F2	11.55	–
	F3	11.37	–
$z_{\mathrm{pc}} = 12$	F4	11.20	–
(imaging collision event)	F5	11.03	z = 11

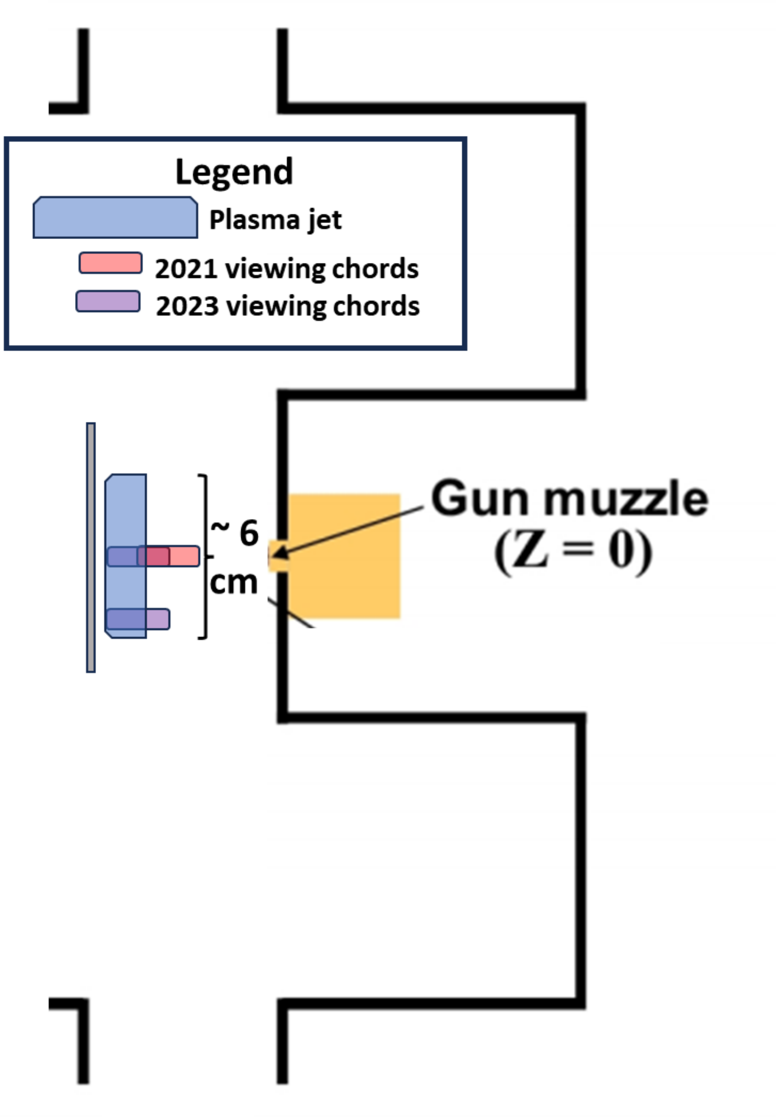

Figure 4.1: Comparison of spectrometer viewing chords between campaigns. In this most recent study, the viewing chords are located at axial locations closer to the obstruction location. Additionally, the telescope is varied between two different radial stations, effectively providing chord integrated measurements across the width of the post-shock material. This more detailed setup is leveraged in subsequent sections to quantify the distribution of ion species across the shock.

4.2 Qualitative insights into shock formation and propagation

Just as before, Chord-integrated interferometer traces of the experiment alongside temporally-resolved, VUV image of the collision event are presented in Figures 4.2 and 4.3. The chronological progression of the collision event is consistent with the previous experimental campaign [15], where the obstruction stagnates the first jet, which the second jet collides with moments later. This results in the usual features also being observed in our interferometer chords. However, one point of interest is that features attributable to the post-shocked material is only observed at the z = 11.65 cm chord. At z = 11 cm the expected large jump in *nel* is significantly smaller, with an observed *nel* that is more consistent with that of the unobstructed second jet, as measured in previous experiments. This suggests that the plasma shock has not formed by the time it reaches the z = 11 cm station. At this time, the interaction between the second jet and stagnated first jet is likely dominated by kinetic interpenetration, with the transition to a collisional regime happening later in time, as evidence by the large density gradient observed at the z = 11.65 cm station. Prior to beginning this campaign, the railgun and PFN system was refurbished. As a result, this change in the location at which the post-shocked material is observed cannot be attributed solely to the gas mixture supplied to the railgun. It is likely that subtle differences in the re-construction of the railgun and capacitor bank system contributed as well. However, the identification of collisional shock formation at the z = 11.65 cm station shows that the arrangement of our spectrometer viewing chords from Table 4.2 are sufficient for studying the shock front and post-shock region.

One potential consequence of probing regions closer to the obstruction location is the risk of probing a region prone to plasma sheath effects [10, 33]. If this is true, we cannot assume

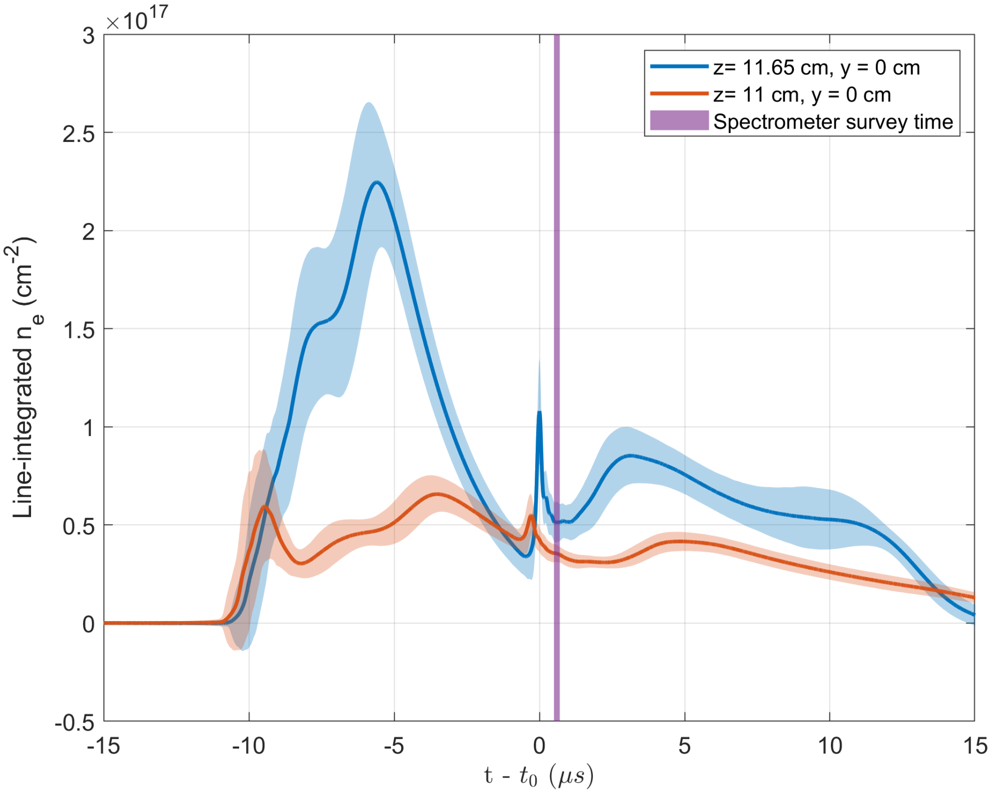

Figure 4.2: Averaged line-integrated n_e and 1-sigma standard deviation for the interferometer arrangement described in Section 4.1. Jet-interpenetration is observed in the z = 11 cm chord, which then transitions to collisional shock formation at z = 11.65 cm at $t - t_0 = 0$ µs. The vertical gel-shaded line represents the spectrometer survey time extensively studied in proceeding sections.

quasi-neutrality in our analysis [10, 33]. To further investigate this, we assume order of magnitude estimates of n_e, T_e, and $\bar{Z}$ (See Section 4.4) to estimate the plasma Debye length in the spectrometer viewing chord closest to the obstruction [33]. Assuming these parameters are an order-of-magnitude estimate for the plasma right in front of the obstruction, the sheath thickness can be approximated as being within ten Debye lengths [10, 53]. Even ten times the Debye length is still orders of magnitudes less than a millimeter, suggesting the region probed by the spectrometer is free of any sheath effects.

A second test for quasi-neutrality relies on an argument made by Bellei et al. [7], which

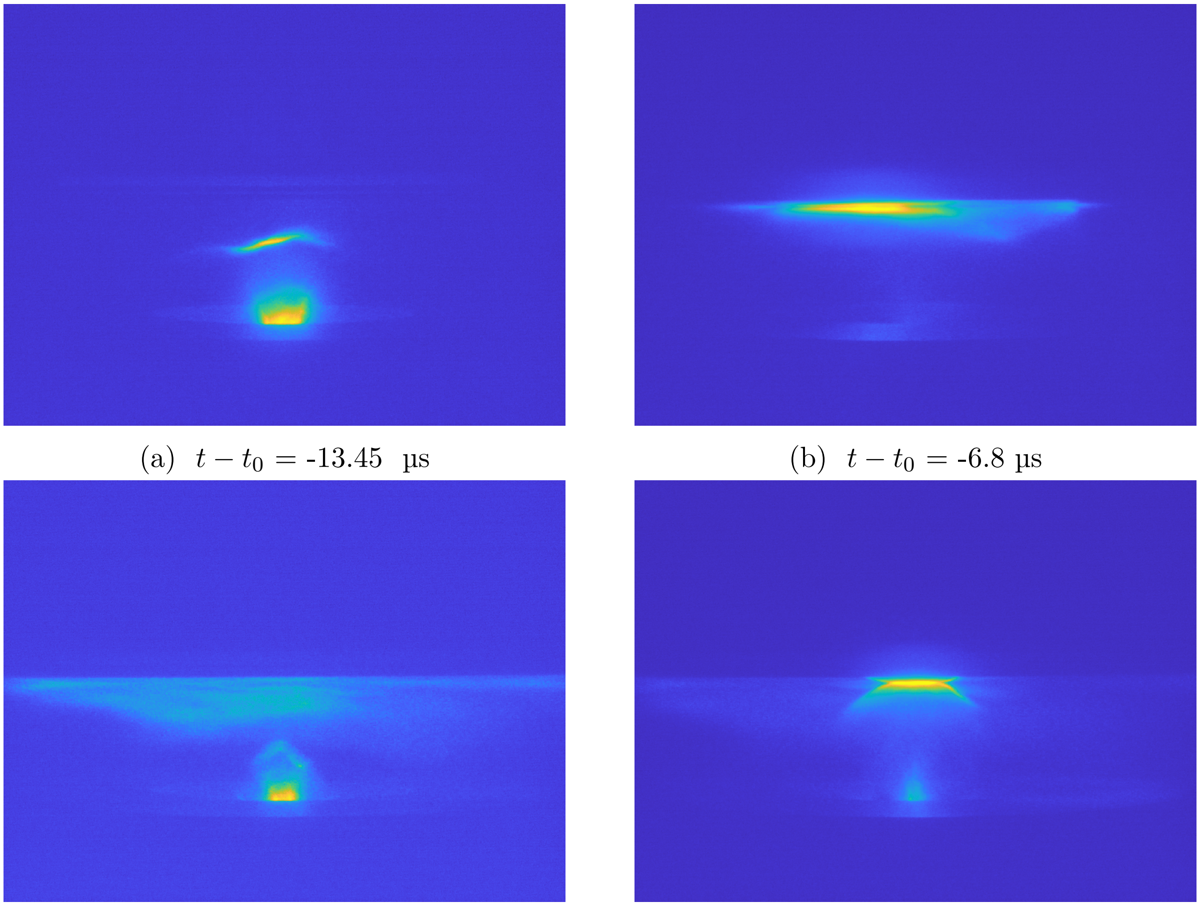

(a) $t - t_0$ = -13.45 µs

(b) $t - t_0$ = -6.8 µs

(c) $t - t_0$ = -2.13 µs

(d) $t - t_0$ = 0.08 µs

Figure 4.3: False color, logarithmic scaled, freeze frame VUV images of experiment evolution. Polycarbonate obstruction is located at z_{pc} = 12 cm. Experiment progression is similar to the campaign reported on in the previous chapter. Here, time is measured relative to the transit time of the post-collision plasma in the interferometer chord located at z = 11.65 cm.

is that quasi-neutrality holds as long as the square of the ratio of the Debye length and ion-ion mean free path is significantly less than one [7]. This arises from the fact that $(Z_i n_i - n_e)/en_e$ is of the same order of $(\frac{\lambda_D}{\lambda_{ii}})^2$ [7]. Using the order of magnitude estimates of density and temperature from our measurements (See Section 4.4), we see that this is in fact the case for our experiment. This allows us to make further inferences about the presence of electron temperature gradients in our plasma as well. The lack of charge separation implies that any ambipolar electric fields due to charge separation are likely not present in our experiment [30, 33]. Because we know that ambipolar electric fields are on the order of electron temperature gradients present in our experiment [23, 32, 45], this implies that our plasma is quasi-neutral, with small or negligible electron temperature gradients between the pre- and post-shock region, suggesting that the effects of electro-diffusion can be safely neglected, a conclusion that is in agreement with both our previous studies as well as work done on experiments within similar parameter spaces [15, 23, 32].

Table 4.2: Order of magnitude estimates of relevant scale lengths in the experiment help justify the quasi-neutral approximation [7], with the spectrometer survey region remaining free of plasma sheath effects.

λ_D (mm)	$\frac{\lambda_D}{\lambda_{ii}}^2$
« 1	« 1

4.3 Observed transition towards intensity separation between ion species

Within our experiment, three species are consistently observed in the emission spectrogram, attributable to N-II (399 nm), Ar-II (435 nm) and Al-III (453 nm). Aluminum is consistently the brightest line of interest, suggesting that the impurity concentration [47] in these experiments are quite significant compared to the previous campaign [15]. We do not observe carbon hydrogen or oxygen lines in our analysis, leading us to conclude that the dominant impurity source in this experiment is the plasma facing insulators, consisting of aluminum, nitrogen and likely boron [47]. We first look at time-resolved measurements of plasma emissivity to understand the evolution of the experiment, alongside the dynamics at play. We refer to emissivity as the wavelength integral of the measured line profile (See B) [54]. These time-resolved measurements are taken with the coarsest spectrometer grating available

(300 gmm) for two primary reasons. Firstly, the coarser grating results in each pixel having a wider wavelength bin, capturing more photons per unit time, resulting in higher signal to noise ratios over shorter exposure times. The finer gratings have narrower wavelength bins across the detector, therefore requiring longer exposure times to obtain usable signals. However, one glaring downside with the coarser grating is that the larger wavelength bin per pixel limits wavelength resolving power, with lines that are not sufficiently isolated from neighboring lines appearing contaminated with their sideband components, therefore unable to be resolved or identified [54]. This phenomena limits our ability to survey the Ar-II line at 435 nm with the 300 gmm grating, due to contaminating elements on each side of the line. Another consequence of this coarser grating is a large instrument function, preventing the inference of electron densities through Stark broadening. Therefore, what is gained in temporal resolution with coarser gratings, is lost in wavelength resolution. To this end, our coarser grating measurements are used to temporally survey the emissivity for Al-III and N-II for the purposes of identifying important features and trends within the experiment itself. To examine the distribution of argon, as well as extract more quantitative information and physical parameters from the experiment, we turn to measurements taken at a singular survey time (See Figure 4.3) with the finer grating (2400 gmm) in the proceeding sections.

Figure 4.5 presents raw, time-resolved spectrograms, taken on-axis at various times for Al-III at 453 nm and N-II at 399 nm. For Al-III, these shots were taken with exposure times of 150 ns, where shots with N-II used an exposure time of 500 ns to obtain usable signals. While these exposure times are larger than the ≈ 3 ns exposure used for the camera images in the previous section, they are sufficient for identifying temporal trends in plasma emissivity for each of these respective species. Each of these frames are oriented such that the horizontal axis is wavelength, and the vertical axis represents the spatial location mapped by each of the fibers in the telescope array. It is also important to note that these raw measurements are chord-integrated [10, 21]. The topic of Abel inversions and off-axis contributions to these measurements will be addressed in the proceeding sections [26, 27].

Starting with Al-III, the first frame is provided right as the shock layer is beginning to clear the z = 11.65 cm station. This is consistent with the spectrograms that show that over the exposure time, the viewing chords closest to the obstruction are illuminated with a maximum intensity nearest to the obstruction. Over the next ≈ .7 µs however, we observe successive illumination of the viewing chords farther away from the obstruction, with the maximum emissivity now being observed farther away from the obstruction. It is important to note that over the course of this time, the interferometer traces indicate that the shock layer is moving towards the obstruction (up the image). Interestingly, this reverse-propagating illumination of viewing chords is not observed in N-II images, where the peak emission is consistently observed in the viewing chord closest to the obstruction. This provides the first hint of diffusive mechanisms present in the shock, as binary-ion diffusion theory predicts that in the center-of-mass frame, lighter ion species diffuse towards the pre-shock region (closer to the obstruction), while heavier ion species diffuse towards the post-shock region (away from the obstruction), which are consistent with these initial observations [23, 30, 31, 32].

4.4 Temperature and density distributions inferred from Al-III lines

While the trends established in Section 4.3 are potential evidence of species separation within a plasma shock, further quantification requires an understanding of the general trends associated with electron temperature and electron density. This is due to the fact that line emissivity is a convolution of density dependent and temperature dependent effects, as de-

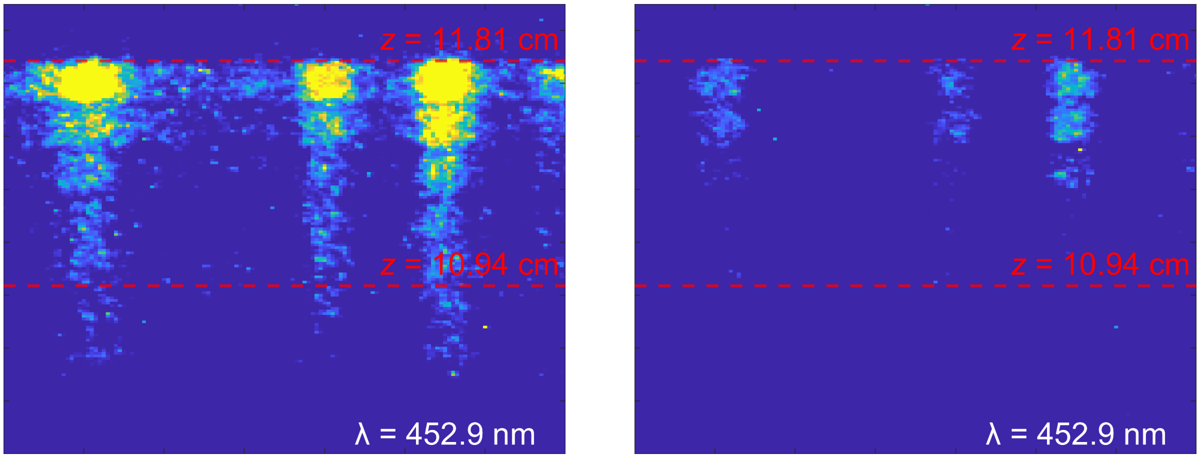

(a) Al-III: $t - t_0$ = -.18 µs (b) Al-III: $t - t_0$ = .28 µs

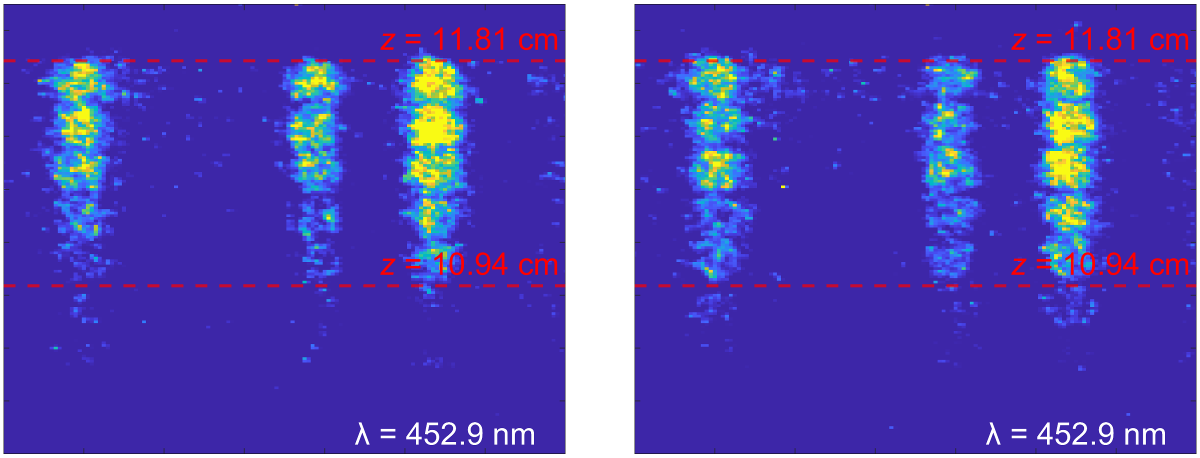

(c) Al-III: $t - t_0$ = .55 µs (d) Al-III: $t - t_0$ = .75 µs

Figure 4.4: False-color, chord-integrated spectrograms of Al-III taken on-axis with a coarse diffraction grating (300 gmm) and low exposure time (150 ns) show that over time, Al-III at 453 nm is emitted in viewing chords farther away from the obstruction), which is in the opposite direction of the forward propagating shock, which travels up the image frame.

tailed in Section B and Ref. [54]. As it happens, the Al-III lines present in our experiment provide a unique diagnostic opportunity for inferring both parameters, while taking advantage of the spatially resolved spectrometer diagnostic, equipped with the finer diffraction grating.

Regarding temperature, our PrismSPECT simulations show that in the non-LTE regime, line ratios between Al-III at 453 and 448 nm are primarily sensitive to electron temperature. This

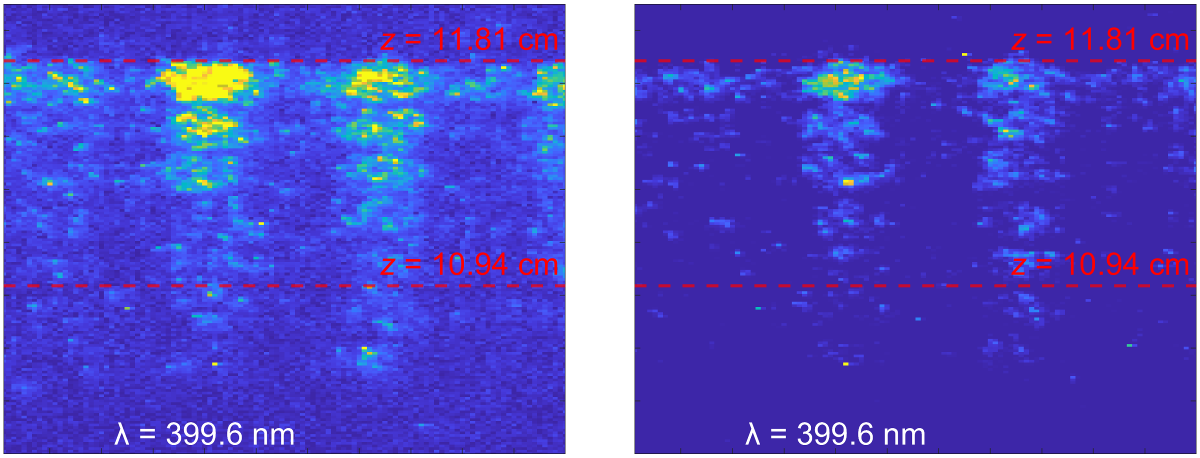

(a) N-II: $t - t_0 = .02$ µs (b) N-II: $t - t_0 = .27$ µs

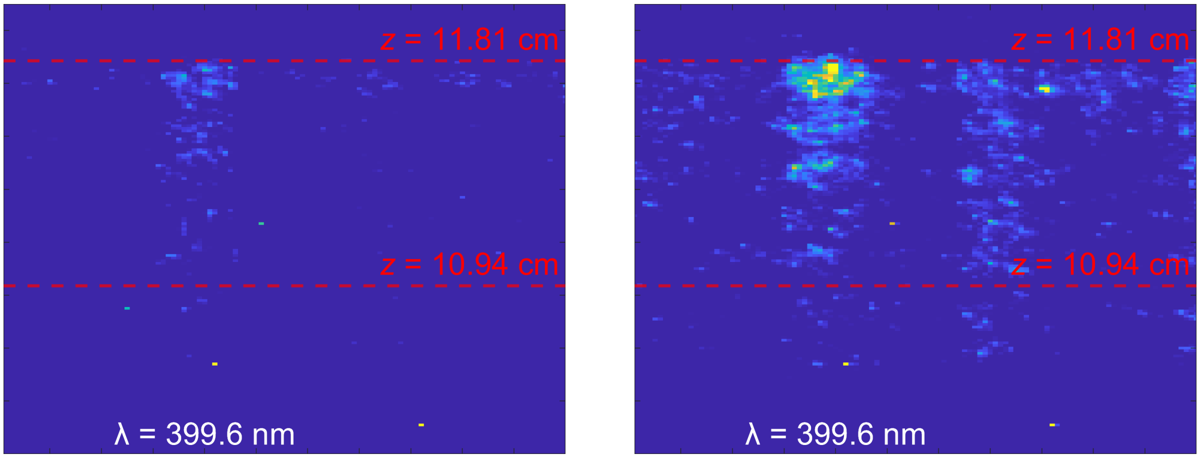

(c) N-II: $t - t_0 = .5$ µs (d) N-II: $t - t_0 = .6$ µs

Figure 4.5: False-color, chord-integrated spectrograms of N-II taken on-axis with a coarse diffraction grating (300 gmm) and low exposure time (500 ns) show that contrary to the Al-III evolution, peak N-II emission is consistently measured in the viewing chord nearest to the obstruction (top of image).

is best exemplified in Figure 4.6. It is important to note that there is also a slight dependence on total ion density, a point that will be examined in more detail in the proceeding section. Because the line ratio of two lines from the same species is equivalent to the ratio of the line's emission rate coefficients, this ratio is also insensitive to changes in plasma composition (See section B and Ref. [54]). Across all permutations of composition and density, this line ratio method can be used to confidently resolve T_e within ± .05 eV, which is sufficient to establish general trends in T_e across the experiment time.

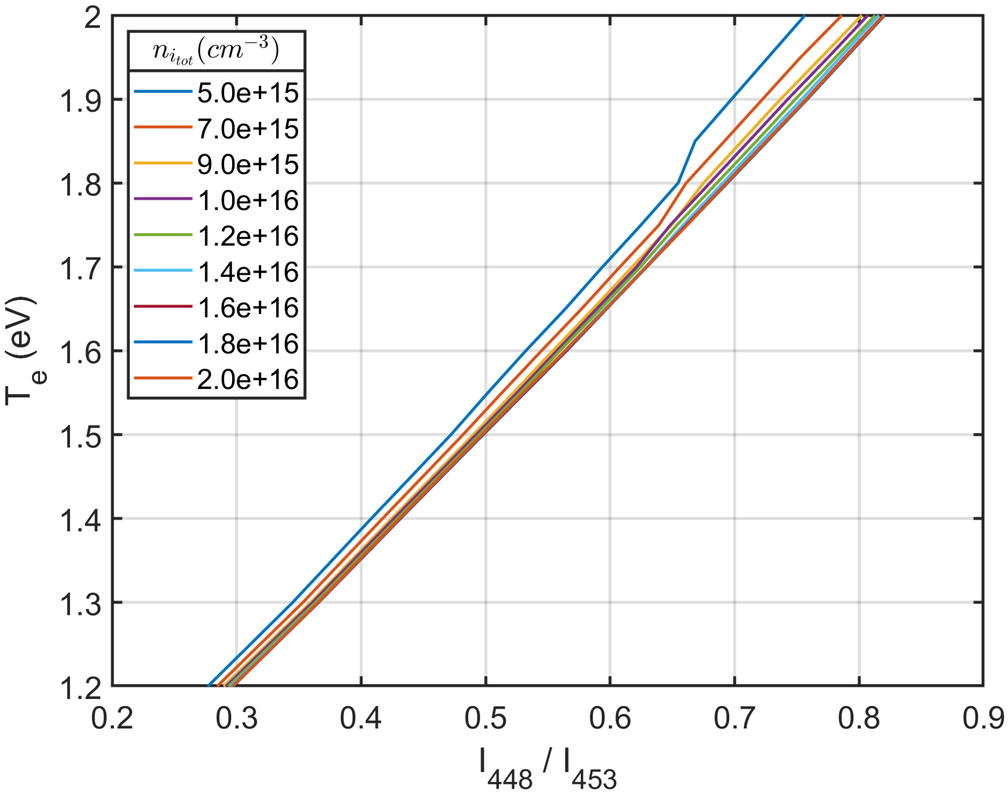

Figure 4.6: Experimental line ratios can be compared to these PrismSPECT simulated ratios to obtain estimates of T_e. These ratios are primarily sensitive to changes in T_e, with a slight dependence on total ion density as well. This dependence on $n_{i_{tot}}$ will be addressed in the proceeding section.

Another advantage of Al-III lines is that the Al-III line at 453 nm is an ideal candidate for Stark-broadening analysis, consistently serving as the brightest line in any recorded spectrogram with recently published results indicating that this line's Stark width is more sensitive to changes in n_e than any other Al-III line within our survey range [49]. Therefore, Stark broadening analysis of this line gives us the opportunity to validate our interferometer measurements with spatially resolved, Stark-inferred estimates of n_e.

Figure 4.7 presents averaged normalized Stark-inferred n_e (top) and averaged normalized

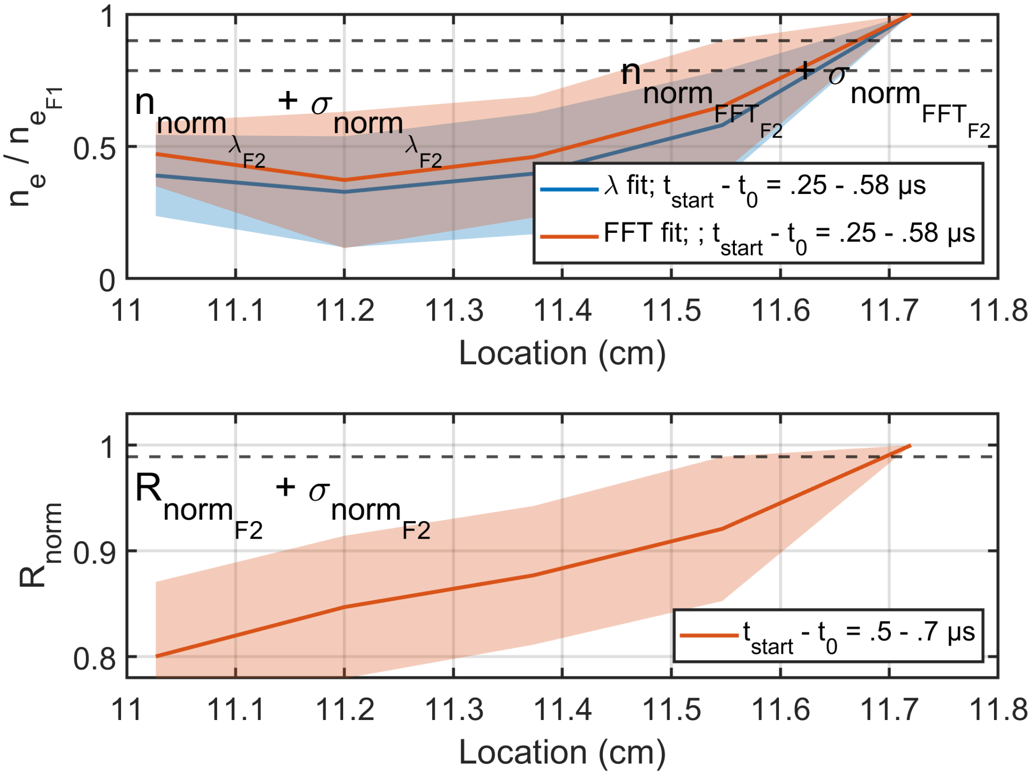

Figure 4.7: Averaged F1-normalized, Stark-inferred n_e and aluminum line ratios, R, alongside gel-shaded 95% confidence intervals inferred from the Al-III impurity lines show that both $R = I_{448}/I_{453}$ and n_e are highest in the viewing chord closest to the obstruction. Dashed lines help emphasize that this feature is both statistically significant, and therefore can be used to interpret line emissivity measurements in the proceeding sections. These parameters are inferred from chord-integrated aluminum measurements, where we assume envelope of the recorded line profile is due to the densest and hottest part of our plasma, likely located along the bore-sight axis. The proceeding section helps to verify this assumption, by showing that the off-axis contribution of emissivity to on-axis chord-integrated spectra is minimal, allowing us to use these measurements to gauge general trends in T_e and n_e across the shock.

line-ratios (bottom) over times where the shock is present in our experiment. All parameters are normalized to the value in the viewing chord closest to the obstruction before being averaged over the shot set, so that this Figure can be used to gauge the evolution of the electron parameters relative to the first fiber in the telescope array. Because line fitting routines are shown to have minimal error when each of the convolved line widths are of similar magnitude relative to one another [20], all the Stark-inferred shots use a spectrometer slit width of ≈ 50 µm, which ensures comparable Lorentzian and Gaussian instrument widths, and therefore, high confidence in the optimized fitting parameters. One consequence of this is that while line-ratios can be extracted from all shots where Stark-broadening is assessed, Stark-broadening cannot be assessed in all shots where line-ratios are extracted, as many of these shots use much higher slit widths (≈ 130 - 150 µm) at the benefit of lower exposure times, but at the cost of larger instrument widths. The parameter t_{start} corresponds to the start time of the spectrometer exposure, with exposure times on the order of 1-2 µs being used for this analysis. Due to these extended exposure times required for the Stark broadening analysis, both the Lorentzian and Gaussian FWHMs are optimized during the fitting process, since bulk hydrodynamic motions, turbulent motions and and thermal motions could all contribute appreciably to Doppler broadening over the exposure time [10, 21, 32], which must be properly accounted for. Across all fits in this shot set, the typical wavelength fits are independently verified by fits in the Fourier domain [20] (See Figure 4.7), which provide confidence that the optimized line widths are representative of the experimental data. In practice, the Gaussian widths fluctuate by a factor of 1 - 1.5 from viewing chord to viewing chord, with no discernible trend. These fluctuations are likely due to the fact that contributions from bulk, thermal and turbulent motions are unsteady and non-uniform across the experiment geometry, resulting in different effective Doppler shifts being observed in the different viewing chords over the prolonged exposure times in the experiment [10, 21, 32]. Despite these fluctuations in the Doppler component, the averaged Stark inferred n_e traces clearly show that n_e consistently peaks in the viewing chord closest to the obstruction, a feature shown to be statistically significant when taking the gel-shaded 95 % confidence intervals into account. This suggests that from $t - t_0 = 0$ onwards, n_e increases towards the obstruction. This can be independently verified through the interferometer traces in Figure 4.2 which clearly show that over the averaging time for the Stark-inferred n_e, the peak electron electron density associated with the shock layer is clearing the z = 11.65 cm station, and moving through the 11.72 cm F1 station and is traveling closer to the obstruction. Because our previous analysis on shock formation, density enhancement and interpenetration lengths [15] (See Section 3) suggest that as the shock propagates towards the obstruction, there is additional compression of background material resulting in higher densities closer to the obstruction, this means that at any instant in time after $t - t_0 = 0$, the axial electron density gradient within the post-shock region of the forward propagating shock should point towards the obstruction, peaking in the viewing chord closest to the obstruction, which is consistent with our Stark results.

Focusing on the ratios of aluminum lines, we see that the ratios also consistently peak in the viewing chord nearest to the obstruction, which is shown to be statistically significant when taking the gel-shaded 95 % confidence intervals into account. We limit this analysis to the times of ($t_{start} - t_0$ = .5 - .7) so that we can use these trends to interpret emissivity profiles collected within the following time frame. Because we have shown through PrismSPECT [18] simulations that the Al-III line-ratio serves as a proxy for T_e (See Section B), Figure 4.7 suggests that T_e increases from ≈ 1.6 to 1.8 eV across the viewing chords, peaking in the fiber closest to the obstruction. Due to the slight density dependence in Figure 4.6, each inferred value of T_e can vary by ± .05 eV, depending on the precise value of n_e at each viewing chord. Due to the steep dependence of X^{Pspect} with T_e coupled with the slight density dependence of X^{Pspect} (See Section B), these trends allow us to state that line ratios and n_e increase towards the obstruction and peak in the spectrometer viewing chord closest to the obstruction. But this analysis does not allow us to precisely infer values of X^{Pspect}. This limitation is acknowledged and discussed in the next section as we quantitatively measure line emissivity across the shock.

4.5 Abel inversions and deconvolved intensity profiles

For more quantitative analysis of the features observed in Section 4.3, we adopt a quasi-stationary approach using the finer spectrometer grating. As stated previously, with this grating we can resolve lines that otherwise would have been obscured with the coarser grating, at the cost of longer exposure times. Rather than using exposure times between .1 and .5 µs, we must now use exposure times between .7 and 1.5 µs. Over these longer exposure times, we interpret axial emissivity measurements to be representative of the state that plasma spends the majority of the exposure time in. To make meaningful measurements, we must therefore focus on a period of time where we are consistently observing the reverse-propagating illumination of Al-III presented in Section 4.3, but over a region in time where the evolution of the experiment is as steady-state as possible. This is done by focusing and averaging exposures whose starting time (t_{start}) is between $t_{start} - t_0 = .5$ and .7 µs. This choice is informed by both practical and physics-based considerations. In practice it is difficult to obtain multiple measurements at the exact same time because of the temporal jitter associated with the initiation of the discharge cycle and onset of the shock front in each shot. However, this "tolerance" of .2 µs in the initiation of the exposure capture is small relative to the total exposure times of ≈ 1 µs, such that any variations in emissivity is offset by a larger sample size, effectively improving shot-statistics. The decision to set the starting bound at .5 µs is informed by the time-resolved analysis provided in Section 4.3, which suggested that the reversed illumination of Al-III is completed at this time, with the interferometer traces in Fig 4.2 also indicating that over the range of values of t_{start} (highlighted by a vertical gel-shaded band), electron density is not varying rapidly. These finer grating, quasi-stationary measurements serve as our primary dataset for quantifying the prospect of species separation in the plasma shock.

One important thing to note is that up until this point, the measurements reported in this chapter have been taken on-axis and are chord-integrated. As we will show later on, this is sufficient for interpretation of the Al-III spectra. But due to the radially unconstrained nature of this experiment, understanding the effects of the radial deconvolutions via Abel inversions [26, 27] (See section 3) is crucial to properly interpreting the experimental measurements. Because radial measurements cannot be made simultaneously, we employ a statistical method when performing Abel-inversions [26].

Because we are probing each radial station individually, the best measurements that we are able to obtain are normalized profiles of on- and off axis emissivity, defined as:

$$I_{On_{Norm}} = [I_{On_1}, I_{On_2}, I_{On_3}...]/I_{On_1} \tag{4.1}$$

and

$$I_{Off_{Norm}} = [I_{Off_1}, I_{Off_2}, I_{Off_3}...]/I_{Off_1} \tag{4.2}$$

Where each matrix element corresponds to the different spectrometer viewing chords. From this general form, we realize that given a normalized on-axis emissivity distribution, we can re-construct a corresponding off-axis set, $I_{Off_{Re-constructed}}$, that can be used alongside $I_{On_{Norm}}$ to obtain Abel-inverted emissivities where radial and axial ratios of the inverted quantities are preserved. This is done through the use of a proportionality constant, χ, that can be defined as:

$$I_{Off_{Re-constructed}} = I_{Off_{Norm}}\left(\frac{I_{Off_1}}{I_{On_1}}\right) = I_{Off_{Norm}}(\chi) \tag{4.3}$$

Given a value of χ we can now obtain localized estimates of emissivity for our lines of interest and 95% confidence intervals that have been propagated through the inversion process [51]. We can estimate χ from raw un-normalized on- and off- emissivity estimates, resulting in an average estimate of χ alongside a 95% confidence interval. However, it is important to the note that due to the method in which $I_{Off_{Re-constructed}}$ is determined, it is not physical for the value of χ to vary randomly from one viewing chord chord to the next; each viewing chord must be multiplied by the same value of χ. Therefore, to correctly estimate uncertainties resulting from the inversion process, we must perform an enveloped analysis, where we perform the Abel inversion three times; one assuming the average value of χ and then two more times assuming values of $\chi \pm \sigma_\chi$. For each value of χ, the uncertainties associated with $I_{Off_{Norm}}$ and $I_{On_{Norm}}$ are propagated throughout the inversion process.

This analysis is presented for Ar-II lines in Figure 4.8, as the Abel inversion is crucial to understanding the local emissivity profile for this species. While the chord-integrated on-axis emissivity profiles suggest a near-linear profile that peaks in F1, all iterations of the Abel-inverted on-axis emissivity profiles show that the localized on-axis profile is instead characterized by an emissivity that decays as one approaches the obstruction location, a feature that is shown through the horizontal dashed lines to be statistically significant. This drastic change in profiles is due to the fact that during the spectrometer survey time, χ » 1, which emphasizes the importance of the Abel inversion in cases such as this. Due to our uncertainty in χ, we cannot claim confidence in the exact on-axis emissivity profile of Ar with any certainty. However, the averaged traces and propagated uncertainty presented in Figure 4.8 does allow us to claim that regardless of the value of χ, the localized on-axis emissivity for argon is higher farther away from the obstruction location.

For the cases of Al-III and N-II the value of χ is shown to be « 1. In these instances, the Abel inversion does not change the location of max emissivity as it did with argon. Therefore, we

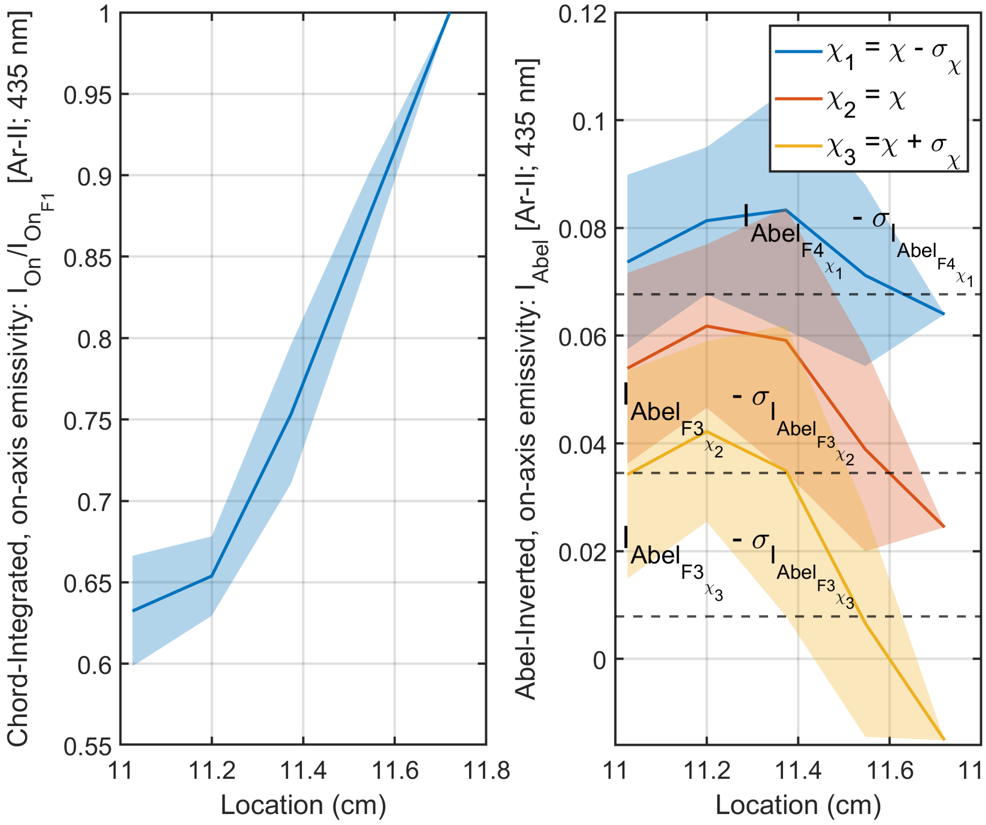

Figure 4.8: The Abel inversion is essential to properly interpreting argon spectrograms, where the localized on-axis emissivity profile displays emissivity which is brighter away from the obstruction; a feature shown by the dashed lines to be statistically significant. Because χ » 1, this feature is obscured in the chord-integrated on-axis measurement.

present peak-normalized chord integrated on-axis emissivity profiles for Al-III and N-II in Figure 4.9 for the purposes of emphasizing the location of maximum emissivity for both lines. Here it is evident that there is a separation of intensity that develops between the heavier (aluminum) and lighter (nitrogen) ion species that is shown to be statistically significant.

The result of this quasi-stationary analysis is that for long exposure shots whose collection time starts between $t_{start} - t_0 = .5$ and .7 µs, statistically significant intensity separation is observed, with the peak argon and aluminum emissivity observed closer to the muzzle of the railgun (nearer to the post-shock region) and peak nitrogen emissivity observed closer to the

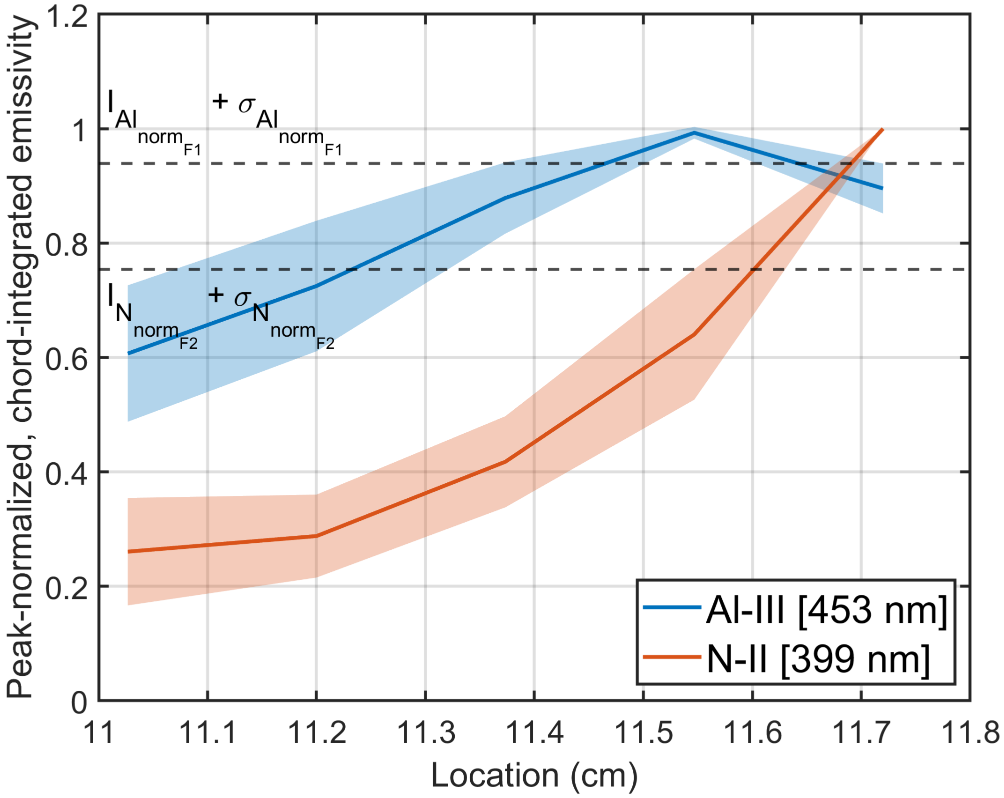

Figure 4.9: Chord-integrated measurements of on-axis emissivity for Al-III and N-II emphasize a statistically significant separation of intensity that is observed between the two species; a feature consistent with the trends hinted at in the time-resolved analysis in Section 4.3

obstruction (closer to the pre-shock region). It is important to note that due to both the fact that we are averaging over a subset in time, as well as the uncertainties involved in the Abel-inversion process, it is only the location of maximum emissivity that we can claim with any degree of certainty. However, given our estimates of electron parameters presented in Section 4.4, we can use physical properties associated with our plasma to make meaningful inferences regarding the distribution of ion species within the plasma shock.

We know from collisional-radiative modeling theory [54] that the emissivity of a line can be cast as being due to the product of the density of the emitting species, the electron density and an equivalent emission coefficient that we can query with PrismSPECT [18], as shown in Eqn. 4.4 (See B, Ref. [54])

$$I = n_s n_e \chi^{Pspect} \tag{4.4}$$

We know from the previous sections that both n_e and line-ratios of aluminum lines peak in the viewing chord closest to the obstruction. However, as discussed previously, we cannot use this information to precisely infer relevant values of χ^{Pspect}. However, we can query the PrismSPECT model to qualitatively understand how increases in both I_{448} / I_{453} and n_e affects the value of $(n_e \chi^{Pspect})$. This is presented in Figure 4.10 , which provides contours of $(n_e \chi^{Pspect})$ for simulated values of n_{tot_i} and I_{448} / I_{453}. We see that in the case of all three lines, as long as n_e and I_{448} / I_{453} is increasing, then the value of $n_e \chi^{Pspect}$ increases as well. This means that during our spectrometer survey time, $(n_e \chi^{Pspect})$ is increasing, with its maximum value located at the viewing chord closest to the obstruction.

Because we now know that $n_e \chi^{Pspect}$ increases as we approach the obstruction, collisional radiative modeling [54] and in particular, Eqn 4.4 tells us that the only way for us to have a decrease in emissivity for argon and aluminum as we approach the obstruction is for their atomic number densities to decrease as well. Thus there is a decay in the heavier ion species as we approach the obstruction.

At the same time, we know from both our Stark-inferred n_e measurements and chord-integrated interferometer measurements that electron density is highest in the viewing chord closest to the obstruction. We also know from our earlier measurements that we are dealing with a quasi-neutral plasma [7, 10, 33]. For a multi-component plasma, this means that the various ion species in the plasma can have drifts relative to the electron layer, but ultimately, they must be balanced, such that the plasma is current-free, leading to the following

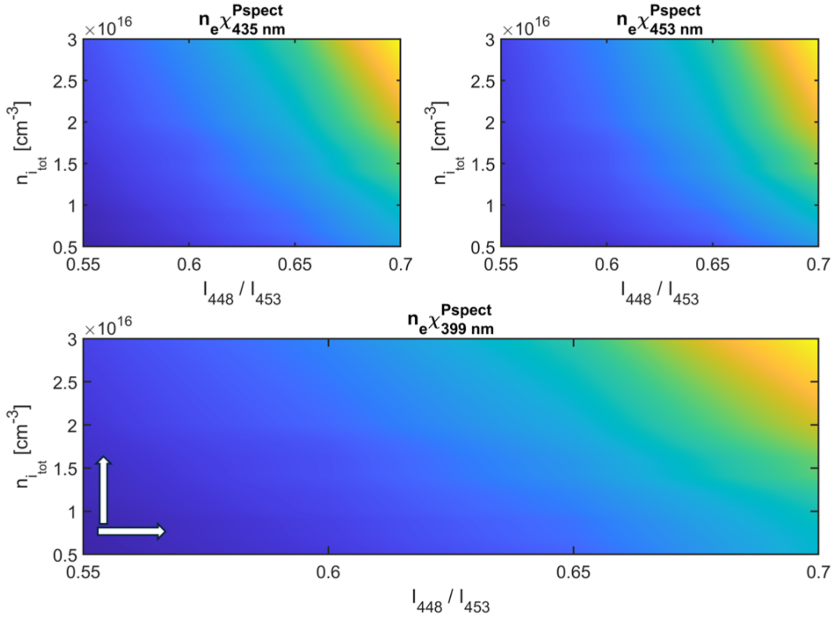

Figure 4.10: Contours of n_eX^{Pspect} across all ion densities, and line-ratios relevant to our experiment. White arrows indicate that as long as either $n_{i_{tot}}$ or the I_{448} /I_{453} line ratio is increasing, then that means that n_eX^{Pspect} must also be increasing. Because our experimentally inferred electron profiles (See Fig 4.7) show that both line-ratios and n_e (and by consequence, n_i) increases towards the obstruction, this means that n_eX^{Pspect} also increases towards the obstruction in our experiment, peaking in the viewing chord closest to the obstruction. this analysis was done using assuming plasmas of 50 % purity (See Fig B.4, but is generalized to all compositions since X^{Pspect} is independent of jet composition (See Fig B.7).

relation: [7]

$$Z_1n_1(u_1 - u_e) + ...Z_nn_n(u_n - u_e) = 0 \tag{4.5}$$

Because our heavier elements, such as argon and aluminum decrease towards the obstruction, the above equation shows that lighter elements in our plasma, (such as nitrogen) must concentrate towards the obstruction (pre-shock layer) to maintain the detailed balance of drift speeds that is required for quasi-neutrality in our system [7]. As a result, our observed intensity separation coupled with the general trends associated with the electron parameters in our experiment is evidence of a separation of the light and heavy elements in the plasma shock.

4.6 Shock front separation and the theory of diffusive mass flux

We now turn to binary ion diffusion theory to validate our experimental results against those predicted to occur from gradient-driven species separation. Once again, we turn to the formalism for diffusive mass-flux in the center of mass frame that is presented in Equation 1.1 [30, 31, 39]. This time however, we look to directly solve the equation for diffusive mass flux. Once the diffusive mass-flux is solved, we can relate it to the diffusion velocities of the light and heavy elements in the center-of-mass (CM) frame of the shock according to the relation [23]:

$$i = \rho_1 v_{D1} = -i = -\rho_2 v_{D2} \tag{4.6}$$

This equation serves to show that in the CM frame (where shock velocity is 0), the diffusion velocities of each species point in opposite directions [23, 32]. The sum of the magnitude of these two velocities represent the velocity of the light species relative to the heavier species in the lab frame [23, 32]. Therefore, the estimated separation from this analysis can be estimated by multiplying this velocity by a characteristic time over which appreciable diffusion occurs.

To obtain an order of magnitude estimate of the separation that can theoretically occur, it is important to properly account for the dominant physical mechanisms at play in our calculations. The most important mechanism is the role of ion heating in the shock [23, 24, 32] , which is a parameter that we cannot reliably measure. Prior to this study, there have been significant experimental studies on plasma shocks in similar a parameter space where measured ion heating through high resolution Doppler spectroscopy has been compared to theoretical calculations assuming that the bulk kinetic energy of the pre-shock flow was converted to ion heating [24, 32]. Recent analysis of this kind done by Langendorf et al. [24] have experimentally characterized ion heating for a variety of single ion species plasmas, showing great agreement between these theoretical estimates and experimental measurements for the case of collisional plasma shocks [24]. The analytic form for ion heating in a plasma shock is derived and presented as a jump condition similar to that of the Rankine-Huguenot condition under the assumption that we are looking at a two-fluid plasma shock consisting of electrons and a single ion species, and that all of the shock heating goes to the ions [24]. While this formalism is purely theoretical, its benchmark studies have shown that this analysis can be used to perform order of magnitude calculations of ion heating, and consequently, of species separation [23, 24].

The jump condition is presented as [24]:

$$\frac{T_{i_2}}{T_{i_1}} = [1 + \frac{2(\gamma-1)\gamma M^2 + 1}{(\gamma+1)^2 M^2}(M^2-1)](\alpha+1) - \alpha \tag{4.7}$$

Where M is the pre-shock Mach number in the reference frame of the shock, and α is $\frac{\bar{Z}T_e}{T_{ipre}}$ [24]. We take this value to be approximately 1, as $\bar{Z} \approx 1$, and we expect temperature equillibration between the ions and electrons in the pre-shock region [55].

The dependence on atomic mass in this jump condition arises from the pre-shock Mach number, as different species with the same velocity will have a different associated sonic speed [23, 24]. While previous analysis has used the second jet parameters for an order-of-magnitude estimate of the jump conditions [15], we recognize that for the case of a shock propagating towards the obstruction, pre-shock quantities refer to the background plasma right between the shock front and obstruction, whose pre-shock velocity is the shock velocity in the reference frame of the shock, not dissimilar to the classic moving shock problem from hydrodynamics [2]. Thus, we estimate the pre-shock velocity based off the transit time of the shock between our two interferometer chords. The resulting velocities, Mach numbers, and post-shock ion temperatures are provided for the ion species of interest in Table 4.3. We see that theoretical estimates of ion temperature increase with atomic mass, consistent with other experimental studies and simulations [23, 24, 32]. Because temperature separation is a higher-order effect [23, 24, 32], diffusion theory assumes that there is a single ion temperature in the post-shock region. Thus, we adopt a similar approach to Simakov et al. [56], where the post-shock temperature is a weighted average (denoted T_{Avg}) of its constituents by molar fraction.

A tractable estimate of the molar fraction of each species in the plasma as a function of time and space is not possible. However, under certain assumptions that better constrain the problem, plasma jet purity can be estimated using line ratios of strong isolated lines in the system and PrismSPECT simulations [18]. We estimate the pre-shock plasma composition through a long exposure (5 µs) spectra of the pre-shock background plasma prior to any shock formation. We perform this analysis by only considering quantities associated with the z = 11.72 cm viewing chord, as this location is closely aligned with the z = 11.65 cm interferometer chord, which is used to estimate gradients and scale lengths for the diffusion calculations.

We know from previous experiments [15] that the first jet in the discharge cycle is typically of high purity, as the bulk of the material being ionized and accelerated is from the neutral gas injection prior to discharge. As an order of magnitude estimate of this purity, we compare line ratios of the high intensity, isolated lines of Al-III line at 453 nm and Ar-II line at 488 nm with various PrismSPECT simulated spectra [18] whose composition is some percentage of the working gas supplied to the system (.9Ar + .1N_2) accompanied by an impurity contribution from the shapal [47] insulators (AlN + BN). Because bright, isolated nitrogen and boron lines were not accessible in the background plasma measurements, this methodology helps us to easily infer composition based on our available measurements. This analysis estimates a jet purity of 70%, which is consistent with the purity estimate of $\approx$ 80% for the argon-only jets in the previous chapter [15]. This estimate of plasma purity is used to infer T_{Avg} in Table 4.3. It is worth noting that this long exposure time primarily captures line emission due to the stagnation event of the first jet against the obstruction, which provides bright impurity lines that can be used for this analysis. However, when performing more time resolved spectroscopy to observe the state of the background plasma immediately before the arrival of the second jet, we observe that the emission at z = 11.72 cm is almost exclusively argon, with no impurity lines present. Because we know from the equivalent rate coefficients queried in Section B that at the same temperature and density conditions, the emission rate of Al-III is orders of magnitude higher than the emission of Ar, this absence of lines is likely due to change in composition of the background plasma as it slowly expands and diffuses after stagnation. This implies that the pre-shot jet purity of 70 % is likely an underestimate, with the pre-shock region immediately preceding the onset of the collision event likely consisting of more argon. Therefore, this conservative estimate of composition results in a conservative estimate of ion heating, and by extension, separation.

We also conservatively estimate the plasma parameters necessary for calculating the diffusion coefficients from the interferometer measurements at z = 11.65 cm to estimate a minimum separation distance present in our experiment. Available Stark broadening measurements

Table 4.3: Post-shocked ion temperature is inferred based on interferometer measurements and temperature jump conditions derived by Langendorf et al. [24]

v_{shock} (km/s)	Mach No. (Ar)	Mach No. (Al)	Mach No. (N)	Mach No (B)	T_{Ar} (eV)	T_{Al} (eV)	T_N (eV)	T_B (eV)	T_{Avg} (eV)
≈20	5.1	4.2	3.0	2.7	32.4	22.3	12.1	9.6	24.2

allow us to assume an order of magnitude estimate of the post-shock region as 1×10^{16} cm^{-3}, while the chord integrated interferometer traces allow us to estimate the pre-shock background plasma density as 2.8×10^{15} cm^{-3}. As a conservative estimate of diffusive mass flux, we only consider the effects of barodiffusion, where we estimate L_{sw} as .4 cm based on the transit time of the shock through the 11.65 cm chord, inferred from the FWHM of the relevant phase structure. We assign ∇C as 0 [23], assuming that any concentration gradient is induced through species separation over a characteristic time of $\approx$ .5 μs, which is based on the time scale of the reverse-propagating Al-III features presented in Section 4.3.

The results, as shown in Table 4.4 compares the estimated light-heavy ion separation to the minimum species separation inferred experimentally from the peak separation in our quasi-steady emissivity measurements. All estimated quantities are of the same order of magnitude indicating congruence between theory and experiment. Because ion heating [24] is included in these calculations, the calculated separation could be enhanced by thermodiffusion [31]. Further analysis of the various diffusion terms indicate that our diffusion coefficients and relevant gradients are generally higher than those inferred by Byvank et al. in their shock experiments [23], which is the only other experiment to directly observe species separation in plasma shocks. This make sense given that our experiment has higher density gradients, and a higher pre-shock mass concentration of the heavier ion species, which results in higher post-shock temperatures under similar velocities, all of which couple into a stronger total ion pressure gradient [15, 23]. Despite our experiment containing stronger gradients, the shocks

Table 4.4: Congruence between theory [23, 30, 31, 32] and experimental inferences help to validate our line emissivity analysis

Min. light-heavy separation (Theory)	Min. argon-nitrogen separation (Exp)	Min. aluminum-nitrogen separation (Exp)
≈ 3.2 mm	≈ 3.5 mm	≈ 1.7 mm

in the experiments by Byvank et al. occur over longer times scales, resulting in comparable separation being induced when compared to our experiment [23].

4.7 Conclusion

The structure of multi-ion-species shock was extensively studied through the use of spatially resolved spectroscopy. Abel-inverted axial emissivity profiles interpreted through collisional radiative modeling [26, 27, 54] provided proof of separation between light (nitrogen) and heavy elements (argon and aluminum) within the plasma shock. Theoretical estimates assuming a binary ion diffusion model [30, 31, 45, 56] suggests that the presence of a density gradient alongside shock heating of ions results in millimeter scale species separation, which is on the order of the axial emissivity measurements. This work is some of the first to be conducted in a plasma shock with more than two ion species, and can serve as a foundation for more sophisticated plasma shock experiments in the future.

Chapter 5

Summary of research deliverables and future work

The linear railugn experiment at Virginia Tech's EPPL has provided a strong foundation conducive to fundamental plasma physics research. Throughout this dissertation, the author has leveraged the diagnostic capabilities of the experimental setup to perform a detailed study on colliding plasma jets and collisional plasma shocks, which have been emphasized through the following milestones:

Centimeter scale shock structures have been identified during the collision of a supersonic plasma jet with a stagnant background plasma [15]. These shock structures have been identified as low temperature and highly collisional. Ion-ion stopping distances have suggested that the supersonic jet acts as a snowplow, compressing the background material and driving shock formation.

A spatially resolved spectroscopy diagnostic has been developed to enable millimeter scale spatial resolution of plasma parameters and line emissivity. A modular telescope design allows for the spatial resolution of the spectrometer collection optics to be tuned based on experimental configuration and diagnostic requirements. Line emission from impurity aluminum lines present a unique diagnostic opportunity allowing for the inference of T_e from line ratios [18, 54] and n_e from Stark widths [20]. To the author's knowledge, millimeter scale spatial resolution of these parameters in the diagnosis and characterization of collisional plasma shocks have not been previously reported in the literature. The ability to translate telescope positions to different radial locations and Abel-invert [26, 27] line emissivity measurements allow for the more localized estimates of line emissivity within our experiment, a technique not commonly used in similar experiments, but turns out to be of utmost importance for characterizing the distribution of ion species in radially unconstrained experiments such as this.

Spatially resolved spectrogram measurements on multi-ion-species plasma shocks have suggested the presence of gradient-driven species separation, which drives heavier ion species towards the post-shock region and lighter ion species towards the pre-shock region over a time scale of ≈ .5 µs. These results have been validated through measurements of line emissivity and experimental inferences of electron temperature and electron density that have been paired with fundamental concepts pertaining to collisional radiative modeling [18, 54] to understand the distribution of ion species within the plasma shock. These results have also been benchmarked against binary ion diffusion theory [30, 31, 45, 56], which primarily uses data from our interferometer diagnostic to obtain estimates of separation that are on the order of our spectroscopy results. This congruence between independent measurement techniques helps to validate the experimental results. To the author's knowledge, these results are some of the first to be performed in a plasma shock with more than two ion species, as many experiments up to this point only consider binary ion systems [23, 32]. The importance of Abel inversions [26, 27] in properly interpreting argon spectrograms highlight the importance of understanding the radial distribution of line emissivity, rather than relying on chord-integrated measurements in radially unconstrained experiments such as this.

However, this experiment is not without its constraints. The most notable is the use of only one telescope that prevented us from being able to obtain simultaneous measurements of plasma emissivity at different radial stations. This can be remedied through the use of a second set of collection optics such that two telescopes can be affixed to the vacuum chamber at the same time. Similarly, extending the interferometer setup beyond the two-chord system will also allow for simultaneous measurements of phase shift, and consequently, chord integrated n_e at various radial stations. While these suggestions are potentially costly, they will negate the need to constantly re-configure the diagnostic setup between shots which will minimize the amount of shots needed to obtain statistically significant results.

That being said, the experimental configuration as it stands is still suited to study a wide range of fundamental physics processes. These range from a more detailed study of the effect of ionization processes on shock formation [19], physics of magnetized plasmas [57], and a study of turbulence in low temperature plasmas and plasma shocks [58].

Appendices

Appendix A

Derivations

A.1 Derivation of interferometer/phase shift relation

Following the derivation from Hutchinson [10], the phase difference between a laser beam through the plasma and a reference beam relates to the plasma's index of refraction (N) through the relation [1, 10, 14]

$$\Delta\phi = \int (N-1)\frac{\omega}{c}dl \tag{A.1}$$

Where the integral is taken across the length of the probe beam through the plasma [1, 10, 14]. The index of refraction is defined as the vacuum speed of light normalized to the phase velocity of light in the plasma [10].

For an unmagnetized plasma, the index of refraction is given as [10]:

$$N^2 = 1 - \frac{\omega_p^2}{\omega^2} \tag{A.2}$$

where ω_p is the plasma frequency and ω is the angular frequency of the laser beam [10]. This can also be written in terms of the electron density of the plasma (n_e) and cutoff density (n_c)of the laser beam through the plasma as [10]:

$$N^2 = 1 - \frac{n_e}{n_c} \tag{A.3}$$

By plugging A.3 into A.1 and taking $n_e \ll n_c$, we get [10]:

$$\Delta\phi = \frac{\omega}{2c} \int \frac{n_e}{n_c} \tag{A.4}$$

Given that [10]:

$$n_c = \omega^2 m_e \epsilon_0 / e^2 \tag{A.5}$$

We arrive at the colloquial relation between phase difference and line-integrated electron density [10]:

$$\Delta\phi = \frac{e^2\lambda}{4\pi\epsilon_0 m_e c^2} \int n_e dl \tag{A.6}$$

Where laser frequency ω has been converted into wavelength [10]. Using SI units, $\Delta\phi$ is given as radians, $\int n_e$ is given as m^{-2} and the coefficient to the integral is given as $[rad \times m^2]$ [1, 10, 12, 14]

A.2 Derivation of Abel inversion length matrix

The analytic form of $L_{i,j}$ can be determined through geometry for three specific cases as follows:

1. For the case of $i > j$, $L_{i,j} = 0$. This can be seen in Figure A.1 where sightline '2' does not pass through radial zone '1', and sightline '3' does not pass through radial zone '2'.

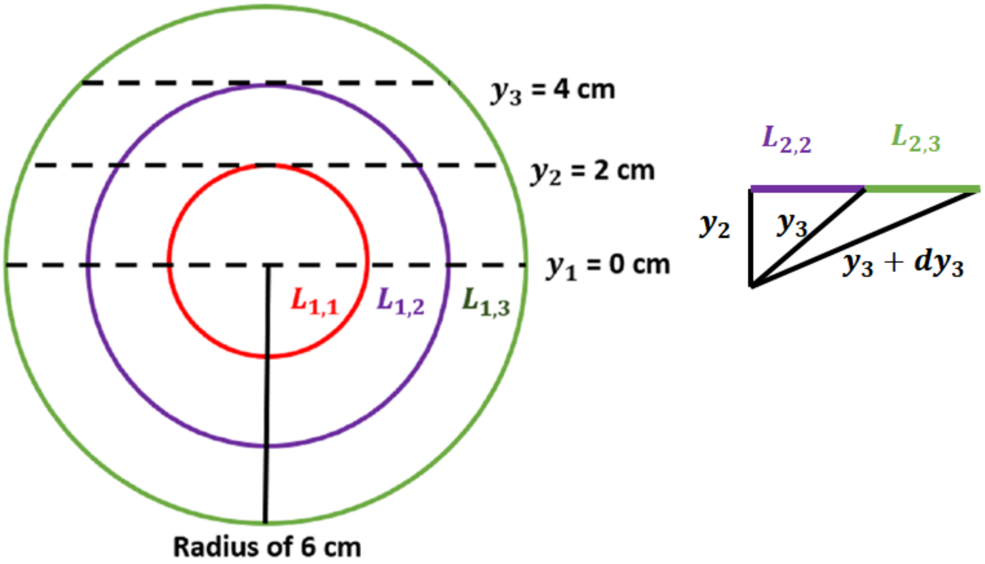

Figure A.1: Axi-symmetric plasma model used for Abel inversions (left), alongside geometric principles used for deriving the analytic form of the length matrix (right) [26]. This model is based of the ones used by Gornushkin et al. [27], where sightlines are tangential to radial zones. Plasma cross-section reproduced from Ref. [15]: AI Mohammed and CS Adams. Ion shock layer formation during multi-ion-species plasma jet stagnation events. Physics of Plasmas, 29(7):072307, 2022., with the permission of AIP Publishing.

2. For the case of $i < j$, Pythagorean's theorem, comes into play. Associated with each chord location y_i, is the distance between the adjacent sightlines, dy_i, such that $y_{i+1} = y_i + dy_i$. One consequence of this is that the inferred radius of the plasma column is bounded by the farthest sightline that is setup, such that $r = y_{i_{max}} + dy_{i_{max}}$, which is necessary to close the system of equations used to solve for n_j. This is why it

is important to set up a sufficient number of sightlines, such that the chord-integrated density tends to zero as 'i' tends to 'i_{max}' [10].

To solve for $L_{i,j}$, we consider the simply case of solving for $L_{2,3}$ in a plasma column, which is illustrated in Figure A.1 [15, 26, 27]. Pythagorean's theorem, $b = \sqrt{c^2 - a^2}$ allows us to write the analytic form for $L_{2,3}$ as:

$$L_{2,3} = \sqrt{(y_3 + dy_3)^2 - y_2^2} - \sqrt{y_3^2 - y_2^2} \tag{A.7}$$

This can be generalized for the case of $j > i$ as:

$$L_{i,j} = \sqrt{(y_j + dy_j)^2 - y_i^2} - \sqrt{y_j^2 - y_i^2} \tag{A.8}$$

3. For the case of i = j, Equation A.9 reduces to

$$L_{i,j} = \sqrt{(y_j + dy_j)^2 - y_i^2} \tag{A.9}$$

A.3 Propagation of error for Abel-inverted datasets

To perform an Abel inversion for spectrometer data requires a chord integrated measurement at a series of of sightlines, $[y_1 ... y_n]$ and associated uncertainties $[\sigma_1 ... \sigma_n]$ where $y_1 \pm \sigma_1$ represent the chordal information taken on axis, such that the line of sight passes right down the middle of the plasma's circular cross section [15, 27].

The formalism for Abel inversions is simply a linear sum of the sightline measurements, where each coefficient corresponds to the inverse of the length matrix (See section A.2) [26]. As a result, error propagation for this analysis can be derived from the general formalism for propagation of error can be applied [51], where the uncertainty in a function of independent variables such as X(a,b,c) is generally inferred as [51]:

$$\sigma_X = \sqrt{(\frac{\partial X}{\partial a}\sigma_a)^2 + (\frac{\partial X}{\partial b}\sigma_b)^2 + (\frac{\partial X}{\partial c}\sigma_c)^2} \tag{A.10}$$

By evaluating the partial derivatives we obtain the final expression for the propagated error for the localized on-axis component as:

$$\sigma_X = \frac{1}{2}\sqrt{(L^{-1}_{1,1}\sigma_1)^2 + ... + (L^{-1}_{1,n}\sigma_n)^2} \tag{A.11}$$

Appendix B

Theory of plasma spectroscopy

While the act of recording an emission spectrogram is fairly easy, correctly interpreting these measured line profiles rely on the understanding of a vast amount of nuances and physics processes [10, 21, 54]. This section is meant to highlight a few key concepts that are essential to the processing and interpretation of the data provided in this dissertation. I will leave the comprehensive overview of the theory of plasma spectroscopy to the more detailed sources referenced throughout this section [10, 21, 54].

B.1 Units in emission spectroscopy

For the purpose of identifying atomic species in a plasma, the intensity of atomic line profiles are often presented in arbitrary units [A.U.], frequently normalized to the value of peak intensity in the spectrogram [13, 15, 17, 19]. But quantitative interpretation of experimental and simulated spectrograms often require an understanding of the physical units at play [10, 21, 54]. This section details the units for spectrograms simulated through PrismSPECT [18] and relates them back to measurements obtained with a relatively calibrated system such as the one detailed in this dissertation.

Emission spectra are reported as specific intensity in units of erg/cm^2/s/ster/eV [54]. The breakdown of these units are as follows:

- Erg can be interpreted as a unit of intensity, which can often be interchangeable with photon counts [21, 54].
- cm^2 corresponds to differential area, often corresponding to that of the emitting surface [21]
- S refers to the time interval [21, 54]
- The steradian is the unit of solid angle of the emitting object as seen by the detector surface [21]
- eV is the energy interval. While simulated spectra are primarily reported as a function of eV, experimental units are reported as a function of wavelength (nm). The relation between these two independent variables requires the use of a Jacobian [21, 28, 54] (See below).

These units work together to describe the specific intensity associated with rays of a certain frequency range, subtending a solid angle that cross through differential area over a specified unit of time [21, 54]. Figure B.2 shows the geometry associated with description [21]. This specific intensity is averaged over the line of sight [21, 54]. Therefore, Abel-inverted intensity [26] is in units of $\mathrm{erg/cm^3/s/ster/eV}$ [21, 54]. By integrating over these quantities, we can determine the total energy measured by the detector.

B.2 Integrating line-profiles and the use of the Jacobian

The profile of an emission line typically defaults to a Voigt profile, which consists of a Gaussian and Lorentzian component [10, 21, 54]. These line profiles may be represented as

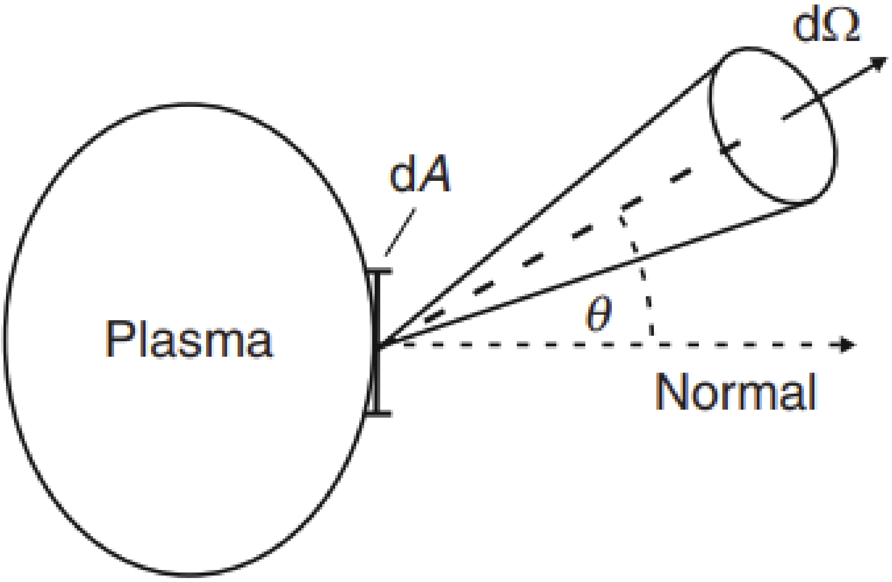

Figure B.1: Nominal geometry associated with an emitting surface on the plasma [21]. Units of emissivity allow for a complete description of line emission, involving the associated time, energy, and direciton [21]. Image used with permission of Springer Nature BV, from Ref [21]: Hans-Joachim Kunze. Introduction to plasma spectroscopy, volume 56. Springer Science, Business Media, 2009.; Permission conveyed through Copyright Clearance Center, Inc.

a function of wavelength or energy [10, 21, 54]. In either case, the analytic form of the line profile, V, is area normalized to one [10, 21, 54], such that:

$$\int V(\lambda)\,d\lambda \;=\int V(E)\,dE \;=1 \tag{B.1}$$

The line intensity recorded by the spectrometer is of the analytic form [54]

$$f=\epsilon_{pk}V \tag{B.2}$$

Where ϵ_{pk} Is the line emissivity, and V is the line profile, represented either as function of energy or wavelength [54]. To recover the emissivity associated with the line, we simply integrate along the line profile [10, 21, 54]. Due to Eqn B.1, the convoluting effect of the line profile vanishes [10, 21, 54]. For the cases where the line profile is measured as a function of wavelength, this presents as [21, 54]

$$\epsilon_{pk} = \int \epsilon_{pk} V(\lambda)\, d\lambda \; = \epsilon_{pk} \int V(\lambda)\, d\lambda \; = \epsilon_{pk}(1) \tag{B.3}$$

To prove that the emissivity of the same line presented as a function of wavelength and energy is equivalent, we turn to Planck's law, which defines the relation between the energy and wavelength of a photon [28]:

$$E = \hbar c/\lambda \tag{B.4}$$

With our Princeton Instruments spectrometer, the recorded signal is really photon counts per nanometer, with each pixel on the detector essentially serving as a bin, with wavelength resolution governed by the dispersion across the detector from the diffraction grating [10, 21, 54]. Due to conservation of energy, we know that [21, 28]:

$$f(E)dE = f(\lambda)d\lambda \tag{B.5}$$

However, Equation B.4 shows us that there is an inverse relation between energy and wavelength [28]. Given that the dispersion across our iCCD results in evenly spaced wavelength bins, when converted to units energy, these bins become un-evenly spaced, as evident from Figure B.2 [28]. The use of a Jacobian reconciles this discrepancy in binning, while also maintaining conservation of energy [28]. By combining Equations B.4 and B.5, we perform the chain rule to yield [28]:

$$f(E) = f(\lambda)\frac{d\lambda}{dE} = -f(\lambda)\frac{\hbar c}{E^2} \tag{B.6}$$

Therefore, to convert a wavelength spectrum to an energy spectrum, we must scale the photon counts by the Jacobian factor of -$\frac{\hbar c}{E^2}$ [28]. The inclusion of this Jacobian factor helps to preserve conservation of energy, despite the inverse relation between energy and wavelength bins [21, 28]. This conservation law is what tells us that the emissivities inferred from experimentally integrated wavelength spectra are able to be fairly compared to the emissivities inferred from integrated energy spectra simulated via PrismSPECT [21, 28].

B.3 Population models for emission spectroscopy

Line radiation primarily occurs due to excitation of particles from a meta-stable state (denoted q) to an excited level (denoted p), followed by de-excitation down to a level denoted k [10, 21, 54]. Upon de-excitation, a photon is emitted, whose energy is equivalent to E = $E_p - E_k$ [10, 21, 54]. The emissivity associated with this transition has the analytic form of: [54]

$$\epsilon_{pk} = n(p)A_{pk}\frac{\hbar c}{4\pi\lambda_0} \tag{B.7}$$

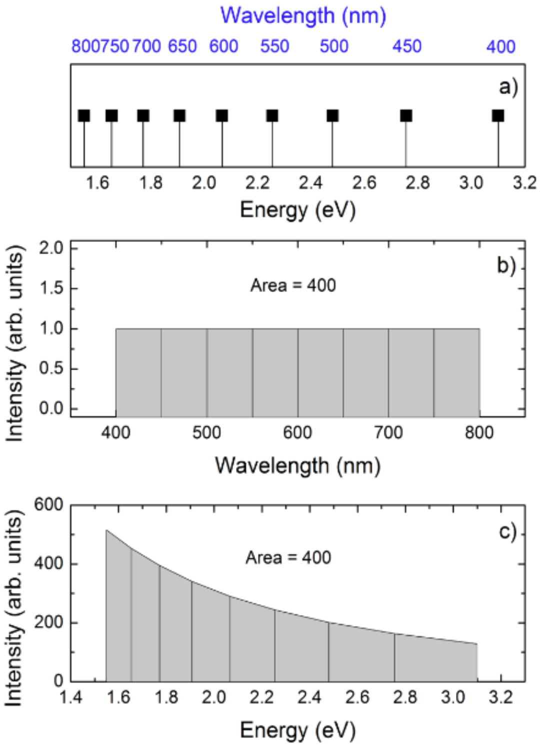

Figure B.2: Due to the reciprocal relationship between energy and wavelength, evenly spaced energy bins represent un-evenly spaced wavelength bins and vice-versa [28]. This highlights the need for a Jacobian factor when converting recorded photon counts between the two base units [28]. Figure reprinted with permission from Ref [28]: Jonathan Mooney and Patanjali Kambhampati. Get the basics right: Jacobian conversion of wavelength and energy scales for quantitative analysis of emission spectra, 2013. Copyright 2013 American Chemical Society.

Where n(p) is the population density of the excited state at the time of de-excitation [10, 21, 54]. This relation clearly shows that the brighter the line, the higher the excited state population density [10, 21, 54]. To make meaningful inferences of plasma parameters, population models must be employed to estimate the value of n(p), and relate it back to more fundamental plasma parameters such as electron density and plasma temperature [10, 21, 54]. This can be accomplished through the use of various population models [10, 21, 54]. The choice of each model depends on the plasma of interest.

B.3.1 Boltzmann distribution

This is the simplest population model, and assumes that our plasma is in thermal equilibrium [10, 21, 54]. In general, this condition is satisfied for higher electron densities, where high collision frequencies mediate thermal equilibration [21, 54]. When the excited states can be described by a Boltzmann distribution, the population densities can be uniquely determined by the temperature, T [10, 21, 54]. As the electron density decreases, less frequent collisions causes a deviation away from the Boltzmann regime [21, 54]. In this lower density regime, additional population models must be employed [10, 21, 54].

B.3.2 Rate coefficients and populating processes

When determining what population model to employ, it is imperative to understand which processes are dominant in the plasma of interest [10, 21, 54]. Associated with each process is a probability that must be considered [21, 54] . For spontaneous emission, this is best represented by the transition probability, A_{pk}, which is referenced in Equation B.7 [10, 21, 54]. When considering collisional processes, cross sections and coefficients come into play [21, 54].

The significance of a cross section can be understood by adopting the physical picture of a test beam of particles that are incident upon a grouping of stationary target particles [21]. The classical picture shown by Chen is presented in Figure B.3 [29, 33]. The cross here represents an effective area over which a collision is likely to occur [21, 33]. As a result, this also represents an effective probability for a collisional process [21, 33]. However, because particles in plasmas typically follow some velocity distribution function, the convolution of the test beam particle distribution function with the collisional cross section yields the effective rate coefficient for the collisional process of interest [10, 21, 33, 54]. These rate coefficients are of particular interest when describing non-equilibrium plasmas whose excited

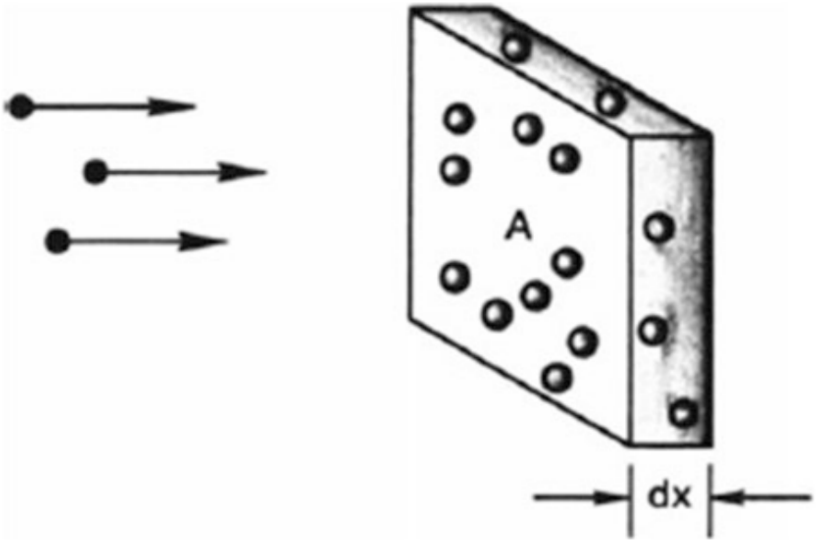

Figure B.3: Basic physics model from which cross sections are derived involve a set of beam particles incident on stationary target particles [29]. Image used with permission of Springer, from Ref. [29]: Francis F Chen. Introduction to plasma physics and controlled fusion. switzerland, 2016.; permission conveyed through Copyright Clearance Center, Inc.

states do not follow a Boltzmann distribution [10, 21, 54]. For electron impact processes, many codes and databases assume an isotropic Maxwellian distribution (such that there is no drift velocity) [18, 54]. This must be considered when querying rate coefficients from databases [18, 54]. In the case of our experiment, our electrons (in the post-shock material) may have some drift associated with them [15, 17]. However, the energy associated with this drift velocity is so small that the convolution region is effectively unchanged. Thus, we assume a Maxwellian EEDF when modeling electron impact effects in PrismSPECT.

B.3.3 Coronal equilibrium

In the case of very low electron densities, one can default to a coronal equilibrium which assumes low density but high temperatures (100s of eV), similar to that of the sun [21, 54]. The simplest coronal model balances electron impact excitation with spontaneous de-excitation, resulting in the following analytic form for emissivity [21, 54]:

$$\epsilon_{pk} = n_{g_z} n_e X^{exc}(T_e) \tag{B.8}$$

Where n_{g_z} is the ground state density associated with the emitting atom/ion of charge state $\bar{Z}$, and $X^{exc}(T_e)$ corresponds to the excitation emission rate coefficient [21, 54]. By neglecting additional populating and de-populating processes (such as electron impact de-excitation and self absorption), excited level population densities are orders of magnitudes less than that of the ground state density [54]. As a result, the ground state density in Equation B.8 can assumed equivalent to the overall atomic number density, providing a direct relation between line emissivity and atomic number density in the coronal model [54].

B.3.4 Collisional radiative modeling

The most general population model is the collisional radiative model, which essentially bridges the gap between the low density coronal regime, and high density Boltzmann regime [54]. The collisional radiative model balances collisional and radiative processs to evolve the excited state population density as a function of time [10, 21, 54]. This is all detailed in the following equation [10, 21, 54]:

$$\frac{dn(p)}{dt} = \Sigma_{k<p} n(k) n_e \chi_{kp}^{exc} - n(p)[n_e(\Sigma_{k<p}\chi_{pk}^{de-exc} + \Sigma_{k>p}\chi_{pk}^{exc} + S_p) + \Sigma_{k<p}A_{pk}] + \tag{B.9}$$

$$n(k)\Sigma_{k>p}(n_e\chi_{kp}^{de-exc} + A_{kp}) + n_i n_e(n_e\alpha_p + \beta_p) \tag{B.10}$$

The first term represents populating of the higher state due to electric impact excitation [54]. The bracketed second term details various loss mechanisms that can decrease the population of n(p) [54]. The third term accounts for populating procsses for n(p) that originate from higher energy states [54]. The final term represents recombination processes [54].

While this equation may seem intimidating, a tractable solution can be made given some guiding approximations [21, 54]. The first of which is assuming that the time derivative is ≈ 0 [21, 54]. This is often justified when considering that the relaxation times for atomic system are usually orders of magnitudes less than the time scales at which plasma parameters change [21, 54]. This approximation is reflected in our PrismSPECT simulations by selecting the steady-state option [18].

This steady-state approximation allows us to infer the analytic form for n(p) as a coupled linear equation of the form [54]:

$$n(p) = R_{g_z}(p) n_{g_z} n_e + R_i(p) n_i n_e \tag{B.11}$$

Here, the R terms are coupling coefficients, n_{gZ} is the ground state of the ion of interest, and n_i is associated with the next ionization stage [54]. By plugging this equation back into Equation B.7, we obtain the following form [54]:

$$\epsilon_{pk} = n_{g_z} n_e X^{eff}(T_e) \tag{B.12}$$

Where the coupling terms have been grouped together into the term X^{eff}, which represents the effective emission coefficient rate [54]. Simulations often show that for a variety of lines, these coefficients are primarily dependent on electron temperature [18, 54]. One important distinction between this formalism and the coronal equilibrium expression is that when using the collisional radiative model, we cannot assume that the ground state density is equivalent to the atomic number density of the emitting species [54], because as we move into CRM and Boltzmann regime, the excited state population density increases by many orders of magnitude [54].

B.3.5 Rate coefficients inferred via PrismSPECT

Assuming the quasi-static approximation with the collisional radiative model, our relation between line emissivity, ground state density and electron parameters is given as [54]:

$$\epsilon_{pk} = n_{g_z} n_e X^{eff}(T_e) \tag{B.13}$$

Where for a given T_e configuration, the relation between the ground state density of the emitting ion species of charge state Z and the total atomic number density of that ion species, n_z is given as [54]:

$$n_{g_z} = \frac{n_{g_z}}{n_z} n_z = A \times n_z \tag{B.14}$$

Where finally the ionization fraction, f, can be used to relate the number density of the ion species of charge state Z to the total number density of the species of interest (across all charge states), n_s [29]:

$$n_{g_z} = An_z = A \times f \times n_s \tag{B.15}$$

We can then plug this expression back into Equation B.16 [54] and group the terms A, f and X^{eff} into the following expression:

$$\epsilon_{pk} = n_s n_e X^{Pspect}(T_e) \tag{B.16}$$

Where $X^{Pspect} = X^{eff} \times f \times A$ is an equivalent CRM rate coefficient that we can query through PrismSPECT [18] simulations by providing simulated values of of density and temperature.

Queried values of X^{Pspect} are shown for Ar-II lines in Figure B.4 as a function of electron temperature with multiple curves plotted for varying values of total ion density, n_{tot_i}. It is important to emphasize here that total ion density corresponds to the total ion density of the system, such that $n_e = \bar{Z} n_{tot_i}$ [18, 33]. These figures show that X^{Pspect} is primarily sensitive to temperature, with its value over various orders of magnitude with increasing with T_e. It is important to note that the slope of increase for X^{Pspect} is quite steep at temperatures relevant to our experiment ($\approx$ 1.8 eV). It is also important to note that X^{Pspect} has a slight dependence on n_{tot_i}, especially for singly ionized lines such a N-II and Ar-II. For example, with argon, we see that X^{Pspect} tends to decrease with increasing n_{tot_i}. A possible reasoning for this is hinted at in Ref. [54], where we see that after a certain density value, the excited state populations for hydrogen tend to level out, a trend that could also feasibly occur in argon. Because emissivity is also proportional to n(p) [54] (See above), this would mean that at the stagnation point of n(p), changes in density would be greater than changes in emissivity, leading to a lower X^{Pspect} at higher densities as shown below. It is also important to note that X_{Pspect} is relatively insensitive to changes in plasma composition, as shown below in Figure B.7. This is likely because electron-impact effects are the dominant collisional process [54], and across the possible permutations of composition relative to our experiment, $\bar{Z}$ and consequently n_e are both relatively unchanged. By using this equivalent form of the CRM rate coefficient alongside Equation B.16, variations in line emissivity can be directly tied back to variations in atomic number density of the emitting species, n_s. This formalism is used for interpreting line emissivity measurements in Chapter 4

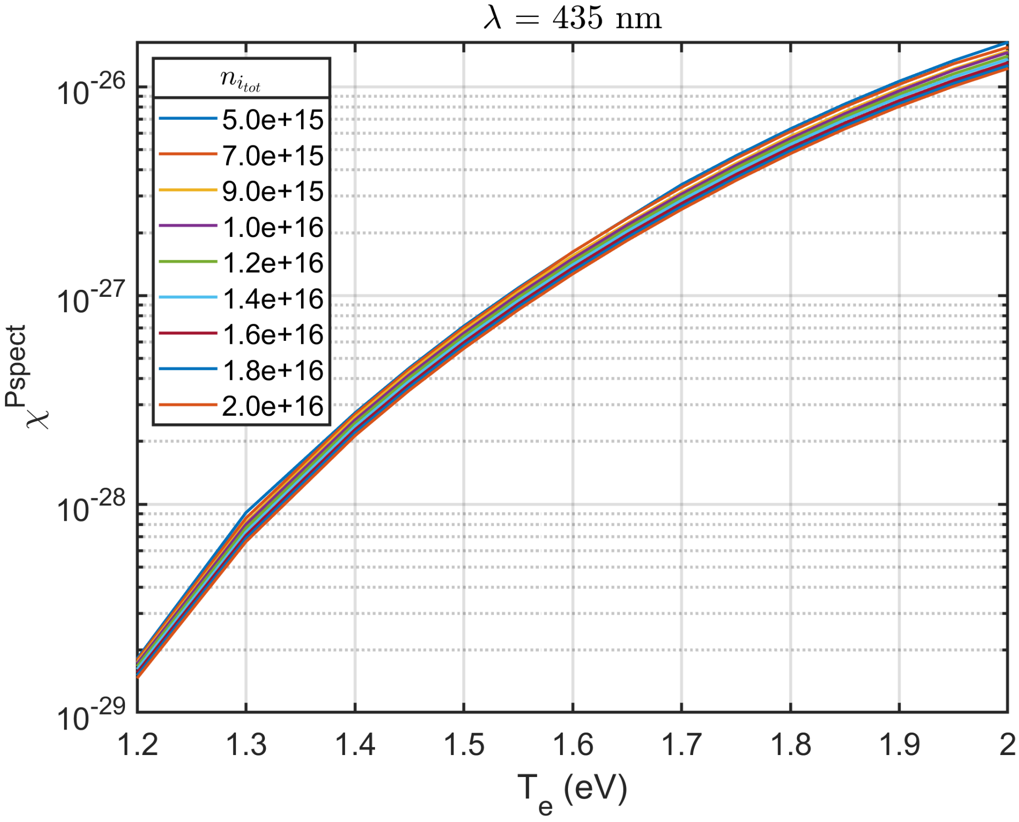

Figure B.4: Equivalent CRM rate coefficients tabulated for Ar-II (435 nm) using PrismSPECT. These rate coefficients are primarily sensitive to changes in temperature, but also has a noticeable dependence on total ion density as well. This rate coefficient was simulated assuming a plasma composition that is 50 % gas (referred to as 50 WG) supplied to the railgun (which is 90 % Ar, 10 % N_2.)

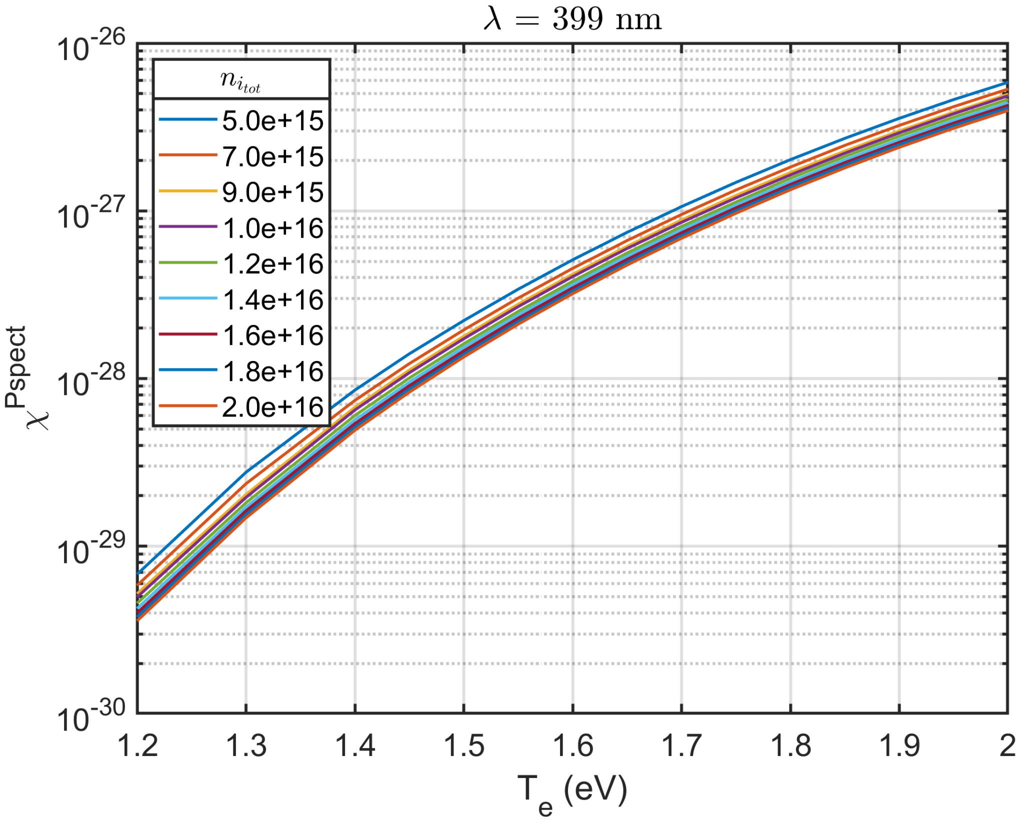

Figure B.5: Equivalent CRM rate coefficients tabulated by PrismSPECT for N-II (399 nm) using the 50 WG composition described in Figure B.4. Like Ar-II, this rate coefficient is primarily dependent on temperature with a slight density dependence

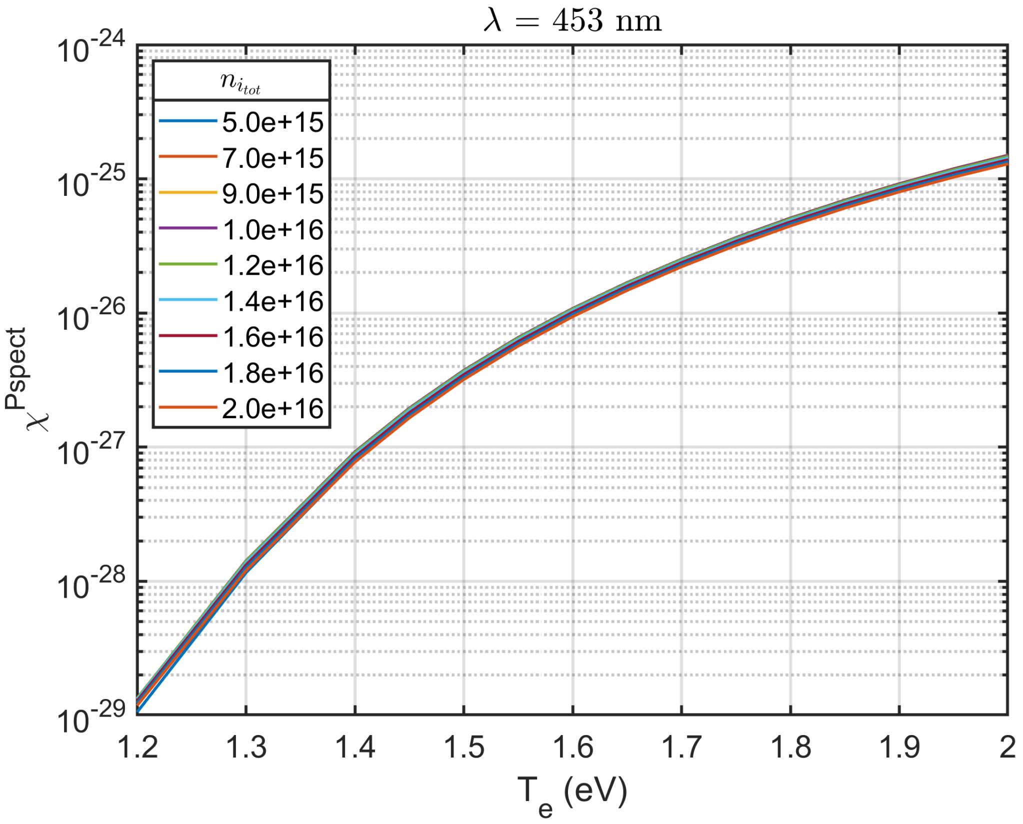

Figure B.6: Equivalent CRM rate coefficients tabulated by PrismSPECT for Al-III (453 nm). These rate coefficients are primarily sensitive to changes in temperature, but also has a noticeable dependence on total ion density, though this is not as drastic as it is in the singly ionized elements.

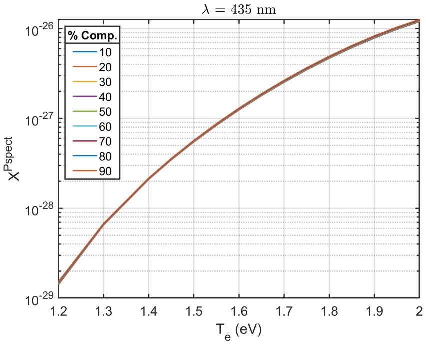

(a) Equivalent Ar-II (435 nm) rate coefficients for jets of 10 % purity (.9Ar + .1N_2) through 90 % purity. These traces represent a total ion density of 2E16 cm^{-3}, but these trends are consistent across all densities relevant to the the experiments in Ch. 4).

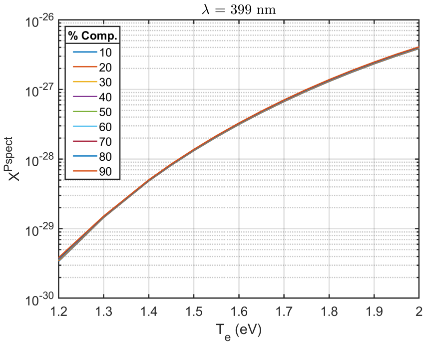

(b) Equivalent N-II (399 nm) rate coefficients for jets of 10 % purity (.9Ar + .1N_2) through 90 % purity. These traces represent a total ion density of 2E16 cm^{-3}, but these trends are consistent across all densities relevant to the the experiments in Ch. 4).

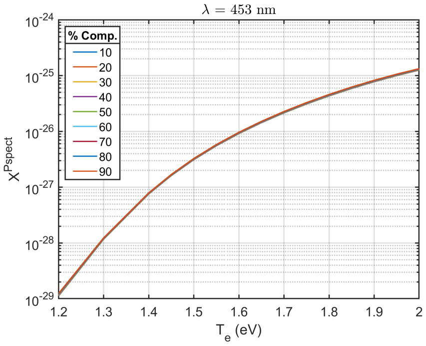

(c) Equivalent Al-III (453 nm) rate coefficients for jets of 10 % purity (.9Ar + .1N_2) through 90 % purity. These traces represent a total ion density of 2E16 cm^{-3}, but these trends are consistent across all densities relevant to the the experiments in Ch. 4).

Figure B.7: PrismSPECT queried equivalent rate coefficients are generally insensitive to changes in plasma jet composition with a relative percent difference of ≈ 1 % in χ^{Pspect} across a 10% change in jet purity. This independence from composition allows us to confidently infer trends in χ^{Pspect} in Ch. 4.

Appendix C

Standard operating procedures

C.1 Telescope design

The general layout for the telescope design is presented in Figure C.1. This design can be easily adapted to achieve varying spatial resolutions with the ThorLabs fiber bundle that is attached to the end of the apparatus. The defining feature of this design is the use of a pinhole that is positioned exactly at the focal distance from the lens, which ensures that only collimated light passes through the telescope array and is projected onto the fiber bundle. This is especially important, because while light emitted from a point source will diverge as a function of distance, collimated light does not. This ensures that the spectrometer will measure the same signal from a light source irrespective of distance from the objective lens. This invariance of signal as a function of distance is crucial to the Abel-inversion process [26], otherwise a weighting function will have to be applied to the system of linear equations that are solve during the inversion process.

C.2 Spectrometer setup

Setup of the interferometer diagnostic is well documented in Ref. [1]. For the spectrometer, details regarding setup and characterization will be provided below. To align the telescope with the desired viewing location, the author uses a Newport pencil style calibration

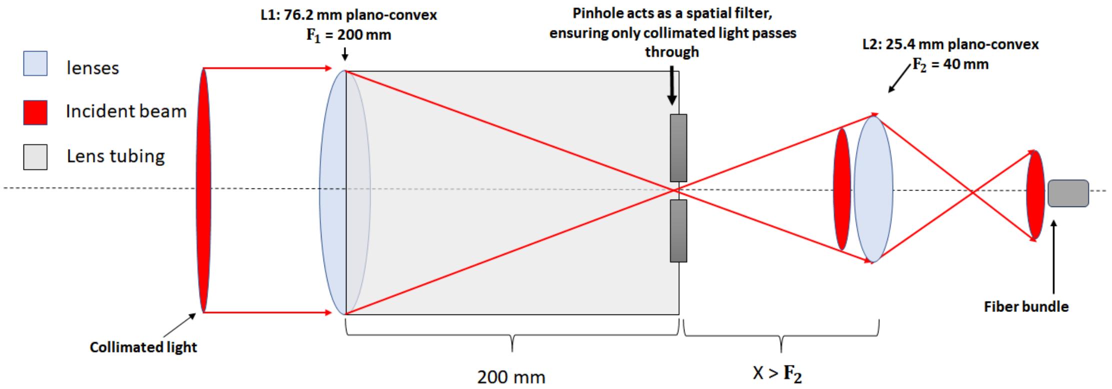

Figure C.1: The telescope used throughout these two campaigns project collimated light onto the linear fiber bundle to obtain spatially resolved spectrograms. An objective lens with a focal length of 200 mm is used, with a pinhole placed at exactly one focal distance away from the lens. This arrangement accepts only collimated light incident on the objective lens, preserving spatial resolution, as well as ensuring that the recorded signals can be confidently Abel-inverted [26]. The remaining components include a 40 mm plano-convex lens as well as the fiber bundle. The distance between this lens and the pinhole can be tuned to minimize the incident spot size, while preserving all the relevant spatial information obtained via the objective lens. The size of this projected spot size relative to the size of the fiber bundle determine the spatial resolution of the each fiber. With the exception of the distance between the pinhole and objective lens, all other distances between optical components can be varied depending on the needs of the experiment.

lamp [8, 59]. By placing this lamp at the desired z-axis viewing location, the telescope can confidently aligned by mounting it in a manner that maximizes the throughput to the fiber optic bundle. This can be determined in real-time by using the live-view feature associated with the spectrometer software. An example is displayed in Figure C.2.

Because the telescope projects light onto a linear fiber bundle, it is imperative to know the precise location of each fiber in the array. This is done through the use of an 8x8 LED array [8]. With the telescope mounted, the LED is placed at the height of the bore-sight axis of the chamber, and translated along the z-axis with the use of a micron-precision translation stage. By covering all LEDs on the array except for one, this single LED can be used to illuminate each fiber in the bundle. This is done by translating the LED through each fiber,

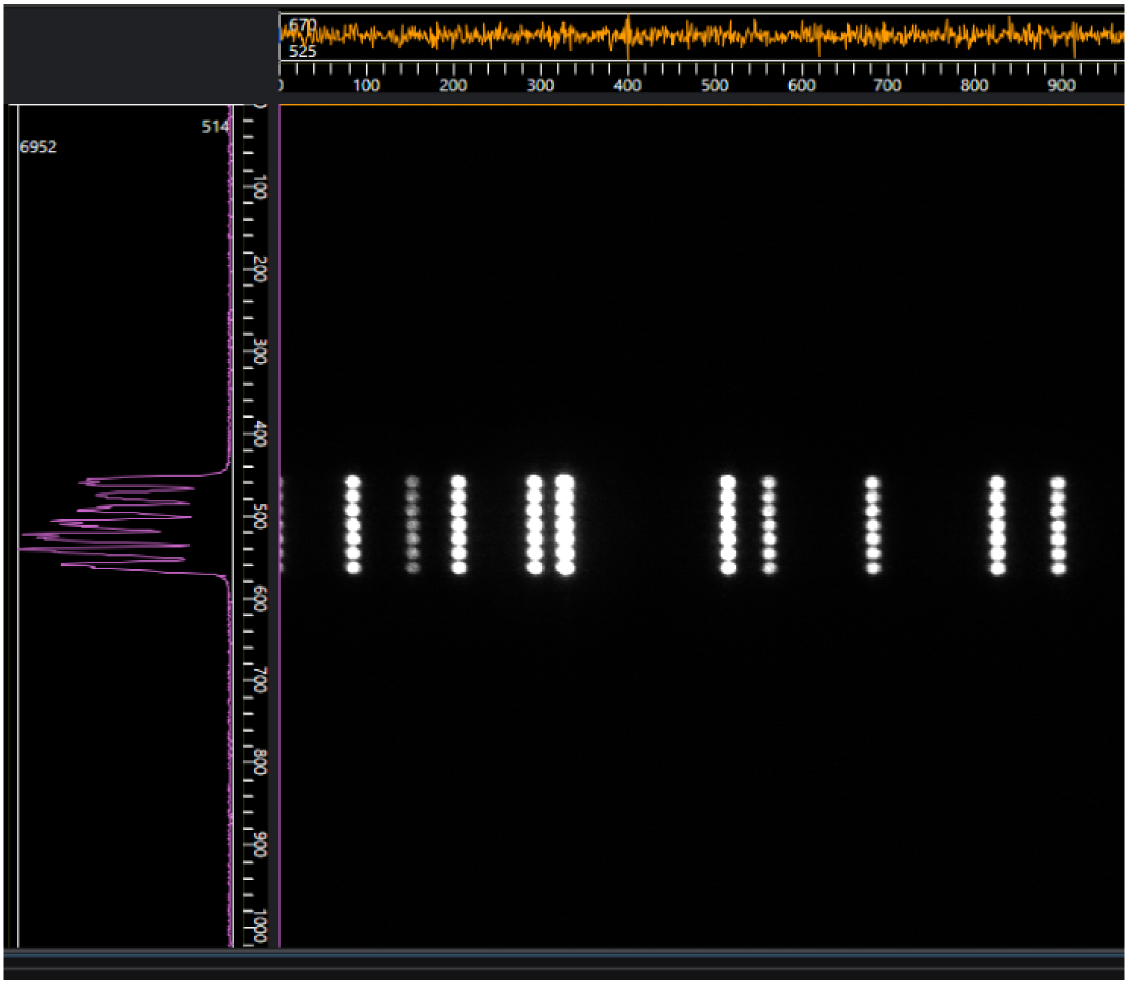

Figure C.2: Raw spectrogram output from the neon lamp. The live view tab on the left-hand side is used to monitor throughput to the detector. Telescope is considered aligned with respect to the neon lamp when this signal is maximized throughout each fiber.

and stopping at the location at which the throughput to that fiber is maximized. With the use of the micrometer measurements on the translation stage, the fiber-to-fiber distance, and fiber-z-axis location can be inferred from this procedure. An example of this analysis is displayed in Figure C.3.

In addition to mapping the viewing chords of all fibers, the last campaign has highlighted a need to quantify the intensity captured in each fiber relative to one another. This is done at the same time as the spatial mapping done above. As each fiber is illuminated by the single

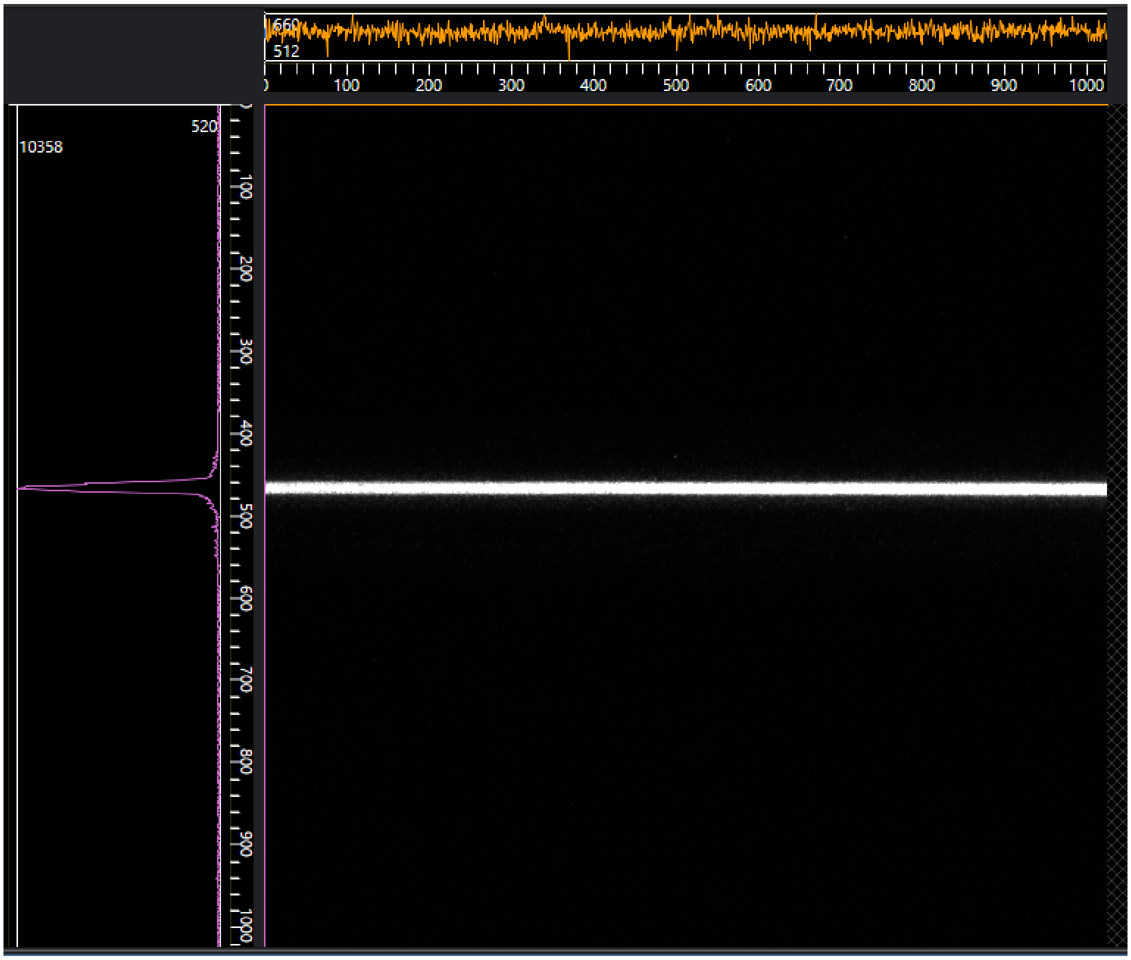

Figure C.3: Raw spectrogram output from the LED as it is incident on a single fiber. Once again, the live view tab on the left-hand side is used to monitor throughput to the detector as the LED is translated from fiber to fiber. LED is considered aligned with respect to viewing chord of a fiber when this signal is maximized.

LED, the wavelength-integrated intensity is recorded and compared to all other fibers. This allows for the determination of a sensitivity factor that can be applied to each measurement to ensure that when the fiber is illuminated by the exact same LED, the measured signal is exactly the same.

It is essential to note that for the results presented in Section 4, the collection optics and fiber bundle are suspended on top the vacuum chamber by an 80/20 support mount. Prior to each day of testing, the collection optics are translated to the necessary location, and coarse check of alignment is performed with a level that confirms the telescope is level with the chamber, and re-aligning with the z-axis as necessary by measuring the location of peak emissivity from the single LED as it is translated along the chamber. This constant re-alignment process implies that the optical setup is subtly different from day to day, and therefore the relative intensity calibration derived on one day cannot be assumed or simply extracted for subsequent days. As it turns out, this fluctuation in fiber-to-fiber sensitivity can be quite significant, with two independent setups from two different days probing the same axial location, and clearing the same coarse alignment checks having relative sensitivity factors that can vary by as much as 10 to 30 percent. One possible contributor to this drift is attenuation within the fiber as a result in subtle changes in launching conditions into the fiber and bending radius of the fiber at the top of the telescope as it travels from the top of the chamber down towards the spectrometer entrance slit [60]. In instances such as this, a calibration routine that is not properly controlled for risks invalidating our data and interpretation of the results. [61]. This is especially true in constrained experimental setups such as this, where the viewing chord of maximum emissivity may only be ≈ 10 % greater than in adjacent viewing chords. In response, for axial emissivity profiles in Chapter 4, intensity calibration for all relevant shot sets were performed immediately before or after data collection, as not doing so would have produced calibration measurements without sufficient control, and therefore unreliable measurements. [61]

C.3 Creating a vacuum environment

With the exception of atmospheric pressure plasmas, plasmas require a vacuum environment to exist in. In atmosphere, the surrounding air facilitates recombination, effectively acting as a sink for electron and ion densities [33]. The cylindrical chamber mentioned above is the vessel that is pumped down to maintain a vacuum environment sufficient for operating the experiment. Maintaining a vacuum in part relies on ensuring that the vessel and all interfaces between the interior and exterior are free of oils and debris. This can be accomplished by cleaning the flanges and gaskets that are affixed to the chamber.

When pumping a vessel down from atmospheric pressure ($\approx$ 760 mTorr) to a high vacuum, the behavior of the enclosed gas transitions from viscous flow, dominated by inter-molecular collisions, to molecular flow, dominated by random particle motion [62]. Because different vacuum pumps are designed for different flow regimes, obtaining a vacuum environment requires at least two different pumps used in coordination with one another [62]. At the EPPL, we employ a rotary vane roughing pump do obtain a rough vacuum, and a cryopump [62] to further transition to a moderate to high vacuum. The roughing pump is by default isolated from the chamber by a roughing valve, while the cryopump is isolated from the chamber by a pneumatic actuated gate valve. Assuming this default configuration at amospheric pressure, the pump down process is initiated by turning on the rough pump, opening the roughing valve, and the opening the gate valve. The gate valve is opened so that in addition to roughing down the chamber, the rotary pump will pump down the baffles for the cryopump. Once the chamber is at 50 $\approx$ mTorr, all isolation valves are closed and the rough pump is turned off. Once it is certain that both the gate valve and roughing valves are closed, it is appropriate to turn on the cryopump. At this point in time, the active surfaces of the cryopump are cooled from 300 K to 20 K, a process that takes $\approx$ 3 hours. Because no pumps are on during this cool-down time, it is natural for the chamber to slowly leak up from 50 mTorr. If this is the case, it is important that the rough pump is employed to return the vessel pressure to 50 mTorr before opening the gate valve to expose the cryo to the chamber. Once the chamber is at 50 mTorr and the cryopump has cooled to 20 K, the roughing pump is turned off, the isolation valve is closed, and the gate valve is opened.

As the cryopump is exposed to the chamber, the particles that pass through the pumping surfaces are supercooled and adsorb to the cryo surface, evacuating the chamber [62]. Once the pressure has dropped into the nTorr range, then the experiment can be run. Throughout this procedure it is important to note that while both pumps can be turned on at the same time, the cryo gate valve should never be opened while both the cryo and rough pumps are on. If this occurs, then oil from the rotary vane pump could backstream through the chamber, contaminating the chamber.

C.4 Running the railgun experiment

With the exception of the spectrometer, the railgun and associated diagnostics are operated through a LabVIEW GUI in a manner similar to the work carried out in Ref. [17], [15] and [8]. LabVIEW commands are mediated through fiber-optic signals to “charge” and “dump” accumulated charge on the capacitor bank/PFN system via mechanical relays which ensure that the connection between the PFN and power supply is floating during each shot, and grounded immediately after. The GUI also interfaces with the PXIe (See Ch. 2), which acts as the DAQ for the Rogowski Coil and interferometer chords.

The figure below (See Figure C.4) shows the GUI reponsible for running the experiment. In practice, two people must be present to run the experiment. One is responsible for operating the high voltage supply, the other operates LabVIEW. Both are responsible for maintaining safety standards are being met throughout the testing time. Prior to a single shot, the data acquisition units must be armed for collection. This is achieved by clicking the “Start DAQ” and “PXIe Data Acquisition Armed” buttons on the GUI, which will then stay armed for the entirety of the shot. To begin the shot sequence, the charge and dump buttons are engaged on the LabVIEW GUI. This connects the high voltage power supply to the PFN, while disconnecting the PFN from ground, such that it is essentially floating. Initially, the users will observe a current being drawn from the power supply, which is an artifact of the charging of the capacitor bank, where $I = C\frac{dV}{dT}$ [62]. As PFN charges to its desired voltage, the current eventually tends to zero. We consider the PFN as fully charged when the multimeter across the PFN measures the nominal voltage while the power supply is supplying a current $<$ .06 mA. Once these conditions are met, the charging relay is "opened" such that the power supply is disconnected from the PFN. At this point in time, the bank is still considered floating from ground. Once the charge relay is opened, the high voltage output on the power supply is turned off, at which point the "Fire" button on the GUI is engaged. This button controls a delay generator which then sends out precisely timed triggers to different aspects of the experiment. One of these triggers is sent to a spark gap switch that when triggered, allows the PFN to discharge across the railgun, completing the discharge cycle. At the end of the shot, the "PXI Data Acquisition Armed" button automatically disarms itself, indicating that data has been acquired through the PXIe. Once the shot has successfully occurred, the dump relay is engaged which dumps any remaining charge remaining on the PFN back to ground. From here, the shot process repeats itself as necessary.

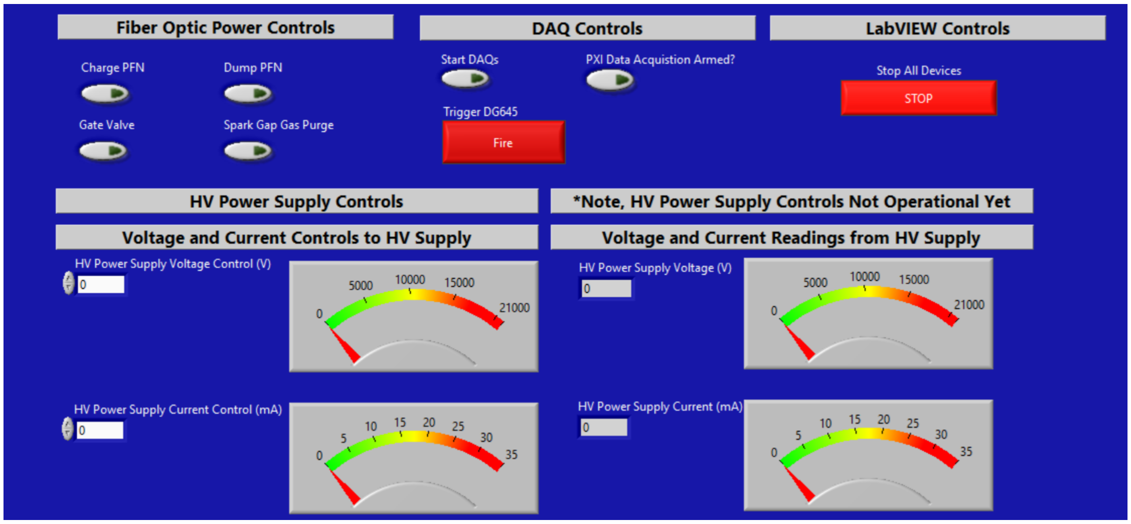

Figure C.4: Screenshot of LabVIEW GUI utilized for the railgun experiment. This tab depicts all the buttons necessary for successfully completing a shot with the experiment.

Appendix D

MATLAB analysis codes

D.1 Matrix Abel inversion for interferometer data

```
function [ne,sigma_ne_1,L] = Gnskn_Abel_Inversion_Final(y,dy,Avg_y0,Mapping,stdev)
%% Gnskn Abel Inversion
% Written by: Ameer Mohammed
% Kevin T. Crofton Department of Aerospace Engineering

%% Overview
% This code computes an abel inversion to determine the radial
% density distribution using the matrix Abel inversion tecnique. Radial
% zone disribution is consistent with the model employed by Gornushkin et
% al.

%% User inputs
% y = []; These are chord locations relative to the center of the cross
% sectional area of the cylinder (typically units of cm). This includes any
% boundary conditions

% dy = []; Distance between adjacent radial zones. Units of cm. One element
% of dy per element of y. Represents the distance from the sightline to the
% end of the corresponding radial zone in one qaudrant of the plasma
% column.

% Avg_y0 = ; Average nel measured at the y = 0 station. T
% Mapping = []; Derived from radial model. Includes any boundary conditions

%stdev = [];
% Standard deviation for error propagation. Should be same length as
```

```
% y

% Mapping = [];

%% Code Outputs
% This code outputs the radial density distirbution for the component of
% interest, as well as the propagated uncertainty for the on-axis value.

%% Code:

C =9.7874E+14;
% Constant used to convert from phase shift to ne
phi = (Avg_y0*Mapping)./C; % Averaged phase shift recorded at each sightline
% [Units Degrees]

% sanity check
if length(phi) ~= length(phi)
    return
end
% if length phi is not equal to length of y, end and double check inputs.
imax = length(y); % i corresponds to the sightline
jmax = length(y); % j corresponds to the radial zone

% Creating the length matrix
for ii = 1:imax

    for jj = 1:jmax
        if ii > jj
            L(ii,jj) = 0;
        elseif jj > ii
            L(ii,jj) = sqrt( ((y(jj) + dy(jj))^2) - (y(ii)^2) ) - sqrt( (y(jj)^2) - (y(ii)^2));
        elseif jj == ii
            L(ii,jj) = sqrt( ((y(jj) + dy(jj))^2) - (y(jj)^2));
        end

    end

end

```

```
% Inverting the length matrix
InvL = inv(L);

% Performing the abel inversion
for jj = 1:jmax
    for ii = 1:imax
    term(ii) = InvL(jj,ii)*phi(ii)
    end
    ne(jj) = (C/2)*sum(term)
end

% Caculating error in the y = 0 components
for ll = 1:length(y)
    if ll == 1 % if looking at the first propagated term
        for mm = 1:length(y)
            First_term_sub_term(mm) = (C/2)*InvL(1,mm)*(Mapping(mm)/C);
        end
        Error_term(ll) = ( (sum(First_term_sub_term))^2 ) * (stdev(ll)^2);
    else
        Error_term(ll) = ((C/2) * InvL(1,ll) * (Avg_y0 / C) * stdev(ll))^2;
    end
end

sigma_ne_1 = sqrt(sum(Error_term));
```

D.2 Wavelength space spectral line fits

```
function [P_Fit_WLfit,conf_WLfit,fun_WL_Fit] = Voigt_WL_Fitting_Func(L,LineMatNorm,
    Wavelength_Sample,Gwidth,Lwidth)

%% Voigt WL Fitting Function
% Written by: Ameer Mohammed
% Kevin T. Crofton Department of Aerospace Engineering

%% Overview
% This function performs wavelength space fitting of inputted specrtal line
```

```
% to infer optimized effective Gaussian and Lorentzian widths and
% associated confidence intervals. To accomplish this, a local curve
% fitting routine is run in parallel with a global optimization scheme to
% reduce the effects of intial guesses on the converged solutions.

%% User Inputs:

% L: Matrix of initial guess parameters.
% Format for L is [Centroid, Lorentzian FWHM, Gaussian FWHM,amplitude];
% This is the format in which optimized parameters will be reported as
% well.

% LineMatNorm: Input specral line

% Wavelength_Sample: Wavelength vector

% Gwidth & Lwidth: Experimentally inferred instrument function widths.

%% User Outputs:

% This function returns optimized fitting parameters and associated
% confidence intervals.

%% Code

LB = [-Inf,Lwidth,Gwidth,0];
UB = [Inf,.9,.9,Inf];
% Optimized Gaussian and Lorentzian FWHMs cannot be less than the
% instrument functions.

% Fitting data in WL space and comparing the quality of fit.
fun_WL_Fit = @(L,WLS) L(4)* ((convn(  (exp( (-4 * log(2) .* ((WLS - L(1)).^2) ) ./ (L(3).^2) )) , ((L(2).^2) ./ ( (4.* ((WLS - L(1)).^2)) + (L(2).^2)) ),'same')) * round( abs(WLS(2) -WLS(1)),4) );
[P_Fit_WLfit,resnorm_WLfit,residual_WLfit,exitflag_WLfit,output_WLfit,lambda_WLfit,J_WLfit] = lsqcurvefit(fun_WL_Fit,L,Wavelength_Sample,LineMatNorm,LB,UB)

% Multi-Start for the lambda fit
global_check = -3; % makrer used to confirm when the minimum process is being run.
```

```
while global_check <= 0
    % lsqcurve fit is good for finding local minimums of the sum of residuals
    % to ensure that the parameters used in this fit is in fact a global sum,
    % MultiStart is run in parallel to lsqcurvefit to ensure this
    problem1 = createOptimProblem('lsqcurvefit','x0',L,'objective',fun_WL_Fit,...
    'lb',LB,'ub',UB,'xdata',Wavelength_Sample,'ydata',LineMatNorm);

    ms1 = MultiStart('PlotFcns',@gsplotbestf);
    [xmulti1,errormulti1] = run(ms1,problem1,50) % This runs the global solver over 50 instances
        to determine the global minimum

    if abs(xmulti1 - P_Fit_WLfit) < 1E-4 % If local and global fit converge
        yfit_WLfit = fun_WL_Fit(P_Fit_WLfit,Wavelength_Sample);
        conf_WLfit = nlparci(P_Fit_WLfit,residual_WLfit,'jacobian',J_WLfit);
        % Compute confidence intervals
        global_check = 1; % Exit condition for loop
    else % If convergence is not achieved
        [P_Fit_WLfit,resnorm_WLfit,residual_WLfit,exitflag_WLfit,output_WLfit,lambda_WLfit,
            J_WLfit] = lsqcurvefit(fun_WL_Fit,xmulti1,Wavelength_Sample,LineMatNorm,LB,UB)
        fit_WLfit = fun_WL_Fit(P_Fit_WLfit,Wavelength_Sample);
        conf_WLfit = nlparci(P_Fit_WLfit,residual_WLfit,'jacobian',J_WLfit);
        global_check = global_check+1;
        % Re-run fit, re-compute uncertainties

        if abs(xmulti1 - P_Fit_WLfit) < 1E-4
            global_check = 1;
            % If re-fitted parameters converge, supply exit condition for
            % loop. Else, loop repeats.
        end
    end
end
end
```

D.3 FFT spectral line fits

```matlab
function [I_fft,k,P_Fit_FFT,conf_FFT,lambda0_FFT,FFT_lambda_Conf,Recvonvolved_Function] = Voigt_FFT_Fitting_Func(P,LineMatNorm,Wavelength_Sample,centerbin,pixelbin,Gwidth_Inst,Lwidth_Inst,lambda0)

%% Voigt FFT Fitting Function
% Written by: Ameer Mohammed
% Kevin T. Crofton Department of Aerospace Engineering

%% Overview:
% Given a spectral line, this code fits a Voigt profile in FFT space,
% reporting the optimzied effective Gaussian and Lorenztian widths.

%% Inputs:
% P: Initial guess vector for local fit. Structure of
% [Lorentzian FWHM, FFT Amplitude, Gaussian FWHM]

% LineMatNorm: Spectral line to be fitted

% Wavelength Sample: Wavelength vector

% Centerbin: Center element number of LineMatNorm (assumed total length is
% odd)

% pixelbin: (length(LineMatNorm)-1)/2. Used to construct wavenumber array

% GWidth_Inst & LWidth_Inst: Instrument Function FWHMs

% lambda0: Initial guess line centroid

%% Outputs:
% Optimized effective Gaussian and Lorentzian lengths alongside confidence
% intervals assocaited with final fit.

%% Code

% Computing the FFT
I_fft = fftshift(abs((fft(LineMatNorm)))); % This plots the magnitude of the fourier coefficients (since they are complex)
% fft shift re-arranges the transform so that the zero wavenumber is in the
```

```
% center, with the negative and positive wavenumbers on the left and right
% respectively.

LB = [Lwidth_Inst,0,Gwidth_Inst];
UB = [Inf,Inf,Inf];

% Determining wavenumber
k(centerbin) = 0; % This is the center point where wavenumber is zero
k_spacing = (2*pi()) / ( round((Wavelength_Sample(2) - Wavelength_Sample(1)),4) * length(I_fft) ) ;
% Source: Fox -> Waves and Oscillations Textbook.

for ii = 1:pixelbin % This assumes the sample size of the input line is odd
    k(centerbin + ii) = ii * k_spacing;
    k(centerbin - ii) = -ii * k_spacing;

    % When the sample size is odd, then the FFT argument returns the
    % two-sided spectrum (zero wavenumber, positive wavenumbers and mirrored
    % negative wavenumbers) and no nyquist frequency component.
end

% Fitting spectral profile in the FFT domain
options = optimset ('MaxFunEvals' ,1E7 , 'MaxIter' ,1E7,'Algorithm','levenberg-marquardt' );

% order of parameters in matrix: [lwidth,amplitude,gwidth]
fun = @(Pvar,kvar) Pvar(2)*exp(  ( -( ((Pvar(3).^2) * (kvar.^2)) ./ (16.*log(2)) ) ) - ( ((Pvar(1)).*abs(kvar)) ./ 2) )

% Local fitting call
[P_Fit_FFT,resnorm_FFT,residual_FFT,exitflag_FFT,output_FFT,lambda_FFT,J_FFT] = lsqcurvefit(fun,P,k,I_fft,LB,UB,options);

% Running a global fit using multi-start to ensure a global minimum is being found
global_check = 0; % makrer used to confirm when the minimum process is being run.
while global_check == 0

    % lsqcurve fit is good for finding local minimums of the sum of residuals
    % to ensure that the parameters used in this fit is in fact a global sum,
    % MultiStart is run in parallel to lsqcurvefit to ensure this
```

```
    problem1 = createOptimProblem('lsqcurvefit','x0',P,'objective',fun,...
    'lb',LB,'ub',UB,'xdata',k,'ydata',I_fft);

    ms1 = MultiStart('PlotFcns',@gsplotbestf);
    [xmulti,errormulti] = run(ms1,problem1,50) % This runs the global solver over 50 instances to determine the global minimum

    if abs(xmulti - P_Fit_FFT) < 1E-4
        conf_FFT = nlparci(P_Fit_FFT,residual_FFT,'jacobian',J_FFT); % If both routines return the same parameters, compute the confidence interval. If not
        % re-run the lsqcurvefit with the xmulti output as an initial
        % guesss to obtain the proper Jacobian
        global_check = 1;
    else
        [P_Fit_FFT,resnorm_FFT,residual_FFT,exitflag_FFT,output_FFT,lambda_FFT,J_FFT] = lsqcurvefit(fun,xmulti,k,I_fft,LB,UB,options);
        conf_FFT = nlparci(P_Fit_FFT,residual_FFT,'jacobian',J_FFT);
    if abs(xmulti - P_Fit_FFT) < 1E-4
        global_check = 1; % If that second time did the trick, then it exits the while loop.
    end
        % The way this is re-initialized basically clears the slate of the
        % previous curve fitting routine.
    end
end

% Re-convolving fit in wavelength space.

% Initial guess voigt parameters to be optimized
 L = [lambda0,100];

 % Fitting a Voigt profile centroid and amplitude in lambda-space, using
 % the FFT optimized parameters
Recvonvolved_Function = @(L,WLS) L(2)* ((convn(  (exp( (-4 * log(2) .* ((WLS - L(1)).^2) ) ./ (P_Fit_FFT(3).^2) )) , ((P_Fit_FFT(1).^2) ./ ( (4.* ((WLS - L(1)).^2)) + (P_Fit_FFT(1).^2)) ), 'same')) * round( abs(WLS(2) -WLS(1)),4) );
[lambda0_FFT,resnorm_reconvolved,residual_reconvolved,exitflag_reconvolved,output_reconvolved,lambda_reconvolved,J_reconvolved] = lsqcurvefit(Recvonvolved_Function,L,Wavelength_Sample,LineMatNorm)

```

```
% Multi-Start for the lambda fit parameters
global_check = 1; % makrer used to confirm when the minimum process is being run.
while global_check == 1
    % lsqcurve fit is good for finding local minimums of the sum of residuals
    % to ensure that the parameters used in this fit is in fact a global sum,
    % MultiStart is run in parallel to lsqcurvefit to ensure this
problem2 = createOptimProblem('lsqcurvefit','x0',L,'objective',Recvonvolved_Function,...
    'lb',[-Inf,0],'ub',[Inf,Inf],'xdata',Wavelength_Sample,'ydata',LineMatNorm);
ms2 = MultiStart('PlotFcns',@gsplotbestf);
[xmulti2,errormulti2] = run(ms2,problem2,50) % This runs the global solver over 50 instances to determine the global minimum
    if abs(xmulti2 - lambda0_FFT)<1E-4
        FFT_lambda_Conf = nlparci(lambda0_FFT,residual_reconvolved,'jacobian',J_reconvolved);
       % Compute confidence intervals
        global_check = 2; % If convergence is achieved, supply exit condition
    else
        [lambda0_FFT,resnorm_reconvolved,residual_reconvolved,exitflag_reconvolved,output_reconvolved,lambda_reconvolved,J_reconvolved] = lsqcurvefit(Recvonvolved_Function,xmulti2,Wavelength_Sample,LineMatNorm)
        FFT_lambda_Conf = nlparci(lambda0_FFT,residual_reconvolved,'jacobian',J_reconvolved);
         % re-run fit, re-compute uncertainties
        if abs(xmulti2 - lambda0_FFT)<1E-4
            global_check = 2;
            % If re-fitted parameters converge, supply exit condition for
            % loop. Else, loop repeats.
        end
    end
end
```

D.4 Spectrometer background averaging

```
function [Grating] = Spectrometer_BG_Averaging_September_2023(Shots,BG_no,filepath,filepath_save)

%% BG Averaging code:
    % Written by Ameer Mohammed March 2022
    % Updated for analysis June 2022
```

```
%% Code Overview:
    % This code is developed for the 2022 Shock campaign, to average over large
    % number of BG shots. For the previous camapgin, one BG shot was taken to
    % essentially detrend the experimental intensity data. This method was
    % sufficient for larger exposure times, where SNR was good. For gate times
    % ~ 10s of ns, it is important to limit the amount of noise present in
    % experimental data. Because a BG shot has its own independent noise
    % contribution, while it can detrend the data, it can also and noise back
    % into the BG-subbed data. This code attempts to generate a cleaner BG by
    % averaging over a large amount of data. This should cause the random noise
    % to average out to zero.

%% Code inputs
    % Shots (string or double): This specifies the shot of interest to be processed. If the
    % shot to be processed is an energized railgun shot (for ex: shot 2540),
    % then this is simply an entry or array of shot numbers. If this is the
    % background data for the LED calibration trials, then this entry is a
    % string that specifies the base name of that background file.

    % BG_no (double):  Number of background shots taken per shot. Presently, this must be
    % constant for the shots specified as input

    % filepath (string): This is the path name of the background data to be
    % processed. All raw BG data is in the form of csv files with first
    % column representing WL, second: Intensity, third: PiMax row

    % filepath_save (string): This is the path name where the output file will
    % reside.

%% Code outputs:
    % Avg_Reshaped_BG (matrix): This is a 1024x1024 matrix of averaged
    % intensity values which can be used in future codes to perform line
    % outs and detrend data.

%% Log:
    % 1) Last edits made before using in first pass of processing on 11.9.2022 @ 5:41 PM

    % 2) 3.16.2023 @ 5:51 pm: Added functionality for LED calibratoin BG files as well.

```

```
%% Code:
for jj = 1:length(Shots) % Iterate over shots.
    Shot_val = Shots(jj);
    Summed_matrix = []; % initializes summed matrix
    Subtractor = 0;

    for ii = 1:BG_no  % Iterates through all the BG shot files (csv)
        if isa(Shots,'string') == 1 % if shot inputs are string (like on/off
            % axis BG for calibrations
            String = sprintf('%s/%s_%d.csv',filepath,Shot_val,ii);
            % Base file name for LED BG shots
        else % if averaging BG for energized shots
            String = sprintf('%s/pimax%d_BG_%d.csv',filepath,Shot_val,ii);
            % Base file name for railgun BG shots
        end
        if isfile(String) == 1 % if file exists, load and perform summing
            % If not, move onto next iteration of loop
            BG_dat = csvread([String]);
            BG_Int = reshape(BG_dat(:,2),[1024 1024]); % Reshapes intensity into
            WL_mat = reshape(BG_dat(:,1),[1024 1024]); % WL is first column
            WL = WL_mat(:,1); % consecutive columns are

            if WL(end) - WL(1) < 10
                Grating = 2400;
            elseif WL(end) - WL(1) > 30
                Grating = 300;
            end

            % a 1024 x 1024 matrix
            if ii == 1  || isempty(Summed_matrix) == 1
                Summed_matrix = BG_Int;
                % Otherwise ”arrays have incompatible sizes for this operation”
            else
                Summed_matrix = Summed_matrix + BG_Int;
            end
        else
            Subtractor = Subtractor - 1;
            % do nothing. Simply move onto next file to include

```

```
            Grating = NaN; % if no bg file is present, grating in

        end
    end

    % Computing the averaged BG matrix
    Averaged_matrix = Summed_matrix ./ (BG_no + Subtractor);
    % Saving the BG data
    Avg_Reshaped_BG = Averaged_matrix;
    if isa(Shots,'string') == 1 % if shot inputs are string (like on/off
        save(sprintf('%s/Data/Avg_BG/%s_Avg_BG.mat',filepath_save,Shot_val),'Avg_Reshaped_BG','BG_no','Subtractor')
    else
        save(sprintf('%s/Data/Avg_BG/%d_Avg_BG.mat',filepath_save,Shot_val),'Avg_Reshaped_BG','BG_no','Subtractor')
    end
    % Note it is important to note that the BG data is a reshaped matrix here,
    % so additional processing is required to bin over the corresponding
    % fibers. A variation of the spectrometer_visualizezr code can be used for
    % this purpose.
end
end
```

D.5 Spectrometer intensity integral

```
function [] = Integrated_Intensity_Function(Shots,Species_pixels,fibers,Species)

%% Overview
% This function computes the integrated intensity across the wavelength
% spectrum for the fibers of interest.

%% Outputs:

% Integrated_Intensities data mat: Contains spatially resolved emissivities
% for the shots of interest. For each shot, also has figures that
% illustrate the integration region to ensure that contaminating lines
```

```
% aren't present.

% Note:  Physical constants
% h = 6.62607015E-34; % J-Hz^-1
% c = 2.9979E8; % m/s

%% Code

for ii = 1:1:length(Shots)
    Shot_val = Shots(ii);
    figure
    for ff = 1:fibers
        filename = sprintf('../../../Processed_Data/Processed_Spec_Data/Data/Adaptive_Binning/Shot_%d_Fiber_%d_Spectrometer_BG_Sub_Final.mat',Shot_val,ff);
        load(filename)
        Wavelength_bin = Wavelength(Species_pixels(1):Species_pixels(end));
        I_bin = I_BGsubbed(Species_pixels(1):Species_pixels(end));
        Integrated_Intensity_WL(ff) = trapz(Wavelength_bin, I_bin);

        % After all fibers have been iterated over, plot the WL/Int
        % information
        plot(Wavelength_bin,I_bin)
        hold on

    end

    legend('F1','F2','F3','F4','F5','F6','F7')
    xlabel('Wavelenth (nm)')
    ylabel('Intensity (A.U.)')
    fig = gcf;
    fig.PaperPosition = [0 0 10 6];
    print(sprintf('../../../Processed_Data/Processed_Spec_Data/Data/Intensity_Integrations/Png/Integrated_Region_Shot_%d_all_fibers_%s',Shot_val,Species),'-r300','-dpng')
    savefig(sprintf('../../../Processed_Data/Processed_Spec_Data/Data/Intensity_Integrations/Fig/Integrated_Region_Shot_%d_all_fibers_%s.fig',Shot_val,Species) )

  % Saving to matrix
    save(sprintf('../../../Processed_Data/Processed_Spec_Data/Data/Intensity_Integrations/Data/Integrated_Intensities_Shot_%d_%s.mat',Shot_val,Species),'Integrated_Intensity_WL','
```

```
        Species_pixels')
    close all
end
```

D.6 Effective emission coefficient processing

```
function [] = Xeff_Batch_Processing(Direc_PsrName,Line_Info,Save_order,WL_or_eV_LineInfo,varnumel
    ,matfilename,load_prism_key,final_mat_name)

%% Xeff_Batch_Processing

%% Overview:
% This code will allow the user the specify a number of emission centroids,
% and the directory of a set of PrismSPECT simulations, and will then load
% the simulation data, and will then determine the effective emission
% coefficient (using CRM theory) and will then save the Xeffs in various
% mat files. The mat files will be structured s.t. species corresponds to
% the columns (maybe store these as struct. to eliminate ambiguity) and the
% rows will correspond to temperature (in incrments of .1 eV). This batch
% processing can also be used later on to determine temperrature via the
% ratio method....

% Note: PrismSPECT data is given in energy units. Thus the integration
% region corresponds to energy. The integration bounds are inputs in this
% analysis and will be stored in the data file, and must be carefully
% considered for each case. There will be file outputs that bound the
% integrated region so that they can be inspecte again upon further use. A
% good way to bound regions is to simply look at extremas in temp and ne
% cases, and make sure no overlapping liens are nearby.

%% User Inputs
%Direc_PsrName = []; % first row is directory names,
% second row is correspondging psr names for sims
% Example: Direc_PsrName = [50_WG_N_additional_Lines_Xeff';50_WG_N_additional_Lines_Xeff'];

%Line_Info = []; % Matrix where elements in first row correspond to centroid
```

```
% of interest, second row is beginning integration bouund, third row
% is final integration bound (both in wavelengths)
% fourth row is molar fraction of the element of interest in the sims that
% have been run.
% fifth row is save order. 6th row is species. 5th and 6 row entries are
% redundant, but used to double check when processing data.
% The integration bounds are given in terms of the x-axis.

% WL_or_eV_LineInfo: This is to state whether the line_info boundary
% information is provided in WL or eV units

%Save_order = ["total","ArII","NII","AlIII","f_f"]; % save order. Verified
% with load prims test codes
%% Inferred structure of spect files
% spect{1,1}(:,4) --> total
% spect{1,1}(:,5) --> species 1
% spect{1,1}(:,7) --> species 2
% spect{1,1}(:,9) --> species 3
% spect{1,1}(:,11) --> free - free
% Note: The PrismSPECT lines are not detreneded: Thus a linear polyfit
% will be used to detrend the lines prior to analysis.

%% Code Outputs:
% This code will output multiple figures in the "Integration_Figures"
% directory. There will be a figure for each ni iteration. Within each
% figure, there will be multiple subplots, each corresponding to a centroid
% of interest. Each of these subplots will overlay the line profiles for
% all the simulated temperatures. This can be used to ensure no
% contaminating lines are skewing the integration.

%% Code

% physical constants
c = 2.9979E+8; % units of meters/second
h = 6.6261E-34; % J * s (source: Plasma formulary). Note: Here we are using h,
% not hbar, which is also in the plasma formulary and is different by a
% factor of 2pi
eV_per_Joule = 6.241509E+18; % source:
m_per_nm = 1E-9; % source:
```

```

Entry = 1; %Initializing row entry in struct
for ii = 1:size(Direc_PsrName,2) % Across the numebr of psr files (columns)
    % that will be processed at once
    sim_data_path = Direc_PsrName(1,ii); % Directory name
    simname = Direc_PsrName(2,ii); % Psr name associated with directory

    if load_prism_key == 1 % this indicates you want to run the pspect load
        % function
        [datastruct, spect] = loadPrism(sim_data_path,simname,varnumel); % load all relevant prismspect data
    else
        load(matfilename) % else load the matfile name already
    end

    Iteration_Num = size(spect); % Returns mat with two entries. First are
    % are number of iterated temperatures (rows), second are number of iterated
    % densities (columns). Product of the two are the number of ppd files that have been
    % processed.

    %% Processing the Xeff at files
    for jj = 1:Iteration_Num(2) % number of density iterations
        for kk = 1:Iteration_Num(1) % number of temperature iterations
            % this forms the independent variable in the mat file.
            T = datastruct.T(kk,jj);
            ni = datastruct.ni(kk,jj);
            Z = datastruct.Z(kk,jj); % Mean charge state of system
            ne = datastruct.ne(kk,jj);
            Energy = spect{kk,jj}(:,1); % Energy in eV
            for ll = 1:size(Line_Info,2) % Iterating through elements of
                % interest
                Centroid = Line_Info(1,ll); % characteristic centroid of line
                Starting_Bound = Line_Info(2,ll); % Starting integration
                % bound for element of interest. These are in units of
                % [nm]
                Ending_Bound = Line_Info(3,ll); % Ending integration bound
                % these are in units of [nm]
                Molar_Frac = Line_Info(4,ll); % fourth row is molar frac used in the simulation
                % this is used to recover atomic number density
```

```
Line_Save_Order = Line_Info(5,ll); % index corresponding to
% the order in which these species were saved in the
% PrismSPECT simulation. This is defined in the simulation
% file itself, so it is important ot make sure that the
% Line_Info matrix is congruent with simulation setup.

    if Ending_Bound > Starting_Bound
     Temp = Starting_Bound;
     Starting_Bound = Ending_Bound;
     Ending_Bound = Temp;
     else
        sprintf('Double check bound formatting for line info mat')
    end

% Converting starting and ending bounds to units of energy
if WL_or_eV_LineInfo == ”nm”
    Starting_Bound = ((h*c) / (str2num(Starting_Bound) * m_per_nm)) * eV_per_Joule; % The
    % 1E-9 converts from nm to m for the analysis. The
    % 6.241509E+18 converts from J to eV
    Ending_Bound = (h*c) / (str2num(Ending_Bound) * m_per_nm) * eV_per_Joule;

end

Species = Line_Info(6,ll); % The species being processed
if Save_order(str2num(Line_Save_Order)+1) ~= Species
    % The +1 is because save_order(1) is free-free
    fprintf('\n ERROR. Double check line info matrix')
end % Sanity check before proceding

nspecies = ni * str2num(Molar_Frac); % This is the atomic number density
% for the species of interest, consisting of all charge
% states (including neutrals)

% Loading corresponding species intensity
if str2num(Line_Save_Order) == 1 % first save species
    Intensity = spect{kk,jj}(:,5); % First save
elseif str2num(Line_Save_Order) == 2
    Intensity = spect{kk,jj}(:,7); % Second save
```

```
                elseif str2num(Line_Save_Order) == 3
                    Intensity = spect{kk,jj}(:,9); % Third save
                end
                % We are only looking at 3 species for now. For additional
                % species, add the relevant fields to this structure.

                % Detrending + Integrating line intensity
                [~, px1] = min(abs(Starting_Bound - Energy));
                [~, px2] = min(abs(Ending_Bound - Energy));

                slope=((Intensity(px2)-Intensity(px1))/(px2 - px1));
                trend=(px1:px2).*slope+(Intensity(px1)-(slope.*px1)); % point slope form

                if size(Intensity(px1:px2),2) ~= size(trend,2) % if arrays are not compatible
                    trend = trend'; % transpose to avoid a matrix from being
                    % generated via subtraction
                end
                Intensity_detrend = Intensity(px1:px2) - trend; % detrending signal.
                Integrated_Intensity_untrended = trapz(Energy(px1:px2),Intensity(px1:px2));
                Integrated_Intensity_detrend = trapz(Energy(px1:px2),Intensity_detrend);
                % Due to conservation of energy, wavelength and energy
                % integrals will be equivalent as long as Jacobian is
                % observed

                % Generating figure to show integrated bounds to ensure the
                % effect of contaminating lines are kept to a minimum.
                figure(jj) % For each density iteration, plotting all lines
                % from all temperature iterations on a subplot, 1 per line

                subplot(size(Line_Info,2),1,ll)
                plot(Energy(px1:px2),Intensity_detrend,'LineWidth',1.5,'Color','b')
                hold on
                xlabel('Energy (eV)')
                ylabel('Intensity (erg/cm3/ster/s/eV)')
                grid on
                hold on

                %Xeff.(sprintf("Energy_Line_%s",Centroid))(Entry,:) = Energy; % pixels for integration
```

```
                Xeff.(sprintf(”Pixels_Line_%s”,Centroid))(Entry,:) = [px1,px2]; % pixels for integration
                %Xeff.(sprintf(”Intensity_Line_%s_detrended”,Centroid))(Entry,:) = Intensity_detrend; % detrended intensity
                Xeff.(sprintf(”Xeff_Line_%s”,Centroid))(Entry,:)= Integrated_Intensity_detrend / (nspecies * ne);
                % This will be saved as a single dimension vector where
                % each entry will correspond to different temperature,
                % electron density pairing. This will be specified by an
                % additional field in the code.
                Xeff.(sprintf(”Integrated_Int_Line_%s_detrended”,Centroid))(Entry,:) = Integrated_Intensity_detrend;
                % This will be used for temperature ratios later on. The
                % structuring is the same as the Xeff entry above.
                Xeff.(sprintf(”Integrated_Int_Line_%s_untrended”,Centroid))(Entry,:) = Integrated_Intensity_untrended;
                % Saved for verification purposes later on.

                Xeff_Compilled_Mat.(sprintf(”Xeff_Line_%s”,Centroid))(kk,jj) = Xeff.(sprintf(”Xeff_Line_%s”,Centroid))(Entry);

                % Verification Plotting
                if kk == Iteration_Num(1) % If at the very end of iteration, plot verification plots
                    figure(Iteration_Num(2)+ll)
                    plot(datastruct.T(:,1),Xeff_Compilled_Mat.(sprintf(”Xeff_Line_%s”,Centroid))(:,jj))
                    % one column of T is from 1.3 −−> 3
                    % the corresponding column of Xeff compiled is for the
                    % density of interest
                    hold on
                    xlabel('Temperature')
                    ylabel('Xeff')

                end

            end

        Xeff.(sprintf(”Sim_Inputs_ne”))(Entry,:) = ne;
```

```
        Xeff.(sprintf("Sim_Inputs_Te"))(Entry,:) = T;
        Xeff.(sprintf("Sim_Inputs_ni"))(Entry,:) = ni;
        Xeff.(sprintf("Sim_Inputs_Z"))(Entry,:) = Z;
        % These are meant to map 1:1 with simulated Xeff
        % This can be used to plot everything later.
        Entry = Entry + 1; % Move onto the next entry
        end

    end
end
% Saving data to MAT Files
batch_save_name = sprintf('%s.mat',final_mat_name);
save(batch_save_name,'Xeff')

end
```

D.7 Effective emission coefficient plotting

```
function [] = Xeff_Plotting_Script(Line_Info,varnumel,density_plot,WG)
%% Plotting Script: Xeff Batch Processing
close all
clc
% Written by: Ameer Mohammed

%% Overview:
% This code takes the structure generated by Xeff_Batch_Processing, and
% generates a series of plots of all the effective emission coefficients so
% that it can be visualized. This function cab be called through
% Xeff_Batch_Procession_Function_Calls, or it can be run on its own to
% generate the necessary figures

%% Inputs:
% Xeff & varnumel : Structure. This contains all the integrated intensity information,
% as well as the simulation Te, ni_tot A and ne. This is provided as a
% single column vector where all elements map 1:1 with each other, but can
% be reshaped according to the command varnumel, which specifies the number
```

```
% of temperature iterations (varnumel(1)) and total ion density iterations
% (varnumel(2))

% Line_Info: Matrix. Specified in the Xeff_Batch_Processing_Function_Calls

% density_plot: This represents the indexes corresponding to the subset of
% densities that you want to plot. This helps to keep the figure manageable
% so that the underlying physics does not get lost in the weeds.

%% Outputs

%% Code:

load(sprintf('Data/Batch_%dWG_Xeff.mat',WG));

% Loading simulation input parameters
Te = Xeff.(sprintf("Sim_Inputs_Te")); % electron / plasma temperature
ni_tot = Xeff.(sprintf("Sim_Inputs_ni")); % Total ion density
ne = Xeff.(sprintf("Sim_Inputs_ne")); % Electron density
Z = Xeff.(sprintf("Sim_Inputs_Z")); % Mean charge state

% Reshaping simulation input parameters
Te_reshaped = reshape(Te,varnumel);
ni_tot_reshaped = reshape(ni_tot,varnumel);
ne_reshaped = reshape(ne,varnumel);
Z_reshaped = reshape(Z,varnumel);

% Loading simulation output parameters
for ll = 1:size(Line_Info,2) % Specifies the number of lines Xeff was generated for
    Centroid = Line_Info(1,ll); % Specifies the center WL of the line
    Molar_Frac = str2num(Line_Info(4,ll)); % Specifies the percent composition for the species
    nspecies = ni_tot_reshaped .* Molar_Frac; % For every ion density that
    % is queried, the atomic aluminum numbr density across all charge
    % states is the percent composition times the total ion density

    % states (including neutrals)
    Detrended_Intensity = Xeff.(sprintf("Integrated_Int_Line_%s_detrended", Centroid));
    Xeff_Output = Xeff.(sprintf("Xeff_Line_%s",Centroid));

```

```
    % Reshaping simulation output parameters
    Detrended_Intensity_reshaped = reshape(Detrended_Intensity,varnumel);
    Xeff_reshaped = reshape(Xeff_Output,varnumel);

    % Generating plot of Xeff
    figure(11)
    Legend_Vector = [];  % Initializing vector
    for ii = density_plot
        semilogy(Te_reshaped(:,ii),Xeff_reshaped(:,ii),'LineWidth',1.5)
        grid on
        hold on
        Density_Query = ni_tot_reshaped(1,ii); % the 1 is because
        % every row vector of ni_tot_reshaped is the same
        Legend_Entry = sprintf("%.1e",Density_Query); % converting to string
        Legend_Vector = [Legend_Vector,Legend_Entry]; % concaetnating legend vector
    end

    leg = legend([Legend_Vector],'location','northwest') % legends correspond to the densities that
    % have been queried
    title(leg,sprintf("$n_{i_{tot}}$"),'Interpreter','latex' )
    xlabel('T_{e} (eV)')
    ylabel('\chi^{Pspect}')
    title(sprintf("$\\lambda$ = %s nm", Centroid),'Interpreter','latex')
    filename = sprintf("Fig/Xeff_%s_nm_WG%d.fig",Centroid,WG);
    filename_png = sprintf("Fig/Xeff_%s_nm_WG%d",Centroid,WG);
    savefig(filename)
    a = gca;
a.FontSize = 16;
a.LineWidth = 1.5;
hold on
grid on
l1.FontSize = 20;

fig = gcf;
fig.PaperPosition = [0 0 8 6]

    print(filename_png,'-dpng','-r300')

```

```
    % Closure test
    figure(size(Line_Info,2)+ll)
    Inferred_ni_species = Detrended_Intensity_reshaped ./ (Xeff_reshaped .* ne_reshaped);
    Closed_ne = (Inferred_ni_species ./ Molar_Frac) .* Z_reshaped;

    for ii = 1:varnumel(2) % Iterating over all densities
        plot(Te_reshaped(:,ii),ne_reshaped(:,ii),'color',function_matlab_plot_color(1),'LineWidth
            ',1.5)
        hold on
        plot(Te_reshaped(:,ii),Closed_ne(:,ii),'color',function_matlab_plot_color(2),'LineWidth'
            ,1.5)
        grid on
        hold on
    end

end

end
```

Bibliography

[1] Elizabeth C Merritt. *Measurements of railgun generated supersonic plasma jet propagation and two jet oblique merging.* The University of New Mexico, 2013.

[2] John David Anderson. *Modern compressible flow: with historical perspective*, volume 12. McGraw-Hill New York, 1990.

[3] Michel Y Jaffrin and Ronald F Probstein. Structure of a plasma shock wave. *The Physics of Fluids*, 7(10):1658–1674, 1964.

[4] Brett D Keenan, Andrei N Simakov, Luis Chacón, and William T Taitano. Deciphering the kinetic structure of multi-ion plasma shocks. *Physical Review E*, 96(5):053203, 2017.

[5] IAkov Borisovich Zel dovich, Yurii Petrovich Raizer, and Wallace D Hayes. *Physics of shock waves and high-temperature hydrodynamic phenomena*, volume 1. Academic Press New York, 1966.

[6] Garry McCracken and Peter Stott. *Fusion: the energy of the universe.* Academic Press, 2012.

[7] C Bellei, PA Amendt, SC Wilks, MG Haines, DT Casey, CK Li, R Petrasso, and DR Welch. Species separation in inertial confinement fusion fuels. *Physics of Plasmas*, 20(1):012701, 2013.

[8] Maximilian Kurt Schneider. *Characterization of collisional shock structures induced by the stagnation of railgun-driven multi-ion-species plasma-jets.* PhD thesis, Virginia Tech, 2020.

[9] Mohammad Hamed Samimi, Arash Mahari, Mohammad Ali Farahnakian, and Hossein Mohseni. A review on the rogowski coil principles and applications. *measurements*, 4: 5, 2013.

[10] Ian H Hutchinson. Principles of plasma diagnostics. *Plasma Physics and Controlled Fusion*, 44(12):2603–2603, 2002.

[11] Teledyne Princeton Instruments. Iccd and emiccd cameras: The basics, n.d. Accessed May, 2023. https://www.princetoninstruments.com/learn/camera-fundamentals/iccd-and-emiccd-basics.

[12] Colin S Adams, Auna L Moser, and Scott C Hsu. Observation of rayleigh-taylor-instability evolution in a plasma with magnetic and viscous effects. *Physical Review E*, 92(5):051101, 2015.

[13] Elizabeth C Merritt, Auna L Moser, Scott C Hsu, Colin S Adams, John P Dunn, A Miguel Holgado, and Mark A Gilmore. Experimental evidence for collisional shock formation via two obliquely merging supersonic plasma jets. *Physics of Plasmas*, 21(5): 055703, 2014.

[14] Elizabeth C Merritt, Alan G Lynn, Mark A Gilmore, and Scott C Hsu. Multi-chord fiber-coupled interferometer with a long coherence length laser. *Review of Scientific Instruments*, 83(3):033506, 2012.

[15] AI Mohammed and CS Adams. Ion shock layer formation during multi-ion-species plasma jet stagnation events. *Physics of Plasmas*, 29(7):072307, 2022.

[16] Elizabeth C Merritt, Auna L Moser, Scott C Hsu, John Loverich, and Mark Gilmore. Experimental characterization of the stagnation layer between two obliquely merging supersonic plasma jets. *Physical Review Letters*, 111(8):085003, 2013.

[17] MK Schneider, AI Mohammed, and CS Adams. Characterization of plasma jets driven by a small linear railgun. *Plasma Sources Science and Technology*, 29(4):045013, 2020.

[18] Prism Computational Sciences: www.prism-cs.com.

[19] Auna L Moser and Scott C Hsu. Experimental characterization of a transition from collisionless to collisional interaction between head-on-merging supersonic plasma jets. *Physics of Plasmas*, 22(5):055707, 2015.

[20] GV Vogman and U Shumlak. Deconvolution of stark broadened spectra for multi-point density measurements in a flow z-pinch. *Review of scientific instruments*, 82(10):103504, 2011.

[21] Hans-Joachim Kunze. *Introduction to plasma spectroscopy*, volume 56. Springer Science & Business Media, 2009.

[22] Miloš Burger and Jörg Hermann. Stark broadening measurements in plasmas produced by laser ablation of hydrogen containing compounds. *Spectrochimica Acta Part B: Atomic Spectroscopy*, 122:118–126, 2016.

[23] Tom Byvank, Samuel J Langendorf, Carsten Thoma, and Scott C Hsu. Observation of shock-front separation in multi-ion-species collisional plasma shocks. *Physics of Plasmas*, 27(4):042302, 2020.

[24] Samuel J Langendorf, Kevin C Yates, Scott C Hsu, Carsten Thoma, and Mark Gilmore. Experimental study of ion heating in obliquely merging hypersonic plasma jets. *Physics of Plasmas*, 26(8):082110, 2019.

[25] Andrew S Richardson. *2019 NRL plasma formulary*. Naval Research Laboratory Washington, DC, 2019.

[26] Ronald E Bell. An inversion technique to obtain full poloidal velocity profiles in a tokamak plasma. *Review of scientific instruments*, 68(2):1273–1280, 1997.

[27] Igor B Gornushkin, Sergej V Shabanov, and Ulrich Panne. Abel inversion applied to a transient laser induced plasma: implications from plasma modeling. *Journal of Analytical Atomic Spectrometry*, 26(7):1457–1465, 2011.

[28] Jonathan Mooney and Patanjali Kambhampati. Get the basics right: Jacobian conversion of wavelength and energy scales for quantitative analysis of emission spectra, 2013.

[29] Francis F Chen. Introduction to plasma physics and controlled fusion. switzerland, 2016.

[30] Grigory Kagan and Xian-Zhu Tang. Electro-diffusion in a plasma with two ion species. *Physics of Plasmas*, 19(8):082709, 2012.

[31] Grigory Kagan and Xian-Zhu Tang. Thermo-diffusion in inertially confined plasmas. *Physics Letters A*, 378(21):1531–1535, 2014.

[32] F Chu, AL LaJoie, BD Keenan, L Webster, SJ Langendorf, and MA Gilmore. Experimental measurements of ion diffusion coefficients and heating in a multi-ion-species plasma shock. *Physical Review Letters*, 130(14):145101, 2023.

[33] Francis F Chen et al. *Introduction to plasma physics and controlled fusion*, volume 1. Springer, 1984.

[34] M Wolff and RC Tautz. Cosmic-ray acceleration at collisionless astrophysical shocks using monte-carlo simulations. *Astronomy & Astrophysics*, 580:A58, 2015.

[35] Fan Guo, J Randy Jokipii, and Jozsef Kota. Particle acceleration by collisionless shocks containing large-scale magnetic-field variations. *The Astrophysical Journal*, 725(1):128, 2010.

[36] Steven C Cowley. The quest for fusion power. *Nature physics*, 12(5):384–386, 2016.

[37] RA Gabrielli, D Petkow, G Herdrich, R Laufer, and H-P Röser. Two generic concepts for space propulsion based on thermal nuclear fusion. *Acta Astronautica*, 101:129–137, 2014.

[38] Peter Amendt, OL Landen, HF Robey, CK Li, and RD Petrasso. Plasma barodiffusion in inertial-confinement-fusion implosions: Application to observed yield anomalies in thermonuclear fuel mixtures. *Physical review letters*, 105(11):115005, 2010.

[39] Peter Amendt, SC Wilks, C Bellei, CK Li, and RD Petrasso. The potential role of electric fields and plasma barodiffusion on the inertial confinement fusion database. *Physics of Plasmas*, 18(5):056308, 2011.

[40] O Larroche. Ion fokker-planck simulation of d-3he gas target implosions. *Physics of Plasmas*, 19(12):122706, 2012.

[41] E Vold, R Rauenzahn, and AN Simakov. Multi-species plasma transport in 1d direct-drive icf simulations. *Physics of Plasmas*, 26(3):032706, 2019.

[42] Lev Davidovich Landau and Evgenii Mikhailovich Lifshitz. *Fluid Mechanics: Landau and Lifshitz: Course of Theoretical Physics, Volume 6*, volume 6. Elsevier, 2013.

[43] Abraham Achterberg. *Gas dynamics: an introduction with examples from astrophysics and geophysics*. Springer, 2016.

[44] J Craig Wheeler, Robert P Harkness, Zalman Barkat, and Douglas Swartz. Supernovae, supernebulae, and nucleosynthesis. *Publications of the Astronomical Society of the Pacific*, 98(608):1018, 1986.

[45] PA Amendt, JL Milovich, SC Wilks, CK Li, RD Petrasso, and FH Séguin. Electric field and ionization-gradient effects on inertial-confinement-fusion implosions. *Plasma Physics and Controlled Fusion*, 51(12):124048, 2009.

[46] Robert G Jahn. *Physics of electric propulsion*. Courier Corporation, 2006.

[47] Precision Ceramics. Shapal™ hi m soft, n.d. Accessed January, 2024. `https://precision-ceramics.com/uk/wp-content/uploads/Shapal-Hi-M-Soft-UK-08.02.23.pdf`.

[48] N Konjević, A Lesage, Jeffrey R Fuhr, and Wolfgang L Wiese. Experimental stark widths and shifts for spectral lines of neutral and ionized atoms (a critical review of selected data for the period 1989 through 2000). *Journal of Physical and Chemical Reference Data*, 31(3):819–927, 2002.

[49] Dejan Dojić, Miloš Skočić, Srdjan Bukvić, and Stevan Djeniže. Stark broadening measurements of al ii, al iii and he i 388.86 nm spectral lines at high electron densities. *Spectrochimica Acta Part B: Atomic Spectroscopy*, 166:105816, 2020.

[50] Walter Fox Smith. *Waves and oscillations: a prelude to quantum mechanics*. Oxford University Press, 2010.

[51] John R Taylor. Error analysis. *Univ. Science Books, Sausalito, California*, 20, 1997.

[52] Xian-Zhu Tang, HL Berk, Zehua Guo, and CJ McDevitt. Reduced fokker-planck models for fast particle distribution across a transition layer of disparate plasma temperatures. *Physics of Plasmas*, 21(3), 2014.

[53] S-B Wang and Amy E Wendt. Sheath thickness evaluation for collisionless or weakly collisional bounded plasmas. *IEEE transactions on plasma science*, 27(5):1358–1365, 1999.

[54] Ursel Fantz. Basics of plasma spectroscopy. *Plasma sources science and technology*, 15 (4):S137, 2006.

[55] Joseph Donald Huba. *NRL plasma formulary*, volume 6790. Naval Research Laboratory, 1998.

[56] Andrei N Simakov, Brett D Keenan, William T Taitano, and Luis Chacón. Plasma ion stratification by weak planar shocks. *Physics of Plasmas*, 24(9), 2017.

[57] PD Marković and FR Scott. Interaction of a helium plasma with an inhomogeneous transverse magnetic field. *The Physics of Fluids*, 14(8):1742–1747, 1971.

[58] Akihide Fujisawa. Review of plasma turbulence experiments. *Proceedings of the Japan Academy, Series B*, 97(3):103–119, 2021.

[59] Newport MKS. Spectral calibration lamp, neon, n.d. Accessed June, 2023. `https://www.newport.com/p/6032`.

[60] Thorlabs, Inc. Multimode fiber tutorial, n.d. Accessed January, 2024. `https://www.thorlabs.com/newgrouppage9.cfm?objectgroup_id=10417`.

[61] C M Croarkin. Nist/sematech engineering statistics handbook, chapter 2: Measurement process characterization. 2003.

[62] John H Moore, Christopher C Davis, and Michael A Coplan. *Building scientific apparatus*. Cambridge university press, 2009.